



LUND UNIVERSITY

Atomic Scale Characterization of III-V Nanowire Surfaces

Knutsson, Johan

2017

Document Version:

Publisher's PDF, also known as Version of record

[Link to publication](#)

Citation for published version (APA):

Knutsson, J. (2017). *Atomic Scale Characterization of III-V Nanowire Surfaces*. [Doctoral Thesis (compilation), Department of Physics]. Lund University, Faculty of Science, Department of Physics, Division of Synchrotron Radiation Research.

Total number of authors:

1

Creative Commons License:

Other

General rights

Unless other specific re-use rights are stated the following general rights apply:

Copyright and moral rights for the publications made accessible in the public portal are retained by the authors and/or other copyright owners and it is a condition of accessing publications that users recognise and abide by the legal requirements associated with these rights.

- Users may download and print one copy of any publication from the public portal for the purpose of private study or research.
- You may not further distribute the material or use it for any profit-making activity or commercial gain
- You may freely distribute the URL identifying the publication in the public portal

Read more about Creative commons licenses: <https://creativecommons.org/licenses/>

Take down policy

If you believe that this document breaches copyright please contact us providing details, and we will remove access to the work immediately and investigate your claim.

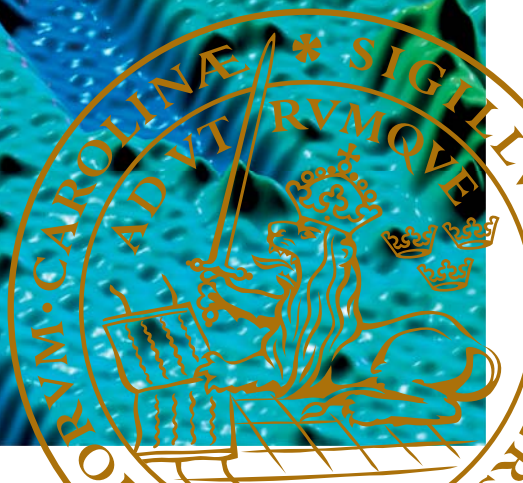
LUND UNIVERSITY

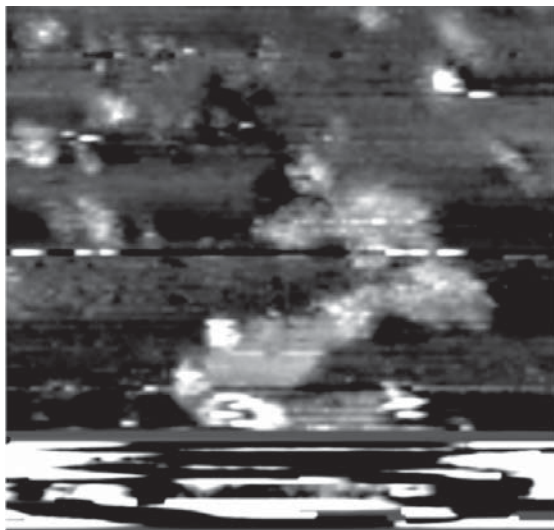
PO Box 117
221 00 Lund
+46 46-222 00 00

A 3D surface plot of a III-V nanowire, showing a highly textured surface with a color gradient from blue to green. The plot is oriented diagonally, showing the length of the nanowire. The surface is covered in a complex, porous-like structure with many small peaks and valleys. The background is black.

Atomic Scale Characterization of III–V Nanowire Surfaces

JOHAN VALENTIN KNUTSSON
FACULTY OF SCIENCE





The nano hype train is real; even Superman have jumped on it.

Atomic Scale Characterization of III–V Nanowire Surfaces

Johan Valentin Knutsson



LUND
UNIVERSITY

DOCTORAL DISSERTATION

by due permission of the Faculty of Science, Lund University, Sweden.

To be defended at the Rydberg lecture hall at the Department of Physics

December 15, 2017, at 13.15.

Faculty opponent

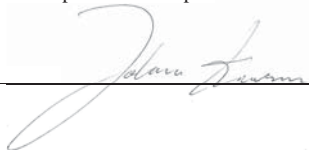
Prof. Randall Feenstra

Carnegie Mellon University, USA.

Organization LUND UNIVERSITY Division of Synchrotron Radiation Research Department of Physics Box 118 S-221 00 Lund Author(s) Johan Valentin Knutsson		Document name DOCTORAL DISSERTATION	
		Date of issue November 21, 2017	
		Sponsoring organization	
Title and subtitle: Atomic Scale Characterization of III–V Nanowire Surfaces			
Abstract <p>This dissertation focus on the atomic-scale characterization of the surface properties and electronic structure of III–V semiconductor nanowires (NWs). Since the early 2000s, the fabrication and characterization of III–V NWs has been a very significant topic within material science due to their potential for applications in lighting, energy harvesting, and electronics. A prominent feature of the NW geometry is the ability to form heterostructures—both radially and axially—for shaping the electronic landscape in the NW. The heterostructures can consist of variations in the crystal structure, material composition, or a combination of the two. A pre-requisite for the fabrication of advanced heterostructures in NWs is an intricate knowledge concerning the atomic-scale surface properties as well as the material and crystal structure-dependent electronic properties. However, little is known about the surface properties of III–V NWs and how the electronic structure behaves at the heterostructure interface at the atomic level.</p> <p>In this dissertation I describe the work on the electronic properties of crystal structure heterojunctions in GaAs and InAs NWs, down to the atomic bilayer level. Scanning tunneling microscopy and spectroscopy (STM/S) was used to probe the surface structure and electronic properties of NW surfaces with atomic resolution. Also, the effects of material overgrowth on GaAs and InAs NW surfaces was studied at the atomic scale. The studies allowed for the identification of nucleation sites, incorporation processes, and growth modes. Furthermore, quantum-size effects have been investigated within crystal phase structures in NWs.</p> <p>Due to the large surface–to–volume ratio of nanostructures, the optical and electronic performance of NW devices is often impeded by surface defects. The quantity, origin and individual influence of such defects is unknown. I have used atomic-scale STM imaging of externally biased NW devices <i>operando</i>, as well as x-ray photoelectron spectroscopy (XPS) measurements, to investigate how surface oxides and atomic-scale defects affect the conductivity of NWs.</p>			
Key words III–V semiconductor materials, nanowire, surface, scanning tunneling microscopy, scanning tunneling spectroscopy, wurtzite, zinc blende			
Classification system and/or index terms (if any)			
Supplementary bibliographical information		Language English	
ISSN and key title		ISBN 978-91-7753-509-6 (print) 978-91-7753-510-2 (pdf)	
Recipient's notes		Number of pages 251	Price
		Security classification	

I, the undersigned, being the copyright owner of the abstract of the above-mentioned dissertation, hereby grant to all reference sources permission to publish and disseminate the abstract of the above-mentioned dissertation.

Signature _____



Date _____

2017-11-07

Atomic Scale Characterization of III–V Nanowire Surfaces

Johan Valentin Knutsson
Doctoral Dissertation
2017



LUND
UNIVERSITY

Division of Synchrotron Radiation Research
Department of Physics
Lund University

Front cover:

STM image depicting the top-most As-atoms of the {11-20}-type facet of a GaAs nanowire. The more protruding atoms, which are randomly distributed on the surface, correspond to Sb atoms which have replaced As in the atomic lattice as a result of Sb deposition and annealing. Image courtesy of Martin Hjort.

Back cover:

STM image of a InAs surface which may contain evidence of nanoscopic intelligent life. The image becomes especially convincing when wearing a foil hat.

Copyright © Johan Knutsson

Department of Synchrotron Radiation Research
Department of Physics
Faculty of Science
Lund University
ISBN: 978-91-7753-509-6
ISS(N+1): 978-91-7753-510-2

Printed in Sweden by Media-Tryck, Lund University
Lund 2017



RWGWARAHHHHWRGGWRWRW

- Chewbacca, The Empire Strikes Back

CONTENTS

Abstract	i
Populärvetenskaplig sammanfattning	iii
Preface and list of publications	v
Acknowledgements	xi
Abbreviations and Symbols	xv
1 Introduction	1
2 Scanning Tunneling Microscopy	5
2.1 Theory	7
2.2 Image Contrast	8
2.3 Imaging nanowires with STM	10
2.4 Tip preparation	12
3 Scanning Tunneling Spectroscopy	13
3.1 Variable z mode and data treatment	17
3.2 Band edge determination	19
3.3 Tip-induced band bending	20
3.4 Effects of low temperature	24
4 X-ray Photoelectron Spectroscopy	27
5 III–V Semiconductor Nanowires	31
5.1 Growth	32
5.1.1 Facets and Shell-growth	34
5.2 Crystal Phase Engineering	38
5.2.1 Electronic structure	41
5.2.2 Quantum dots and wells	43
6 Nanowire Surfaces	49
6.1 Surface morphology	50
6.2 Surface states	53
7 Surface Preparation and Modification	57
7.1 Sample preparation	57
7.2 Removal of native oxides	59

7.2.1	Effects on surface morphology	60
7.3	Surface modification	61
7.3.1	Bi deposition	61
8	Nanowire Devices	67
8.1	Device design	67
8.2	Device operation	70
9	Concluding Remarks and Outlook	75
10	Bibliography	79

ABSTRACT

This dissertation focus on the atomic-scale characterization of the surface properties and electronic structure of III–V semiconductor nanowires (NWs). Since the early 2000s, the fabrication and characterization of III–V NWs has been a very significant topic within material science due to their potential for applications in lighting, energy harvesting, and electronics. A prominent feature of the NW geometry is the ability to form heterostructures—both radially and axially—for shaping the electronic landscape in the NW. The heterostructures can consist of variations in the crystal structure, material composition, or a combination of the two. A pre-requisite for the fabrication of advanced heterostructures in NWs is an intricate knowledge concerning the atomic-scale surface properties as well as the material and crystal structure dependent electronic properties. However, little is known about the surface properties of III–V NWs and how the electronic structure behaves at the heterostructure interface at the atomic level.

In this dissertation I describe the work on the electronic properties of crystal structure heterojunctions in GaAs and InAs NWs, down to the atomic bilayer level. Scanning tunneling microscopy and spectroscopy (STM/S) was used to probe the surface structure and electronic properties of NW surfaces with atomic resolution. Also, the effects of material overgrowth on GaAs and InAs NW surfaces was studied at the atomic scale. The studies allowed for the identification of nucleation sites, incorporation processes, and growth modes. Furthermore, quantum-size effects have been investigated within crystal phase structures in NWs.

Due to the large surface-to-volume ratio of nanostructures, the optical and electronic performance of NW devices is often impeded by surface defects. The quantity, origin and individual influence of such defects is unknown. I have used atomic-scale STM imaging of externally biased NW devices *operando*, as well as x-ray photoelectron spectroscopy (XPS) measurements, to investigate how surface oxides and atomic-scale defects affect the conductivity of NWs.

POPULÄRVETENSKAPLIG SAMMANFATTNING

Sedan mitten på 1900 talet har halvledarmaterial revolutionerat hur vi ser på världen genom uppfinningar som det har gett upphov till, såsom datorer, solceller, och lysdioder. Det är möjligheten att kunna styra halvledarens förmåga att leda ström—mellan att vara nästan metallisk till att vara isolerande—som gör den användbar för tillämpningar inom elektronik. Under de senaste decennierna har elektroniska applikationer såsom datorer gått från att knappt få plats i ett rum till att lätt rymmas i en byxficka. Samtidigt har datorers processorkraft och effektiviteten ökat tusenfaldigt. Grunden till detta ligger i huvudsak i en miniatyrisering av halvledarkomponenter, till exempel transistorer, som gått från att vara centimeterstora till att rymmas inom några tiotals nanometer. En nanometer är en miljarddels meter. För att sätta dimensionerna i perspektiv: om en meter likställdes jordens omkrets, så skulle en nanometer ungefär motsvara längden på en tändsticksask (4 cm).

Att tillverka och studera objekt på nano-skalan kallas för nanoteknik. Nanoteknik används idag inom många områden såsom medicin, biologi, och fysik. Inom fysiken är nanoteknik viktig för tillverkning av till exempel transistorer, solceller och lysdioder. Tillverkning av sådana halvledarkomponenter bygger ofta på att man kombinerar material med olika elektroniska egenskaper. Genom att bygga (växa) och kombinera dessa material i lager på lager kan man skraddarsy komponentens egenskaper till att passa för diverse applikationer. Traditionellt sett har storskalig framställningen av sådan lager-på-lager-växt varit begränsad till att bara kunna växas i två dimensioner (2D). Ett stort problem med 2D-växt är att många materialtyper inte går att kombinera med varandra för att deras kristallstrukturer—det atomära mönstret i ett materialet—inte passar med varandra. Detta kan likställas med att försöka kombinera bitar av LEGO och Duplo med varandra.

I Lund har man de senaste åren experimenterat med att framställa en form av endimensionella halvledarstrukturer som kallas för nanotrådar. Nanotrådarna är stavformade strukturer med diametrar på nano-skalan och längder motsvarande tusentals nanometer. Nanotrådarnas små diametrar gör det möjligt att kombinera material trots att deras kristallstrukturer inte passar med varandra. Detta öppnar upp enorma möjligheter för att bygga nya elektroniska komponenter med unika eller förbättrade egenskaper. En annan fördel med nanotrådarna är att man kan kombinera material på fler sätt än i 2D-växt: både längs med nanotråden men även i lager på lager som skal runt trådarna. Ytterligare en unik fördel med nanotrådar är

att det går att medvetet ändra kristallstrukturen i dem utan att faktiskt byta material, vilket liksom materialkombinationer kan styra nanotrådens egenskaper.

Fördelen med att bara kombinera kristallstrukturer istället för material är att ytskiktet där två olika material möts ofta har defekter som påverkar komponenten negativt. Sådana defekter uppkommer inte då bara kristallstrukturen ändras. Att till viss del ersätta traditionella materialkombinationer med kristallstrukturförändringar skulle således kunna förbättra elektroniska och optiska komponenter avsevärt. En förutsättning för detta är dock att kristallstrukturernas elektroniska och optiska egenskaper är välkända, t.ex. hur snabbt och effektivt dom leder ström och vilka typer av ljus dom kan absorbera och emittera. Då vissa av kristallstrukturerna bara existerar i nanotrådar är de relativt svåra att studera med de metoder som traditionellt använts för 2D-material. Detta har resulterat i att många av de optiska och elektroniska egenskaperna är okända för dessa kristallstrukturer.

Således är inte nanotrådarnas optiska och elektroniska egenskaper fullt så bra som dom teoretiskt skulle kunna vara. En konsekvens av att bygga komponenter på nanoskalan är att andelen atomer som sitter på ytan av en struktur, jämfört med inuti, blir stor. Detta gör att en nanotråds optiska och elektroniska egenskaper helt kan bero på ytans egenskaper; till exempel om det sitter extra atomer ovanpå ytan eller fattas atomer i ytlagret. Hur dessa typer av defekter påverkar nanotrådarna är dock okänt. För att nanotrådar skall kunna uppnå sin fulla potential är det därför väldigt viktigt att ta fram lämpliga metoder för att kunna korrelera nanotrådarnas optiska och elektroniska egenskaper ner till den enskilda atomen.

I den här avhandlingen har jag använt mig av Sveptunnelmikroskopi och spektroskopi (STM/S) för att studera nanotrådsytor samt de elektroniska egenskaperna av olika kristallstrukturer. STM/S är en metod som gör det möjligt att studera ytor av material, samt deras elektroniska egenskaper, med upplösning bra nog till att kunna se enskilda atomer.

Avhandlingen behandlar halvledarmaterial, i huvudsak galliumarsenik (GaAs) och indiumarsenik (InAs). Dessa material har flera fördelar jämfört med det traditionella halvledarmaterialet kisel (Si). Exempelvis så rör sig elektroner väldigt snabbt i dessa material vilket gör att de lämpar sig för höghastighetselektronik. De har också överlägsna egenskaper som gör dem lämpliga som lysdioder och solceller. Jag har undersökt hur ändringar i kristallstrukturen påverkar nanotrådarnas elektroniska egenskaper. Jag har även studerat hur material växer på nanotrådsytorna för bättre kunna kontrollera lager-på-lager-växt med atomär kontroll på nanotrådar. Studier gällande hur enskilda defekter på nanotrådsytorna påverkar dess elektroniska egenskaper har också utförts. Det som upptäckts är av intresse för både grundforskning såsom tillämpningar inom till exempel elektronik.

PREFACE AND LIST OF PUBLICATIONS

This doctoral thesis presents my contribution to the atomic scale characterization of III–V semiconductor nanowires. Here, the techniques and methods used are explained. The underlying theory is presented as well as the results which have been published in scientific journals. The experimental work behind the publications has been performed at several locations and facilities including: Lund University, Sweden; MAX IV, Sweden; Center for Functional Nanomaterials, USA, University of Virginia, USA; and University of California Santa Barbara, USA. As per their focus, the publications included in this dissertation have been arranged in three sub-categories: (I) surface characterization and modification, (II) characterization of heterostructure interfaces, and (III) characterization of nanowire devices *operando*. This dissertation is based on the following papers, which will be referred to in the text by their roman numerals.

(I) SURFACE CHARACTERIZATION AND MODIFICATION

Paper I—Atomic-Scale Surface Structure and Morphology of InAs Nanowire Crystal Superlattices: the Effect of Epitaxial Overgrowth

J. V. Knutsson, S. Lehmann, M. Hjort, P. Reinke, E. Lundgren, K. A. Dick, R. Timm, and A. Mikkelsen

ACS Applied Materials & Interfaces **7**, 5748 (2015)

STM was used to determine the atomic scale dynamics of radial shell growth of InAs zinc blende NWs with a twinning superlattice, consisting of {111}A- and {111}B-type facets. A timeline of the shell growth could be created by imaging along the intentionally tapered NWs, where a gradient in shell-growth progression was present along the NW growth axis. We determined that crystal phase twin defects, located at the interface of the {111}A and {111}B facets, predominantly act as the nucleation centers for the shell growth. Also, the growth was found to be propagated *via* a step-flow growth mechanism which worked significantly faster on the {111}A-type facets compared to the {111}B-type. Additionally, we found a previously unobserved reconstruction on the {111}B-type surfaces.

I took a significant part in the planning of the experiment, the measurements, the data analysis, and the writing of the manuscript.

Paper II—Surface Morphology of Au-free Grown Nanowires After Native Oxide Removal

M. Hjort, J. V. Knutsson, B. Mandl, K. Deppert, E. Lundgren, R. Timm, and A. Mikkelsen

Nanoscale **7**, 9998 (2015)

STM was used to map the surface morphology and step density on InAs NWs grown without the use of an Au-particle. Imaging along several micrometers with monolayer height resolution over individual NWs showed a very low tapering of only $1.5 \text{ \AA}/\mu\text{m}$, being below the detection limit of other techniques. We also find that a large number of crystal phase defects give rise to a unique surface morphology that has previously not been observed in other NW systems. Individual As-vacancies at the surface were probed using filled and empty state imaging. The effects of hydrogen cleaning—used to remove native surface oxides—on the surface morphology was investigated. We conclude that the treatment has a small effect on the surface morphology, only affecting the topmost surface layer.

I took part in the planning of the experiment, the measurements, data analysis, and discussion about the manuscript.

Paper III—Crystal Phase Selective Bi Incorporation in GaAs Nanowires

J. V. Knutsson, N. Wilson, S. Lehmann, C. Palmström, K.A. Dick, R. Timm, and A. Mikkelsen.

In manuscript

In this paper, we present an atomic scale STM study on crystal phase dependent Bi-alloying in the topmost surface layer of GaAs NW side-wall facets. We find distinct differences in the Bi-formations on the Zb and wurtzite facets; on the zinc blende facets, the Bi is distributed stoichiometrically across the surface, whereas a short-range ordering is found on the wurtzite facets. The short-range ordering has a preference for forming atomic chains along the NW growth axis. STS investigation of the chains show signs of a size-dependent confinement of states for chains of different length.

I took a significant part in the planning of the experiment, the measurements, and data analysis as well as manuscript preparation.

(II) CHARACTERIZATION OF HETEROSTRUCTURE JUNCTIONS

Paper IV—Direct Imaging of Atomic Scale Structure and Electronic Properties of GaAs Wurtzite and Zinc Blende Nanowire Surfaces

M. Hjort, S. Lehmann, J. V. Knutsson, R. Timm, D. Jacobsson, E. Lundgren, K. A. Dick, and, A. Mikkelsen
Nano Letters **13**, 4492 (2013)

In this paper, we use STM/S to determine the bandgap energies and offsets between adjacent wurtzite and zinc blende crystal segments in GaAs NWs. The absolute values of the bulk band-properties of the wurtzite phase could be extracted by using the well-known bandgap of zinc blende as a reference and account for tip-induced band bending.

I took part in the planning of the experiment, the measurements, data analysis, and discussion about the manuscript.

Paper V—Electronic and Structural Differences Between Wurtzite and Zinc Blende InAs Nanowire Surfaces: Experiment and Theory

M. Hjort, S. Lehmann, J. V. Knutsson, A. A. Zakharov, Y. A. Du, S. Sakong, R. Timm, G. Nylund, E. Lundgren, P. Kratzer, K. A. Dick, and A. Mikkelsen
ACS Nano **8**, 12346 (2014)

The electronic and structural properties of bulk and surface were determined for adjacent wurtzite and zinc blende segments in InAs NWs using STM/S, low energy electron microscopy (LEEM), and photoemission electron microscopy (PEEM). In contrast to the theoretically predicted type II band alignment between wurtzite and zinc blende in InAs, we find a flat band alignment. We attribute the flat band alignment to Fermi level pinning at the surface as a result of the n-type defects in the NW, intrinsic to MOVPE growth. The results were compared with theoretical calculations based on *ab initio* methods. From the PEEM measurements, it was possible to extract the vacuum level of the wurtzite and zinc blende surfaces, respectively.

I took part in the planning of the STM experiment, the STM measurements, STM data analysis, and discussion about the manuscript.

Paper VI—Electronic Structure Changes due to Crystal Phase Switching at the Atomic Scale Limit

J. Knutsson, S. Lehmann, M. Hjort, E. Lundgren, K.A. Dick, R. Timm and A. Mikkelsen

ACS Nano **11**, 10519 (2017)

In this paper, we directly experimentally show that even for the smallest possible crystal phase change—a single atomic layer—the accompanying electronic structure change mimics that of the bulk crystal phases. We accomplish this by performing atomic level STM/S, operated at 5 K, on top of the sidewall surfaces of InAs NWs in the wurtzite phase with inclusions of monolayer thick zinc blende crystal segments. We show that the zinc blende electronic structure is localized within a single bilayer zinc blende segment such that an atomically sharp quantum well with confined states is formed. We also demonstrate the presence of de-localized surface states extending all over the NW facets; the surface states were not affected by the presence of singly bilayer zinc blende segments.

I took a significant part in the planning of the experiment, the measurements, the data analysis, and the writing of the manuscript.

(III) CHARACTERIZATION OF NANOWIRE DEVICES *OPERANDO*

Paper VII—Electrical and Surface Properties of InAs/InSb Nanowires Cleaned by Atomic Hydrogen

J.L. Webb, J. V. Knutsson, M. Hjort, S. Ghahmestani, K. A. Dick, R. Timm, and A. Mikkelsen

Nano Letters **8**, 4865 (2015)

This paper describes the procedure to use atomic hydrogen to remove native surface oxides of III–V NW surfaces, and how it affects the NW electronic properties. We use XPS and STM to demonstrate that the surface oxide can be removed from both InSb and InAs of heterostructure NWs by annealing to 380°C with a chamber pressure of atomic hydrogen of 10^{-6} mbar. In-vacuum electrical measurements on individual InAs/InSb heterostructure NWs reveal an increase of 2 orders of magnitude in the electrical conductance of the NWs when the surface oxide is removed. We attribute the increase in electrical conductivity to improved metal-semiconductor contacts as well as a reduction in surface states.

I took part in the experiments performed on the NWs and NW devices, the data analysis, and discussion about the manuscript.

Paper VIII—Imaging Atomic Scale Dynamics on III–V Nanowire Surfaces During Electrical Operation

J.L. Webb, J. V. Knutsson, M. Hjort, S.R. McKibbin, S. Lehmann, K. A. Dick, R. Timm, and A. Mikkelsen

Scientific Reports **7**, 12790 (2017)

Here we report on the first demonstration of atomic-scale STM imaging on the surfaces of individual nanowire devices during electrical operation. Structural and potential mapping of the surfaces of GaAs and InAs nanowire surfaces reveal a self-healing effect while under the influence by an external potential, such that single atomic defects are removed and the morphology smoothed at the monolayer level. We also determine how local surface defects and changes in crystal structure affect the externally applied potential across the nanowires.

I took part in the experiments performed on the NWs and NW devices, the data analysis, and discussion about the manuscript.

PAPERS NOT INCLUDED IN THIS THESIS

I also contributed to the following papers, which are outside the scope of this thesis:

Paper IX—Band Bending at the Heterointerface of GaAs/InAs Core/Shell Nanowires Monitored by Synchrotron X-ray Photoelectron Spectroscopy

B. Khanbabaee[?], G. Bussone, J. V. Knutsson, I. Geijselaers, C. E. Pryor, T. Rieger, N. Demarina, D. Grützmacher, M. I. Lepsa, R. Timm, and U. Pietsch

Journal of Applied Physics **120**, 145703 (2016)

Paper X—Self-cleaning and Surface Chemical Reactions During HfO₂ Atomic Layer Deposition on InAs

R. Timm, A. Head, S. Yngman, J. V. Knutsson, Martin Hjort, S.R. McKibbin, A. Troian, O. Persson, S. Urpelainen, J. Knudsen, J. Schnadt, and A. Mikkelsen

Submitted to Nature Communications (2017)

ACKNOWLEDGEMENTS

There are a large number of people that have contributed to the work behind this thesis, and I would like to extend a general appreciation towards all my co-workers for being friendly, engaging, cooperative, earnest, and supportive. With that being said, I would like to extend a few personal courtesies as well.

First of all, I would like to thank my main supervisors Anders Mikkelsen who have always found time for me. I appreciate that you have put up with my many questions, unrealistic deadlines, and for introducing me to the period. I also appreciate that you have entrusted your lab-toys to me, and for allowing me to, in an experimental fashion, realize that the beam shutter is an important function of a hydrogen gun. I admire you for your ability to find something useful from the most unsuccessful experiments. It has been a pleasure to do my Ph.D. studies under your supervision, and I could not have wished for a better supervisor.

I would also like to show gratitude towards my co-supervisor Rainer Timm, one of the friendliest persons I have met, and probably the best proof-reader in the world. I have appreciated our many discussions regarding TIBB and STS interpretation.

None of the work behind this thesis would have been possible without my partners in crime down in the STM labs. Martin Hjort, Sofie Yngman, Olof Persson, Milena Moreira, Andrea Troian, Jim Webb, and Sarah McKibbin, I thank you all for helping me out and providing a nice atmosphere that has resulted in many interesting results. I especially recognize Martin Hjort for teaching me all there is to know about the black magic behind STM measurements. He also deserves to be acknowledged for introducing me and my computer to Sabrina, Tom, Gordon, and many others, all who have supported me during long days and late nights in the lab.

The whole research group of Kimberly Dick Thelander is acknowledged for providing me with crystal structure engineered nanowires of unprecedented quality. In this regard, I would like to extend special thanks to Sebastian Lehmann for our lively conversations and his uncanny ability to grow nanowires with perfect crystal purity.

My collaborators at Brookhaven National Laboratory, Percy Zahl and Peter Sutter, are acknowledged. It has always been a pleasure to visit you; the prices in your cantina are commendable.

My collaborators at University of California in Santa Barbara, Nate Willson, Elliot Young, Shouvik Chatterjee and Chris Palmstrøm, are acknowledged. Nate, I would

like to express my gratitude for your indispensable help in the lab, at any time and day.

I would also like to acknowledge the research group of Petra Reinke at the University of Virginia for our collaborative work.

I acknowledge Behnam Khanbabaee and Genziana Bussone as well as Jan Knudsen, Ashley Head, and Joachim Schnadt for our fruitful collaboration at the MAX IV laboratory. In this regard, I would also like to express my appreciation towards Karina Thånell and Karsten Handrup for keeping the I331 beamline in excellent shape.

As I have learned, maintaining a Ph.D. position requires a great deal of paperwork and bureaucracy. I sincerely thank Patrik Wirgin and Anne Petersson Jungbeck for guiding me through all that. Patrik, I have appreciated our many discussions about highs and lows. I would like you to know that a lunch table without you is a less interesting lunch table. Keep it spinning.

Per Westlings Minnesfond and Admire Research School are acknowledged for financial support as well as for providing many opportunities for meeting new friends and collaborators.

I would like to thank Edvin for hosting the annual kick-off and his enthusiasm for bananas. He is also acknowledged for his trust in my manuscript-preparation skills.

Sean Harrington and Jay Logan, I have appreciated our many fruitful discussions during conferences and research visits.

To Niclas Johansson and Lisa Rullik, your friendship has been appreciated. A special thanks go to Smisklas for allowing people with higher charisma to do the talking in important situations.

Martin Hjort, Erik Mårsell, Filip Lenrick, and Daniel Jacobsson are acknowledged for their enthusiastic sharing of disgusting beer, epic pizza roulette fails, and general silliness. In this regard, I have to give special thanks to Martin and Erik for their resilient, almost intrusive, need to share beverages in the late early evenings, as well as for sharing my fascination of the f-word and activities involving ginger.

I extend my appreciation towards Sanna Hammarberg for being an excellent officemate and for her encouraging conversations.

Olof Persson and Sarah Blomberg are acknowledged for being inspirational office neighbors. Olof deserves a special appreciation for putting up a fair fight in our Pretzel contest.

Elin Grånäs and Andreas Schaefer, you have both, although rarely at the same time, contributed to the characteristic s-ljus spirit. It has not been quite the same since you left.

PO Zetterberg and the people behind the Physics and Laser Show deserve my gratitude for providing many laughs and teaching me about the importance of a safe laboratory environment. My time at Lund University has been infinitely more enjoyable because of you. A special thank goes to Johan “Dr. Z” Zetterberg for his friendship and support as well as the informative demonstrations on the importance of size and dimensions. Moreover, to Odd, we always hoped for your return to make the group hole again, it was not quite the same without you.

Unn “*var e domkyrkan*” Dahlén, Cissi “*the cyborg*” Jönsson, and Odd Hole, I thank you for not letting first impressions decide the outcome of friendships.

I thank Jarle Kalberg, Niclas Johansson, Robin Swärd, and Odd Hole for their jolly cooperation in times of distress. Special thanks are extended to Jarle who have impacted my life in many ways, including the “*Jarlehål*,” “*Jarleroten*,” “*Jarleposen*,” and you even have your own “*Jarlerum*” in my house. Your knowledge about all things 4 cm have also been indispensable for the completion of this dissertation. You and Odd are also recognized for our many inspirational visits to kaavhuset.

Freddie Holmgren is acknowledged for having his hat.

I would also like to thank my “*Kennelmammor*” for giving me the opportunity to refurbish my house, as well as allowing me to leave the “*Jägarlöken*” earlier than what is appropriate.

I express gratitude towards my family for their unconditional support. Mom and Dad, I cannot thank you enough. I always have the three words in the back of my mind. A special appreciation goes to Lillfjompan for her generous sharing of sweets and for always being able to provide new perspectives to my life.

Agneta, I will never forget our taco-evening.

To Monka: Tack.

I thank Arne and Astrid Stenvall for taking the time to do all the things we could not find the time for; the “*silvrväska*” is much appreciated.

Special thanks to Arne and Arne for extending the lifespan of Ran. Ran you are the source of many good memories and are sorely missed. Your Eigen frequency will for always resonate with the Swedish House Mafia.

Finally, I would like to extend my most profound gratitude to Anna Stenvall for her diode-like appreciation for our playtesting, Caipirinha-evenings, “*grejor*,” tasty food, and silly jokes. You have always supported me, even when I run out of minerals. I also express thanks to my daughter Alva, for teaching me to function with minimal sleep; that ability has been very convenient these last few weeks.

ABBREVIATIONS AND SYMBOLS

1D, 2D, 3D	One-, two-, and three-dimensional
(hkl)	Miller index notation for a specific plane
{hkl}	A family of equivalent plane
[hkl]	A specific direction
⟨hkl⟩	family of equivalent directions
{111}A	Group III terminated {111} surface in Zb crystal
{111}B	Group V terminated { $-1-1-1$ } surface in Zb crystal
III-V	Compound comprised of one group III-element and one group V-element in the periodic table.
CB	Conduction band
CITS	Current-imaging tunneling spectroscopy
CP	Close proximity
DOS	Density of states
E_F	Fermi energy
E_g	Bandgap
FIB	Focused-ion-beam
IDOS	Integrated density of states
I_{set}	Setpoint tunnel current
LDOS	Local density of states
LED	Light-emitting diode
MBE	Molecular beam epitaxy
MOVPE	Metal-organic vapor phase epitaxy
NW	Nanowire
QD	Quantum dot

QW	Quantum well
STM	Scanning tunneling microscopy
STS	Scanning tunneling spectroscopy
SEM	Scanning electron microscopy
TIBB	Tip-induced band bending
TEM	Transmission electron microscopy
TPS/TSL	Twinplane superlattice
V_T	Sample bias for STM imaging
U_{set}	Setpoint bias for STS.
U_{ext}	Externally applied bias in NW devices.
UHV	Ultra high vacuum
VB	Valence band
Wz	Wurtzite
XPS	X-ray photoelectron spectroscopy
Zb	Zinc blende
z	Tip-sample separation

1 INTRODUCTION

The advent of semiconductor physics in the early 19th century ignited a technological revolution which ultimately would result in the realization of electronics components which are vital for modern day computers, solar cells and light emitting diodes (LEDs). The technological leaps that have occurred during the last few decades come as a result of improved semiconductor technology and in the case of computers, the downscaling of transistors to the nano-regime.

A promising type of nanostructure for energy harvesting, light emission, and electronics are III–V semiconductor nanowires (NWs). NWs are self-assembled nano-shaped crystalline rods with diameters commonly measured in tens of nanometers and lengths measured in micrometers. The so-called III–V semiconductors consist of materials from group III (*e.g.*, In and Ga) and V (*e.g.*, As, and P) of the periodic system. Most of the III–V materials have advantages to the more conventional semiconductor material, Si, such as direct bandgaps, a higher charge mobility, and tunable bandgap sizes. These properties make III–V materials optimal for high-performance electronics [1-6], photonics [7-10], and energy harvesting [10-14]. Recent progress towards combining III–V NWs with existing Si-technology—and also the small amounts of material needed for NW growth—allows for cheaper manufacturing costs relative to the conventional planar geometries [15, 16].

A fundamental property of a semiconductor is the ability to locally control the electronic properties and conductivity *via* for instance material heterostructures and doping. The 1D nature of NWs allows for additional dimensions when constructing heterostructures; junctions can be formed both axially, along with the growth axis, and radially, perpendicular to the growth axis, providing new degrees of freedom for controlling and designing the electronic landscape of semiconductor devices [17, 18].

NWs also provide a unique ability to control the electronic structure *via* so-called crystal phase engineering [19]. Instead of, as traditionally, varying the material composition to achieve the desired electronic properties, the crystal structure can be changed instead. In contrast to most III–V bulk materials, NWs can be grown in both the cubic zinc blende (Zb) as well as the hexagonal wurtzite (Wz) crystal structure, which are predicted to have different bandgaps [20]. The advantage of crystal phase heterostructures over traditional material junctions is the ability to achieve perfectly atomic sharp interfaces, something which is intrinsically difficult

with material junctions [21]. The quality of the heterostructure interfaces is of fundamental importance for the performance of semiconductor devices. Also, unintentional crystal phase mixing is reported to have detrimental effects on the device performance, and atomic level control and characterization of crystal phase interfaces are thus fundamental for the function of NW devices [22, 23].

As a consequence of the nano-scale dimensions and rod-shaped geometry, NWs have an inherently large surface-to-bulk ratio, making NW devices much more sensitive to surface effects compared to larger-scale components. In fact, the electronic and optical properties of NWs are greatly influenced—and in some cases dominated by [24, 25]—the surface morphology [26–28], surface defects [29–34], and surface states of the NW side facets. Also, the surface morphology and atomic structure play an important role in the controlled growth of radial heterostructures (*i.e.*, core–shell NWs), quantum dots (QDs), and quantum wells (QWs). These issues are further complicated since the morphology and types of defects may vary depending on the crystal structures and facet types of the NWs [35–38]. Characterization of surface effects—their nature, and origin—thus play a crucial role in determining and manipulating the NW properties. Despite this, the correlation between electronic, morphologic, and structural properties of III–V NW surfaces is poorly understood. This issue stems from the difficulty of differentiating between the surface and bulk contributions to the electronic properties, as well as the chemical composition, of NWs with methods conventionally used for nanometer-scale characterization such as contact-electrical measurements, transmission electron microscopy (TEM), and photoluminescence (PL) measurements. On the other hand, standardized surface characterization tools such as the scanning tunneling microscope (STM) and scanning tunneling spectroscopy (STS)—which in combination are capable of atomic-scale characterization of morphologic and electronic structure—are traditionally limited to extremely flat samples, with roughness on the Å-scale. To image NW structures with diameters of tens or hundreds of nanometers is challenging.

The primary goal of my work has been to characterize surfaces of III–V NWs with the purpose to correlate electronic, morphologic, and structural properties, both on the micrometer-scale as well as on the atomic level. To this end, I have studied electronic properties of crystal phase interfaces as well as complex NW surfaces and how they can be overgrown and modified. The bulk of my work has focused on the GaAs and InAs material systems. The chemical composition of NW surfaces was studied using x-ray photoelectron spectroscopy (XPS), which is capable of detecting elements and chemical compounds with high precision and for large sample sizes.

This dissertation consists of two main parts: an initial introductory section containing several chapters, each debating a topic relevant to the work behind this dissertation. The second part is constituted by a collection of papers that are the result of that work. The chaptered section is built up as follows:

In chapter 2, an introduction to the STM, the main experimental method used for the work behind this dissertation, is provided. This includes basic theory, image interpretation as well as optimal settings for imaging III–V NWs. I will also discuss how to prepare tips suitable for imaging on NWs.

In chapter 3 an introduction to STS is provided, a method that was used for several papers included in this dissertation. Different modes of operation as well as data treatment and interpretation are debated. Effects of sample temperature, surface defects, and tip-induced band bending are also discussed.

In chapter 4, the surface characterization of the chemical composition of III–V NWs *via* XPS is discussed. The method was used mainly for Paper **VII**. A brief background on theory and experiment, as well as data treatment and interpretation, is provided.

In chapter 5 an introduction to III–V NWs, their growth, and morphology, is provided. The growth and characterization of heterostructures—formed by either material or crystal structure junctions—are discussed down to the atomic level. Similarly, the electronic properties of different crystal phases, as well as quantum confinement within crystal phase QDs and QWs, are discussed.

In chapter 6, the atomic level surface characteristics of the NW facets, both structural and electronic, are discussed.

In chapter 7, sample preparation, in terms of NW transfer and native oxide removal, is discussed. The chapter also deals with NW surface modification in the form of Bi-incorporation in GaAs NWs for altering the local electronic properties in the surface region.

In chapter 8, means for atomically resolved *operando* STM/S measurements of externally biased NWs are discussed. The chapter also includes a discussion on electromigration, an effect where adatoms “diffuse” along the potential gradient on the surfaces of externally biased NWs.

In chapter 9, the work is summarized in the context of the available literature and describes some possible routes for future NW surface science studies.

2 SCANNING TUNNELING MICROSCOPY

This chapter deals with an introduction to the STM, including theory and image interpretation as well as tip preparation and instrumental settings. A sub-section including the particulars of STM imaging of NW structures is also provided. STM experiments have been an integral part of my work; in fact, all the publications that are included in this dissertation have relied on structural or electronic information to be provided by STM.

The STM is an experimental tool which allows for surface mapping of the physical and electronic structure of surfaces with atomic resolution. It was invented in 1982 by Binnig and Rohrer in collaboration with Gerber and Weibel [39-41]. It is based on the quantum mechanical tunneling effect: a phenomenon which allows electrons to pass (tunnel) through potential barriers without having sufficient energy to overcome them classically. The STM allows for real space imaging of topographic and electronic properties of conducting or semiconducting surfaces with atomic resolution. The method has, since its invention, revolutionized the field of surface science.

In STM, an atomically sharp metal tip is attached to a piezo drive and brought close, typically within 10 Å, to a conductive surface, see Figure 2.1. Upon applying a bias, V_T , between tip and sample a tunneling current, I_T , with typical magnitudes in the range of pA–nA, will flow between them. The magnitude of the tunneling current has been shown to decrease exponentially with the tip–sample separation, z , [40]:

$$I_T \propto e^{(-2z\kappa)}, \quad (2.1)$$

where κ is the inverse electron decay rate:

$$\kappa = \hbar^{-1}(2m\phi)^{\frac{1}{2}}, \quad (2.2)$$

where m is the electron mass, \hbar is Planck's constant, and ϕ is the effective local work function, which in turn depends on the sample bias, V_T . The exponential decay of the tunneling probability with respect to z ensures a sub-Å vertical resolution in the STM. A very high lateral resolution can be obtained since the majority of the tunneling current will flow between the outermost atom of the tip and the closest atom of the surface.

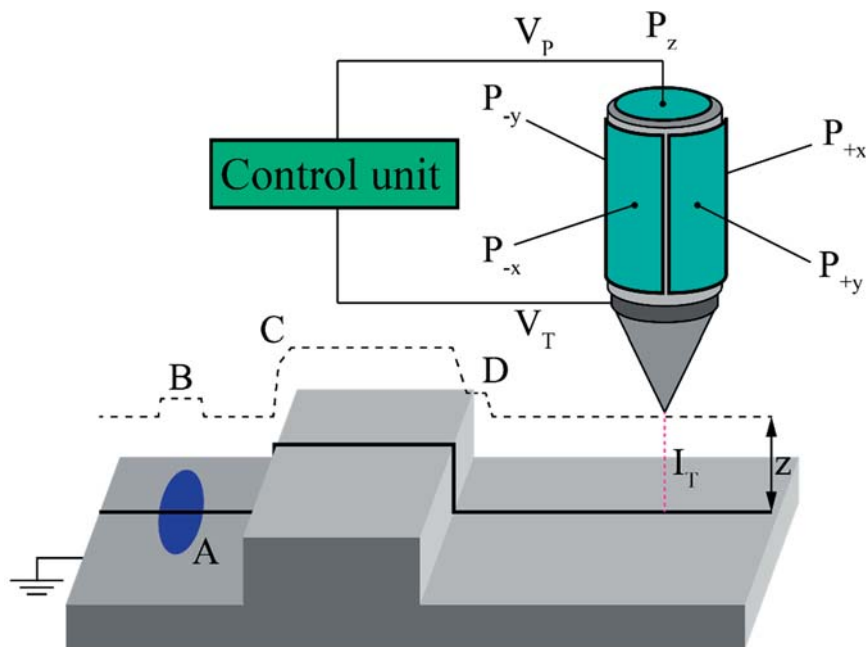


Figure 2.1 A schematic representation of an STM setup. The size of the objects is not to scale. The tip movement in the x -, y -, and z -directions is controlled *via* piezoelectric elements (P). For a given setpoint voltage (V_T) the tunneling current (I_T) is kept constant by varying the tip-sample separation (z), which in turn is controlled by the bias (V_P) applied to the z -element (P_z). The resulting changes in tip-height (dashed line) are recorded to form an image of the surface topography. Irregularities in the surface potential (A) will give rise to variations in the tip height (B). The shape of the tip will influence the recorded topography; similar geometric shapes may appear different depending on their relative orientation to the tip, (C) and (D). Image inspired by the work of Olof Persson, who deserves “*fat stacks of credit.*”

By raster scanning the tip over the sample surface and monitoring the current, an image of the surface can be created. In general, a constant current mode is used in which a feedback loop, controlling the tip height, keeps the tunneling current constant during scanning. Both the tunneling current and tip-sample voltage are kept constant in this imaging mode and are referred to as the setpoint current (I_{set}) and setpoint voltage (V_T), respectively. The relative tip height is recorded for each spatial position and used to form an image. The image contrast is based on topographic as well as electronic features of the surface. This duality can make interpretation of images somewhat challenging, but can also provide valuable information. A sound understanding of the tunneling process is required to distinguish between the two sources of contrast. In general, topography tends to be the dominating contrast mechanism for images with large height variations whereas electronic structure is dominating for flat surfaces.

2.1 Theory

Classically, electrons cannot pass through a potential barrier unless sufficient energy is provided. Quantum mechanics, on the other hand, allows for the electron to be viewed as a wave function—having a distribution in space—which may propagate through sufficiently thin barriers. For two adjacent material systems, separated by a vacuum, such as an STM tip and the investigated sample, the vacuum will act as a potential barrier, preventing electrons from being exchanged between the systems. However, for systems separated by sufficiently small distances, the wave functions of electronic states at the system surfaces may overlap. The overlap will result in a non-zero interaction probability of the tip and sample states such that electrons can be transferred from one system to the other. This process is referred to as tunneling and is the fundamental phenomena upon which STM is based.

As stated by Fermi's golden rule, the probability, T , of an electron to tunnel between tip and sample can be expressed as:

$$T = \frac{2\pi}{\hbar} |M_{i,f}|^2 \delta(E_i - E_f), \quad (2.3)$$

where the δ -function state that the tunneling probability between the initial (E_i) and final state (E_f) is non-zero only for electronic states of the same energy. $M_{i,f}$ is the tunneling matrix element between the initial and final state. By adopting Bardeen's theory of tunneling [42, 43], the tunneling matrix can be approximated; it assumes that electron-electron interaction is ignored, and that tip and sample have an independent and constant occupation probability. As shown below, the matrix element can be described as an integral over an arbitrary surface, S , located in the region between tip and sample:

$$M_{i,f} = -\frac{\hbar}{2m} \int (\psi_i \nabla \psi_f - \psi_f \nabla \psi_i^*) dS \quad (2.4)$$

where ψ_i and ψ_f are the wave functions of the initial and final states respectively (*i.e.*, tip and sample states), ψ_i^* is the complex conjugate of the initial state wave function, and m is the electronic mass.

Using Bardeen's expression for the tunneling matrix, Tersoff and Hamann described the tunneling current using first-order perturbation theory [44]:

$$I_T = \frac{2\pi e}{\hbar} \sum_{i,f} f(E_i) [1 - f(E_f + eV_T)] |M_{i,f}|^2 \delta(E_i - E_f) \quad (2.5)$$

where $f(E)$ is the Fermi distribution function. The equation implies that tunneling only occurs from occupied to empty electronic states. However, in most cases the wave functions ψ_i and ψ_f , needed to calculate $M_{i,f}$, are not known. To estimate the

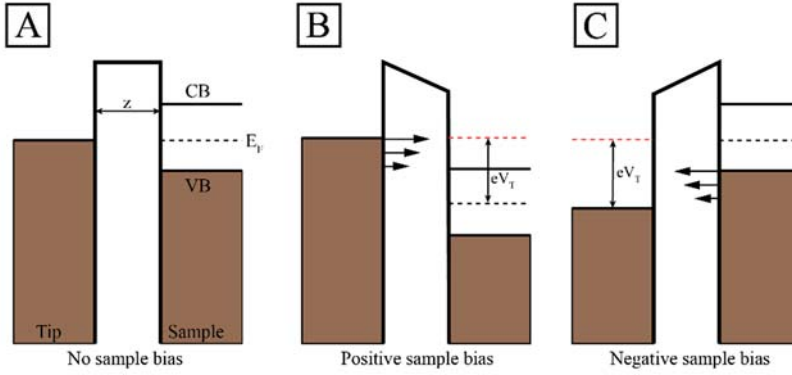


Figure 2.2 Illustration of the flow of the tunneling electrons depend on the polarity of the applied sample bias V_T . Conduction band (CB), valence band (VB), and Fermi level E_F are marked in the figure.

tunneling current several assumptions must be made; an “ideal” tip is conventionally described as having a low temperature, a spherical tip apex—being geometrically and electronically isotropic—and that an s-like wave function is dominating the tunneling current. By these assumptions Tersoff and Hamann showed that the tunneling current is proportional to the integrated density of states (IDOS) in an energy interval between the Fermi level, E_F , and $E_F + eV_T$ at a position r_o of the tip [45]:

$$I_T \propto \rho_t \int_{E_F}^{E_F + eV_T} \rho_{s,loc}(\vec{r}_0, E_F + \varepsilon) d\varepsilon \quad (2.6)$$

where ρ_t is the local density of states (LDOS) of the tip apex and $\rho_{s,loc}$ is the LDOS of the sample at a position r and energy E .

2.2 Image contrast

For images obtained on flat surfaces using a constant current mode, the main contrast mechanism is local variations in the LDOS of the sample. A larger number of states will result in an increased tunneling current and thus show up as a brighter area in the STM image and vice versa for dark areas. As shown in equation (2.6), only states in the energy range of $E_F + eV_T$ contribute to the tunneling, inferring that filled and empty states are imaged separately depending on the polarity of the applied bias, V_T , as illustrated in Figure 2.2. However, if eV_T is smaller than the thermal energy ($k_b T_{temp}$) only states within $E_F + k_b T$ will contribute to the tunneling.

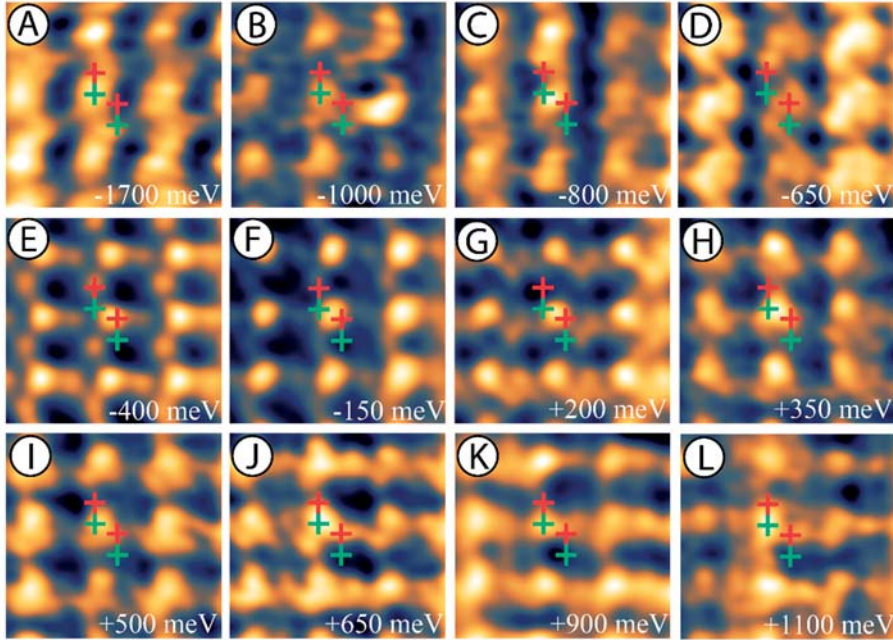


Figure 2.3. Atomically resolved STM images of an $\{11\bar{2}0\}$ -type InAs surface at various tip-sample biases. The images are obtained at the same position and with the same tip. The red and green crosses denote the expected position of As and In atoms, respectively, as based on the protrusion maxima in (A). It can be noted that for -800 mV to $+350$ mV the protrusion maximum is shifted slightly relative the images obtained at higher energies.

The polarity-dependent tunneling is especially useful when studying some III-V systems as, for most surfaces, the filled and empty states are localized at the group V and III atoms, respectively, making it possible to study states specific to each element [46, 47].

Metals generally don't have any strong variations in LDOS near the Fermi level resulting in an image contrast that is relatively independent with respect to the imaging bias, V_T . The same is not true for semiconductors which usually have a very strong variation in LDOS near the Fermi level, which can result in contrasts which do not correspond to topographic features. It is thus recommended to use a number of biases when imaging semiconductors to determine the influence of the electronic structure. For most systems, however, using a large sample bias, (*i.e.*, integrating over many energies) will result in an STM image dominated by topographic features since the majority of electronic states are localized around the atoms. In contrast, by using low sample biases, (*i.e.*, taking fewer states into account), individual states become increasingly more dominant. In the low-bias case, the image contrast may be dominated by a few or even single electronic states of the surface. This phenome-

Table 2.1. Typical STM settings for imaging InAs and GaAs NWs when using an {111}B-type. The settings are based on using the constant current mode at room temperature. Loop gain refers to the integral-part of the feedback regulation speed.

Effective Scan speed [nm/s]	Loop gain [%]	Voltage [V]	Current [pA]
100–300	4–10	–2 to –4	10–100

non is demonstrated in Figure 2.3 where STM images obtained at different biases are shown. The images are obtained at the same spatial position—and at 5 K to minimize thermal drift—and depict an atomically resolved {11–20}-type surface of an InAs NW side facet. The position of the protrusions, as well as the spatial pattern, undergo several changes and shifts when going from higher to lower energies.

To make matters even more complicated, changes in contrast patterns similar to those seen in Figure 2.3 can be induced by changes in the tip apex geometry or electronic configuration. The image contrast depends not only on the LDOS of the sample but also of the tip. However, the LDOS of the tip can most often be neglected since the same part of the tip is used for tunneling (*i.e.*, it is constant), in contrast to the sample where new spatial positions are continuously imaged. Hence, a slight change in geometry of the tip apex could result in an altered contrast pattern. Also, the electronic configuration of the outermost atom of the tip apex could be changed—for instance the “optimal” *s*-like orbital assumed in the Tersoff Hamman approximation could change to a *p*-type orbital—which could result in different states being probed [48]. Not only geometry but also the chemistry of the tip can be changed; it is possible for adatoms from the surface (or in the atmosphere) to adsorb on the tip apex such that the majority of the tunneling current goes through that particular atom. Such tip-changes can drastically change the contrast behavior, especially if the adsorbed atoms result in a tip apex with insulating or semiconductive characteristics. It is thus of vital importance to be aware of any tip changes when performing atomic resolution imaging.

2.3 Imaging nanowires with STM

The STM is an ideal tool to study flat surfaces with extreme spatial resolution. However, imaging samples with height-variations larger than a few nanometers, such as NWs, can be quite challenging and imposes some restrictions on the imaging parameters, tip geometry, as well as the STM operator.

My preferred method of locating NWs is to use coarse movement in combination with a slow-scanning STM tip. For a given position on the sample, only one scan li-

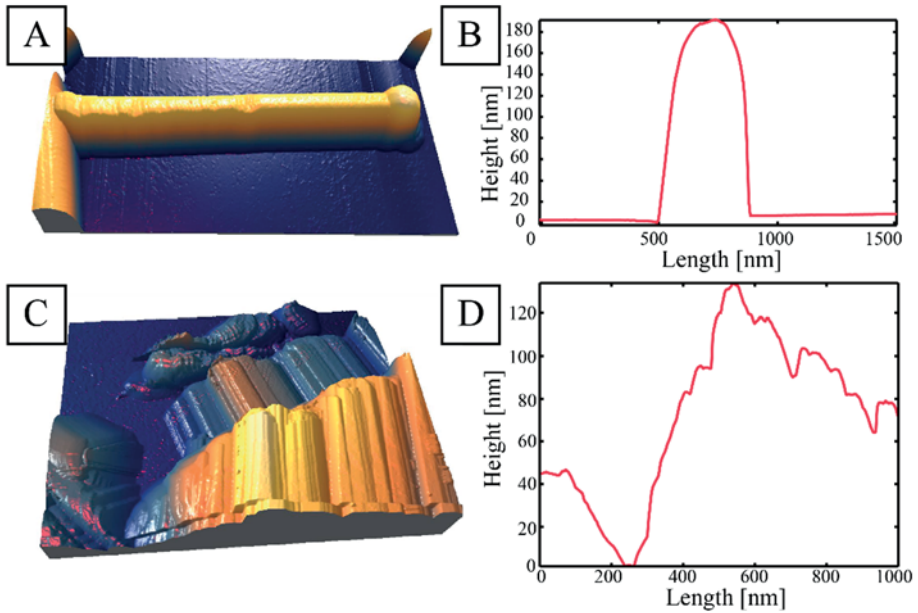


Figure 2.4. STM imaging of NWs often results in a broader NW than expected. (A) 3D render of an STM image depicting an InP NW obtained using a relatively sharp tip. The Au particle is visible to the right. (B) Line profile over the NW. The height is approximately 180 nm and the apparent width 400 nm. (C) 3D render of an STM image depicting a GaAs NW. A relatively blunt tip is used, resulting in a very broad NW with many “copies” due to tunneling contribution from many different parts of the tip. (D) Line profile over the NW in (C).

ne is obtained. From the scan line it is possible to determine if a NW is within reach; if it is not, the tip is relocated to another part of the sample *via* a course movement step. This process is repeated until a NW is found.

When a NW is found, the piezo movement (limited by scan range) is used to traverse on top of the NW to locate the top facet. For this process, it is recommended to use low currents (*i.e.*, large tip–sample separation), fast feedback and slow scan speeds to avoid tip-crashes. In Table 2.1, I have summarized typical settings that I have used for imaging GaAs and InAs NWs deposited on their respective $\{111\}$ B-type substrate.

The resulting image of large objects in STM will consist of a convolution of the object itself and the STM tip. As such, the observed diameter of a NW is, in fact, the actual NW diameter convoluted with the tip shape. For a blunt tip, this can give rise to NWs with an apparent diameter which is significantly larger than the actual diameter, as demonstrated in Figure 2.4. Also, when imaging samples with corrugation on the 100 nm scale, several parts of the tip can contribute to the tunneling current. This effect will make image interpretation challenging as multiple

copies of the NW will show up in the image, often overlaid on top of each other. For this reason, it is preferable to use the sharpest tip available when imaging NWs. Also, it is recommended to use the height of an object rather than its apparent diameter when determining (from a line scan) if the object corresponds to a NW or something else, such as a crystal fragment. Due to the broadening-effect, locating the NW top-facet tends to be the most challenging part when imaging NWs. When trying to locate the top NW facet, it is recommended to turn off the automatic slope subtraction (if it is in use), since it will give false information due to the curvature of the broadened NW. Also, it is recommended to use a differentiated version of the STM image to make it easier to compare features at different heights and angles.

2.4 Tip preparation

The tips used for most of my work were made in-house *via* electrochemical etching of 0.38 mm tungsten-wire. The etching was done using a DC-setup with a 2 mol/liter sodium hydroxide (NaOH) solution. The current-cutoff was controlled *via* a commercial Omicron tip etching control unit. Post-etching procedures involve rinsing the tips with distilled water and ethanol to remove NaOH-residues, as well as removal of surface oxides *via* argon-sputtering. The sputtering was performed for 2×15 min in a vacuum chamber with an argon-chamber pressure of 1×10^{-6} mbar (and a base pressure of 1×10^{-9} mbar). The sputter-gun was set to a 3 kV acceleration voltage and a 20 mA emission current. This preparation procedure typically results in sharp tips with small tip curvature that is suitable for STM imaging of samples with large height variations such as NWs.

3 SCANNING TUNNELING SPECTROSCOPY

The use of STS has been paramount for obtaining the results presented in several of the papers included in this dissertation. In particular, for obtaining experimental bandgap values of the Wz crystal structure of GaAs and InAs materials. STS was also used for investigation into the limits of the crystal phase dependent electronic structure, down to the single bilayer level. This chapter deals with the theory and practice of STS measurements, particularly in the context of NW surfaces. The chapter also contains introductions to the concepts of data treatment and interpretation, including how to account for tip-induced band bending (TIBB). The intricacies concerning room-temperature *versus* low-temperature measurements—and their respective advantages for NW experiments—is also discussed.

STS is a powerful tool, capable of probing the LDOS as a function of energy, and with an atomic-scale spatial resolution [49, 50]. The spectroscopic method is, in fact, a collective name for a number of techniques, such as current (I–V) spectroscopy [51, 52], differential conductance (dI/dV–V) spectroscopy [53], and spatial LDOS mapping *via* spectroscopic imaging techniques such as current-imaging tunneling spectroscopy (CITS) [54] and differential conductivity imaging [55, 56]. The main advantage that these techniques hold over the traditional and spatially averaging spectroscopy techniques, such as PL or contact-electrical measurements, is its capability to obtain topographic and electronic information with atomic resolution simultaneously. The STS techniques have proved to be invaluable for characterizing the electronic properties of dopants and defects [57, 58], quantum phenomena [59-61], and bandgaps and band offsets of semiconductor materials [35, 62, 63].

In current (I–V) spectroscopy, the STM tip is kept at a fixed position with the feedback loop disengaged, and the tunneling current is recorded as a function of the tip–sample bias. If the equation for the tunneling current, equation (2.6), is rewritten to account for a constant tip–sample separation, and the position dependency is removed, an equation with the tip–sample voltage, V_T , as the only variable is obtained:

$$I_T(V_T) \propto \int_{E_F=0}^{eV_T} \rho_s(E_F + \varepsilon) d\varepsilon \quad (3.1)$$

Table 3.1. Typical settings used for the room temperature (300 K) and low-temperature 5 K setups when performing spectroscopy. These values are general, and circumstantially they may not be viable. The z-modulation parameter will be explained in section 3.1.

Temperature	Modulation frequency [Hz]	Modulation amplitude, ptp. [meV]	Time constant [ms]	Raster time [ms]	z-modulation [$\text{\AA}/V$]
300 K	1000–1200	50–100	10–30	30–60	1–2
4 K	700–1200	5–15	20–100	60–300	1–2

As implied by equation (3.1), the tunneling current at a given tip–sample voltage is proportional to the IDOS in an energy range between the Fermi level, E_F , and sample energy, eV_T . By sweeping (*i.e.*, varying V_T) the tip–sample voltage, the IDOS can be obtained as a function of eV_T . By sweeping from negative to positive voltage values, the IDOS of filled and empty sample states, below and above the Fermi level, respectively, is obtained. In this fashion, the IDOS of the sample can be obtained as a function of energy by simultaneously sweeping the tip–sample bias and recording the tunneling current.

However, for most applications, the LDOS—meaning the density of states at each given energy—is of more relevance. A quantity that is proportional to the LDOS can be obtained by differentiating the current-spectrum with respect to the tip–sample voltage, such that $dI/dV-V$ is obtained [64]. The differentiation of $I-V$ can be done numerically, but at the cost of high noise levels. Instead, it is preferentially obtained experimentally in parallel to the $I-V$ signal *via* a lock-in amplifier.

I have used the lock-in technique, in which a small sinusoidal modulation, dV , is superimposed onto the D.C. tip–sample voltage. From the resulting modulated component in the tunneling current, dI , the differential conductivity $dI/dV-V$ is directly obtained. Larger amplitudes for the modulation signal result in a higher signal to noise ratio at some cost to the spectral resolution. The modulation frequency should be chosen to be higher than the bandwidth of the STM system to avoid feedback response in constant current mode. Additionally, the integration time (time constant), T_c , of the lock-in amplifier should be set to be high enough to allow for several cycles of the modulation signal to be included in the integration. More cycles will reduce noise. Similarly the raster time, T_{raster} , of the STM (time measured at each point in the spectra) should preferentially be set to 2–3 times the time constant of the lock-in. However, for room temperature measurements a problem arises when obtaining spectra with long acquisition times; during the acquisition of a spectra the tip–sample separation will continuously, and in an unknown fashion, change as a result drift in the piezoelectric elements that control tip positioning. Such drift would make a quantitative characterization of the spectra

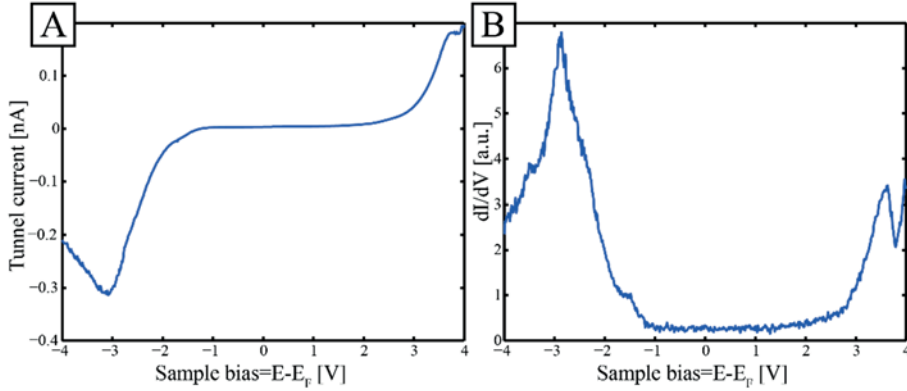


Figure 3.1. Unmodified I–V(A) and dI/dV–V (B) data obtained from a {11–20}-type surface of a GaAs NW. The Fermi level is located at 0 V. Valence and conduction band edges can be found at roughly –1 V and +2.5 V, respectively, $U_{\text{set}} = -4$ V. The large band gap is due to TIBB.

difficult. As a result, an optimization between two effects with opposite requirements is necessary at room temperature, *i.e.*, long acquisition times to reduce noise or short acquisition times to reduce piezo drift. Typically, the time constants are kept low for room-temperature measurements to minimize the effects of piezo drift. Typical settings for room- and low-temperature measurements are summarized in Table 3.1.

Examples of I–V and dI/dV–V curves from a GaAs surface are shown in Figure 3.1. The Fermi level is intrinsically located at 0 V. Filled, and empty states are thus found at negative and positive bias, respectively. The bandgap is located at energies between –1 V to +2.5 V, and the location of the Fermi level—closer to the valence band—suggests a lightly p-doped surface. The large band gap is due to TIBB, an effect increases the apparent band gap of semiconductors when probed with STS. The effect will be discussed in detail in chapter 3.3.

It is recommended to always obtain an image of the area of interest before and after a spectroscopy session to ensure that the sample (or tip) has not changed during the STS measurements. To ensure that the intended position is probed when performing single point STS measurements at room temperature—where thermal drift is significant—it is advisable to obtain each spectrum at the currently acquired scan line in an active STM image.

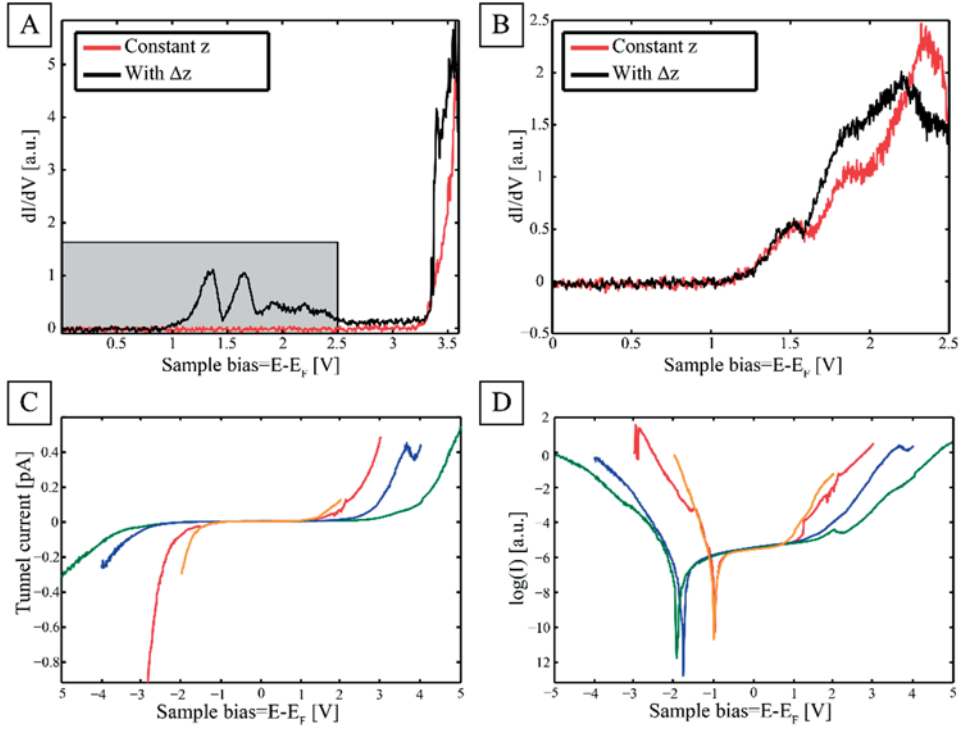


Figure 3.2. STS obtained at the same position, with and without variable z , on a GaAs{111}B surface with 0.5 ML of Bi deposited on top. (A) A large energy range spectrum with a visible conduction band edge at around 3.3 eV. The low LDOS gap states are only visible in the spectrum obtained using variable z , *i.e.*, a large dynamic range is required to resolve the gap states. $U_{\text{set}} = 3.6$ V. (B) Spectra with a smaller energy range (marked by the grey box in (A)) where the high LDOS of the conduction band is not included. As a result, no major differences can be seen between constant z relative to variable z modes. $U_{\text{set}} = 2.5$ V. For all spectra $I_{\text{set}} = 200$ pA. $\Delta z = -0.9$ and -0.35 nm for (A) and (B), respectively. Figures (C) and (D) demonstrate the apparent increase in bandgap size when using larger setpoint voltages in constant- z mode. (C) four I - V -spectra obtained at the same position—using the same setpoint current—but different setpoint voltages, $U_{\text{set}} = -2, -3, -4,$ and -5 V (green, blue, yellow, red), respectively. $I_{\text{set}} = 300$ pA. (D) shows the same spectra but on a log-scale to more clearly visualize the band onsets. The four spectra all appear to have different band-onset positions.

3.1 Variable z mode and data treatment

STS measurements of semiconductor samples are often performed over large voltage ranges to accommodate both valence and conduction band states within a single spectrum. To not saturate the STM electronics, a large setpoint voltage (*i.e.*, a large tip-sample separation) is required when probing the band-states. In the context of STS, the stepoint voltage refers to the starting voltage value used for obtaining a spectrum, denoted as U_{set} . Consequently, when using a large setpoint voltage, the current-signal from the band onsets and possible mid-gap states is significantly reduced due to their low LDOS relative to the valence and conduction bands. In fact, a dynamic range corresponding to several orders of magnitude is required to measure gap states, band onsets, as well as in-band features within the same spectrum due to the exponential dependence of the current on the voltage.

To increase the dynamic range, I commonly used the variable z-mode, where the tip-sample separation is continuously changed while recording the tunneling spectra [65]. Without increasing acquisition time, a dynamic range of up to six orders of magnitude can be achieved using this method, corresponding to an improvement of 2–3 orders of magnitude compared to STS recorded at constant tip-sample distances [53]. In variable z-mode, the feedback loop is disengaged as normally, but instead of using a constant tip-sample separation, z_0 , the separation, z , is varied linearly as a function of the applied bias, V_T :

$$z(V_T) = z_0 - a(|V_0| - |V_T|) \quad (3.2)$$

Where $|V_0|$ is the absolute value of the setpoint voltage (starting value), a is a displacement factor which is set by the operator, and z_0 is the tip-sample separation at $V_T = 0$ V. The tip-sample separation decreases for lower voltage values. Typical values of the displacement factor are, $a = 2$ Å/V.

As demonstrated in Figure 3.2, the dynamic range of constant-z spectroscopy is not large enough to probe both the low-LDOS gap-states and the significantly stronger conduction band states. However, a negligible difference is found for the variable- and constant-z modes when probing a smaller energy range where there are no drastic variations in the LDOS. For similar reasons, the apparent position of the band onsets may vary depending on the probed energy range when using constant-z mode; for the larger setpoint voltages the limited dynamic range cannot account for the low-signal onset-region due to the strong gradient in LDOS at the band edges. As a result, the bandgap size appears to increase for larger setpoint voltages when using constant-z mode.

A consequence of the variable-z mode is that the dI/dV -V signal will depend on both the tip-sample separation as well as the energy (voltage); quantitative comparison between features within, as well as between, spectra become

problematic as a result of having two variables. The tip-sample dependency can, however, be removed by normalizing the $dI/dV-V$ signal by the total conductance ($I-V$) [66, 67]. This can be illustrated by expressing the tip-sample dependent tunneling current, I_T , as a function of the tunneling current at a constant tip-sample separation, I_c :

$$I_T(V_T, z) = I_c(V_T)e^{-2\kappa\Delta z(V_T)}. \quad (3.3)$$

Similarly, the differential of the current can be expressed as:

$$\left[\frac{dI_T(V_T, z)}{dV_T} \right] = \left[\frac{dI_T(V_T)}{dV_T} \right]_c e^{-2\kappa\Delta z(V_T)}. \quad (3.4)$$

Here, κ is (in the lowest order of approximation) independent of z and V_T . By taking the ratio between equations (3.3) and (3.4), the exponential part of both equations will effectively cancel out. The resulting quantity, $(dI/dV)/(I/V)$, is proportional to LDOS and independent of the tip-sample separation. Note, however, that the above equations are low order approximations and as such a perfect normalization cannot be expected.

Although this process works fine for metallic samples, problems arise when normalizing semiconductor samples due to their low-LDOS region within the bandgap. Close to the band edges, the ratio tends to diverge towards infinity as a result of the current approaching zero faster than the conductance. The simplest way to work around this problem is to add a constant to the total conductance. Instead, I have opted to use a slightly more sophisticated technique where the total conductivity is broadened by an exponential function similarly to what was described by Feenstra and Mårtensson [53, 68].

The broadened total conductance, $(\overline{I-V})$, is obtained by convoluting the conductance ($I-V$) by an infinite voltage integral and an exponential function (which have a broadening width of ΔV). This procedure is done for any given voltage value, V_T' , of the $I-V$ spectra:

$$\overline{I/V} = \frac{1}{2\Delta V} \int_{-\infty}^{\infty} \frac{I(V_T')}{V_T'} \exp\left(\frac{-|V_T' - V_T|}{\Delta V}\right) dV_T'. \quad (3.5)$$

In practice the integral is solved as a summation with more, computationally, realistic limits. The measured $I-V$ is extended by ΔV on each side, and the currents in this extended region are assumed to be constant and are set to correspond to the current-values recorded at the respective voltage limits of the spectrum. The summation limits are set to be the min/max voltages of the spectra, extended by the broadening function ΔV . Using this method, the only parameter that has to be set is the broadening factor ΔV , which should preferably be chosen to be in the order of the bandgap of the semiconductor in question.

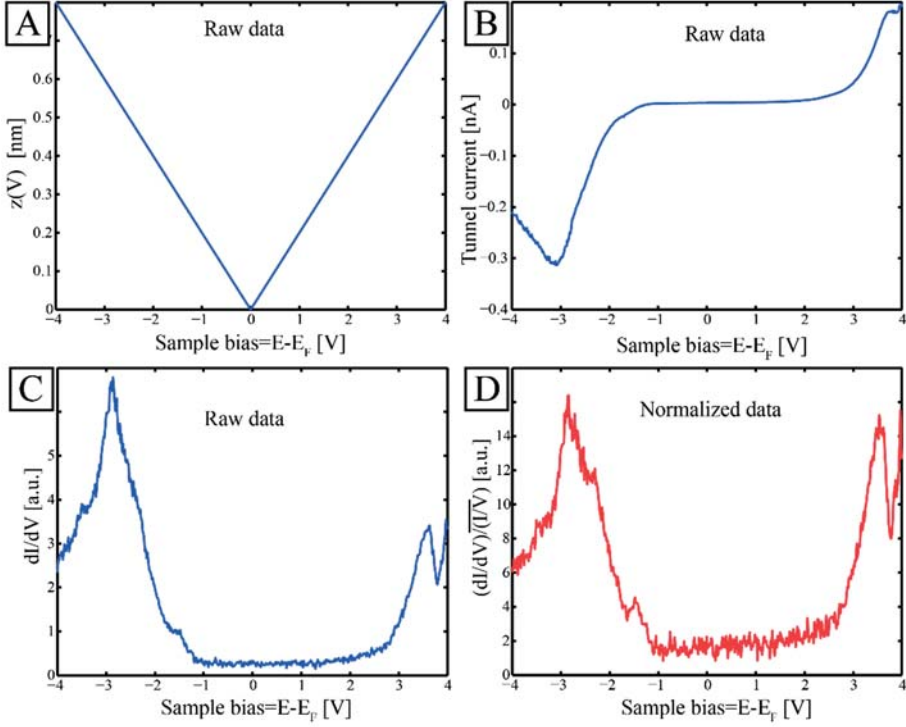


Figure 3.3. Illustration of the normalization procedure of the $dI/dV-V$ when using the variable- z mode. (A) tip-sample separation, z , as a function of energy. (B) Tunneling current as a function of energy. (C) $dI/dV-V$ as a function of energy. (D) $dI/dV-V$ normalized by the broadened tunneling conductance, *i.e.*, $(dI/dV)/(\overline{I/V})-V$. A broadening constant of $\Delta V = 2$ V was used.

The resulting ratio, $(dI/dV)/(\overline{I/V})$, corresponds to a quantity that is proportional to the LDOS and only has a negligible dependence on the tip-sample separation. For comparison, I show, in Figure 3.3, the $z(V)$ signal, current ($I-V$), differential conductance ($dI/dV-V$) as well as normalized differential conductance $(dI/dV)/(\overline{I/V})-V$. When comparing the differential conductance to the normalized quantity, it is possible to see that features far away from the Fermi level has been weighted down or up in accordance with the appearance of the $I-V$ spectrum.

3.2 Band edge determination

I have used a fitting procedure analogous to what is described in ref. [69] to consistently and precisely extract quantitative values of the band edges. First, the

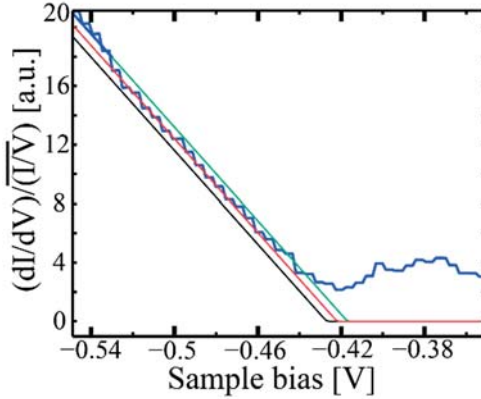


Figure 3.4. Determination of valence band edge at a $\{110\}$ -type InAs NW facet, obtained at 5 K. The red line represents a linear fit, modulated by a Gaussian broadening to account for temperature. The green and red lines represent an estimated error of ± 6 meV. Image adapted from Paper VI, [70].

band onsets must be identified, a procedure that can be non-trivial due to the presence of surface states; the respective LDOS of the band onsets and surface states can overlap. An experimental solution to this problem is to probe an area of the surface with a minimal number of defects; vacancies, adatoms, and step edges, *etc.*, are likely to give rise to surface states. Alternatively, spectra at several different positions can be obtained and compared to differentiate between surface features and onset states; the position of surface states is expected to change in energy depending on the vicinity to the defect (that is giving rise to the state) whereas the band onsets are expected to be constant throughout the measurements. Once the band onsets have been identified, the fitting procedure assumes a linear increase in LDOS at the onsets, as has previously been shown to agree well for the normalized differential conductance [53]. Temperature is taken into account *via* a Gaussian broadening. An example of such a fit is shown in Figure 3.4, where the valence band edge of a spectrum, obtained on the Zb $\{110\}$ -type surface of an InAs NW, has been fitted. An accuracy in the range of ca 30 meV and down to 3 meV can be expected for room temperature and 5 K measurements, respectively [53, 62].

3.3 Tip-induced band bending

Quantitative description of the tunneling spectra of semiconductors is often impeded by their dielectric nature, where some of the applied tip-sample voltage drops in the

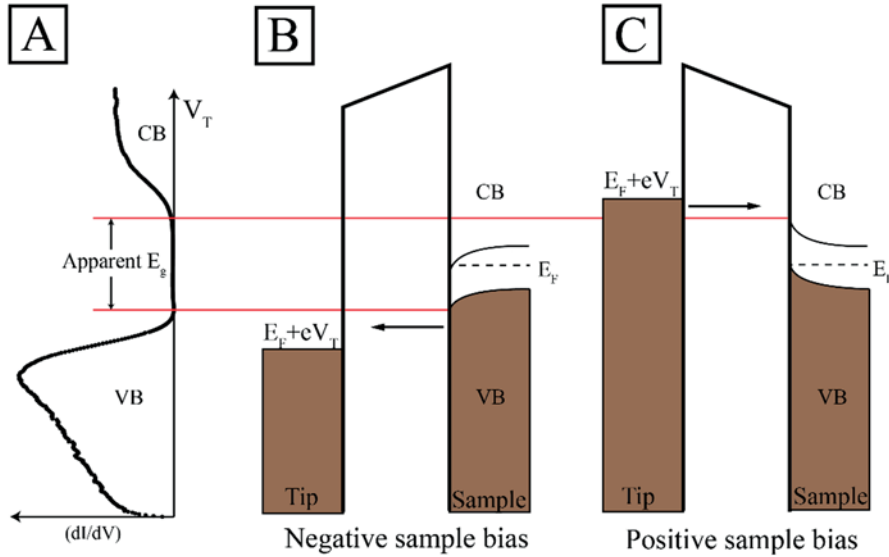


Figure 3.5. TIBB can give rise to an enlarged band gap when measured with STS. (A) (dI/dV) - V spectrum with valence- and conduction bands as well as apparent band gap marked as VB, CB, and E_g , respectively. (B) And (C) show the effects of TIBB for negative and positive biases, respectively. The apparent CB and VB edges of the STS spectrum are determined by the upward and downward TIBB, respectively.

sample instead of, as optimally, in the tunneling barrier. This effect, known as TIBB, will, as the name implies, cause the semiconductor bands to bend at the surface, effectively changing the energy scale of the spectra relative to the bulk. This uncertainty in the energy scale will mask the fundamental energy of features within the spectrum. The main physical parameters determining TIBB are the relative Fermi level-, separation-, and applied voltage-, between tip and sample. Important are also the tip work function (Φ_t), sample carrier concentration and electron affinity (χ_s) [71]. The tip work function is mainly determined by the material used and the shape of the tip apex. The dependence on the tip apex is problematic as even if the same tip is used for a number of measurements, the physical arrangement of the tip apex may be altered such that the work function, and thereby the degree of band bending, will change. As a result, unless a thorough characterization of the tip properties has been performed, only spectra obtained with the same tip and without any tip changes in between them should be directly compared.

The direction of the band bending (towards lower or higher energies) depends on the polarity of the tip-sample bias. The TIBB will change from downwards band bending at negative voltages towards an upwards band being for positive voltages, resulting in an increase in the observed bandgap. This effect is illustrated in Figure 3.5 for a low-doped semiconductor and metallic tip. The effects of TIBB for diffe-

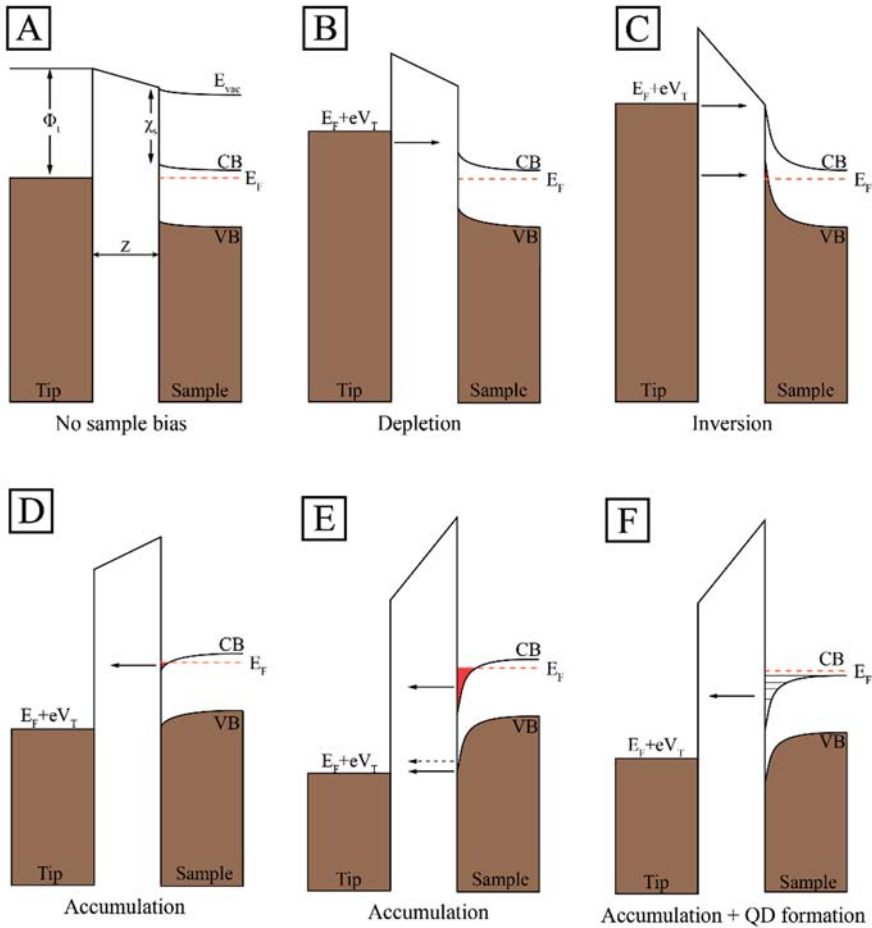


Figure 3.6. TIBB at different sample bias (V_T) settings for an n-type semiconductor and a tip-sample separation of z . (A) No sample bias is applied. The TIBB is determined by the tip work function (Φ_i), charge carrier concentration of the sample, and the sample electron affinity (χ_s). (B) Under positive sample biases, the bands bend upwards in the surface region of the sample. Electron tunneling is marked by the black arrow. A depletion of charge carriers occurs in the conduction band (CB). (C) For large positive sample biases, inversion occurs, and electrons can tunnel from the tip to the valence band (VB) states that are located above the Fermi level (E_F) as a result of the TIBB. (D) For negative sample biases, the bands bend downwards resulting in an accumulation of charge at the surface CB (red area). (E) Under large negative sample biases, electrons can also tunnel directly from the VB to the tip. Also, electrons have a probability of tunneling through the narrow gap region in the VB (marked by dashed arrow). (F) In some cases, quantum confined states can form in the CB, referred to as tip-induced QDs. The sample vacuum level is marked as E_{vac} .

rent bias settings is illustrated in Figure 3.6. For a positive bias, electrons can tunnel from the tip to the empty conduction band states of the sample. In this scenario, an upward band bending will occur. This scenario is referred to as depletion, as the Fermi level is moved further away from the sample conduction band, reducing (depleting) the number of charge carriers in the near surface region. If a large positive voltage is applied, inversion takes place, where the band bending is large enough such that the valence band states are located above the Fermi level at the surface. In this case, tunneling can occur both to the conduction band and valence band of the sample. A negative voltage will lead to an accumulation of charges at the surface, as the bands bend downwards such that the surface conduction band states are located below the Fermi level and become occupied. For large negative biases, electrons are allowed to tunnel to the empty states of the tip from the accumulation states as well as the valence band. Also, if the TIBB is shallow enough (*i.e.*, don't extend deep into the surface), electrons will have a probability to tunnel through the gap, as shown by the dashed arrow in Figure 3.6E. In some cases, TIBB can give rise to tip-induced QDs, where the band bending induce confined states [72, 73].

To obtain the proper absolute energies for features within a spectrum, such as band edge onsets, the TIBB has to be accounted for. The TIBB can be modeled for a hyperbolically shaped probe-tip in the vicinity of a semiconductor using a 3D Poisson solver [52, 62, 74]. The most basic input parameters for such modeling are tip-sample separation, tip radius, tip-sample work function difference, sample carrier concentration, and carrier effective masses. Effects from extrinsic surface states can also be accounted for by providing their position and distribution (in energy) as well as their density and charge neutrality level.

As mentioned, TIBB modeling requires information regarding the tip characteristics, such as its shape and work function. Unless a thorough characterization of the tip has been performed, such properties are unknown. Unfortunately, the results of the TIBB modeling are sensitive to changes in the tip work function and a lack of such information will make the fitting-procedure difficult [72, 75-77]. The tip characteristics can, however, be obtained by using a reference sample, where the sample properties, and thereby the amount of TIBB, are known. In this fashion, the TIBB modeling software can be used to obtain the tip characteristics. For the majority of my work, I have used the SEMITIP software, developed by R. M. Feenstra [74].

By using a reference sample, it was possible to determine the bandgaps of GaAs and InAs in the Wz phase. During STS acquisition adjacent Zb and Wz segments were systematically probed, taking great care that the physical properties of the STM tip remained constant during and in between the measurements. Avoiding tip changes ensured that the STS data obtained on the Zb part could be fitted to its well-established bandgap value as known from bulk measurements—to deduce the tip parameters—and apply the same tip parameters to correct for the TIBB of the Wz

facet. For bandgap determination on NWs, it is also essential to use sufficiently large NW diameters to avoid radial quantization effects which also leads to an enlarged observed bandgap [78, 79]. For this reason, we only used NWs with diameters larger than 80 nm when trying to determine bandgaps, which should be significantly larger than the de Broglie wavelength of any charge carriers within the NW.

For semiconductors with metal-like surfaces, where the surface DOS is significant due to surface states, the TIBB will be minimal as the states are effective in screening the charge induced by the presence of the STM tip. Such states can, however, give rise to Fermi level pinning (and local band bending). For this reason, Fermi level pinned surfaces often show experimental bandgap values which are very close to the tabulated values. This effect was observed for InAs NWs investigated at 5 K (Paper VI) where n-type defects dominated the surface conductivity.

3.4 Effects of low temperature

Room temperature STM/S experiments are limited by thermal drift and reduced energy resolution. Thermal drift is a phenomenon where the sample and tip continuously move with respect to each other due to thermal expansion effects, resulting in a smeared out and distorted image. As a result, the temperature will limit the amount of time one can spend to obtain a single image. Thermal drift is also a problem for ongoing experiments, where the same area should be imaged over extended time periods (hours–days). If the setup is left for only an hour, the tip can drift away far enough that it is challenging to find the area of interest again. Long-term imaging of an area of interest is especially problematic for STM investigations on NWs where the drift will cause the tip to “fall” off the NW and possibly damaging the tip.

In contrast, at 5 K a single spot can be imaged for several hours with minimal drift; imaging can even be performed overnight without significant drift as long as the piezo elements have been stabilized beforehand (*i.e.*, no significant piezo movements for a few hours).

The energy resolution of STM images and especially of STS spectra is limited by the thermal broadening of all electronic states, which at room temperature corresponds to a broadening of $k_b T_{(300K)} = 26$ meV. At lower temperatures, this effect is significantly reduced, $k_b T_{(5K)} = 0.43$ meV, making individual states easier to resolve. For this reason, many exciting phenomena require low temperatures to study, such as charge density waves [80, 81], QD states [73], as well as Kondo effects and magnetism [82, 83]. In some cases, such as for superconductors, the improved resolution is not the determining factor, but rather that the phenomena (currently) only exists at low temperatures [57, 84].

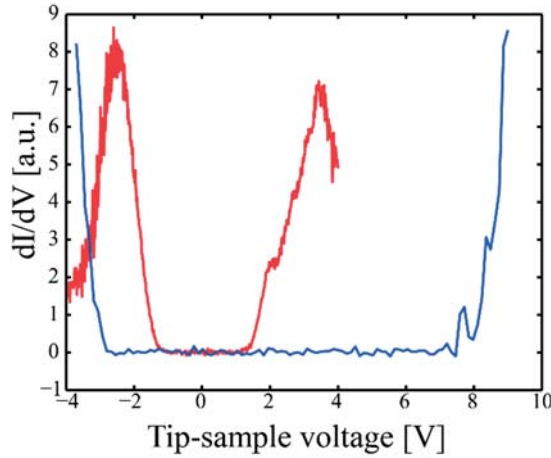


Figure 3.7. Illustrating example on how low temperature affects the conductivity of moderately doped semiconductors. STS on GaAs NW surface obtained at 5 K with a moderately doped (blue) substrate as well as a high doped substrate (red). A bandgap of approximately 11 eV and 2 eV is found for the moderate and high doped substrate, respectively. This is to be compared to the tabulated value of 1.5 eV. $U_{\text{set}} = -4$ V for both spectra.

The benefits of low-temperature STM/S do however come at a price when imaging semiconductor surfaces. Semiconductors at low temperature can have issues with conductivity due to dopant freeze-out. Mainly if the position of the doping levels, relative to the valence- or conduction band edges is larger than $k_b T_{\text{temp}}$. A reduced number of charge carriers at the surface will, in turn, lead to massive TIBB for a non-pinned surface. This effect was observed when imaging nominally undoped (*i.e.*, low degrees of p-doping due to C-impurities) GaAs NWs. As shown in Figure 3.7, an 11 eV bandgap was experimentally obtained, significantly larger than the tabulated bandgap of *ca.* 1.5 eV. The significant TIBB made the empty states of the conduction band inaccessible as substantial tip-sample biases (in the context of STM) in the range of 8–10 V had to be used; applying such large biases will, in most cases, continuously result in severe tip changes. Consequently, the area of interest of the sample will become contaminated by tip residues. In some cases, carrier inversion does not even take place, resulting in an “infinite” observed bandgap [85].

The scan range of the STM is also affected by the temperature, becoming smaller as the temperature decreases; the range of motion is commonly reduced by a factor of 10 when going from room temperature to 5 K, resulting in scan-ranges of *ca.* 400×400 to 2000×2000 nm² for the systems that I have operated. The reduced range of motion is a result of the altered voltage response of the piezoelectric elements

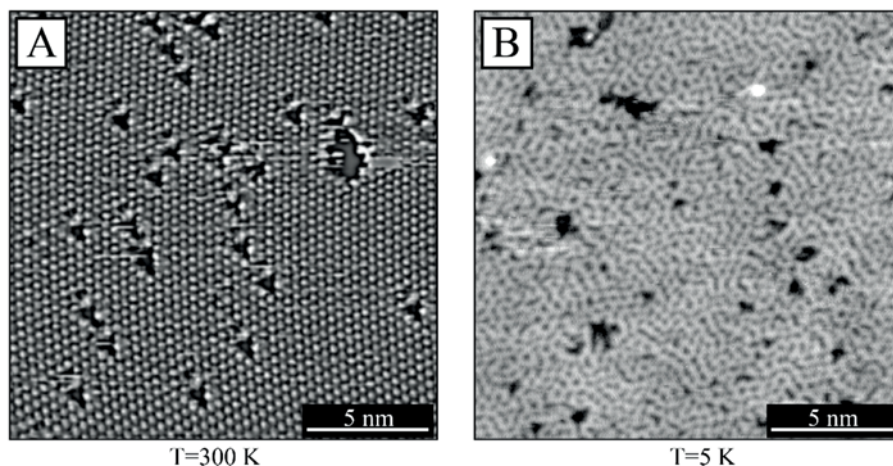


Figure 3.8. The atomic pattern on the InAs (111)B surface is obscured by a 2D electron gas at temperatures around 5 K. STM image acquired at room temperature (A) and at 5 K (B) were obtained at $V_T = -1.0$ V, $I_{\text{set}} = 50$ pA.

that control the tip movement. In typical cases a reduced scan range is not an issue, but when imaging NWs it poses a significant challenge as the scan range is used for traversing from the substrate surface to the top facet of the NWs. For NWs with a broadened apparent diameter, due to a blunt tip, the limited scan range may not be large enough to allow the tip to be moved from the substrate to the top facet of the NW. Consequently, a reduced scan range can limit the STM user to rely purely on course movement for finding NWs (*i.e.*, landing perfectly on top of the NW), a prospect that requires a great deal of luck and patience. Additionally, the ability to traverse along the NW facets—to reach an area of interest, such as a crystal phase interface—is severely limited at low temperatures where the scan range is reduced.

Low temperatures can also give rise to other effects such as surface states. As shown in Figure 3.8, the atomic pattern on the InAs (111)B surface is obscured by a 2D electron gas at temperatures around 5 K. These types of effects can be problematic as the substrate surface is often used as a means for determining the tip quality before deciding to find a NW to image.

4 X-RAY PHOTOELECTRON SPECTROSCOPY

This chapter contains a brief introduction to the theoretical and practical concepts of XPS measurements and data interpretation. Although XPS is only explicitly mentioned in one of the publications included in this dissertation, the method has been used continuously throughout my work. In particular, it was used to investigate means of removing the native oxide of III–V materials, a crucial component of atomically resolved STM investigations of NW surfaces. Also, I have participated in several experiments that have resulted in publications that were left out of this dissertation as they did not fit the intended scope. Examples are band-bending effects at the GaAs/InAs interface of core–shell NWs [86] and the use of ambient-pressure XPS for the investigation the dynamics of the layer-by-layer growth of high-k oxides [87].

XPS allows for quantitative characterization of the elemental composition of conductive and semiconductive surfaces. In XPS, the sample is continuously irradiated by a monochromatic beam of x-ray (or UV) photons, resulting in the emission of photoelectrons as long as the photon energy is sufficiently large. The number of emitted electrons, and their kinetic energy, E_k , is measured by an electron energy analyzer. The kinetic energy of the photoelectron is related to the photon energy, $h\nu$, sample work function, Φ , and the binding energy of the electronic state from which it originated, E_b via the following equation:

$$E_b = h\nu - E_k - \Phi. \quad (4.1)$$

The binding energy of the electron is conventionally used as the energy scale in XPS. The reference for the energy scale is commonly set to be the Fermi level, E_F , of the sample, which is the same for the electron energy analyzer as long as they are connected to the same ground. The above equation hold as long as the photoelectron is elastically scattered, *i.e.*, without energy loss until it reaches the detector. For this reason, the electron analyzer is set up such that only elastically scattered electrons will reach the detector. To ensure a large signal to noise ratio, XPS tends to be operated in UHV to avoid inelastic scattering when the electrons have left the sample. A recently developed method, referred to as ambient pressure XPS, do however circumvent this issue by using a gas pressure cell and differential pumping within the electron energy analyzer to operate at pressures in the mbar-range close to the sample surface [88].

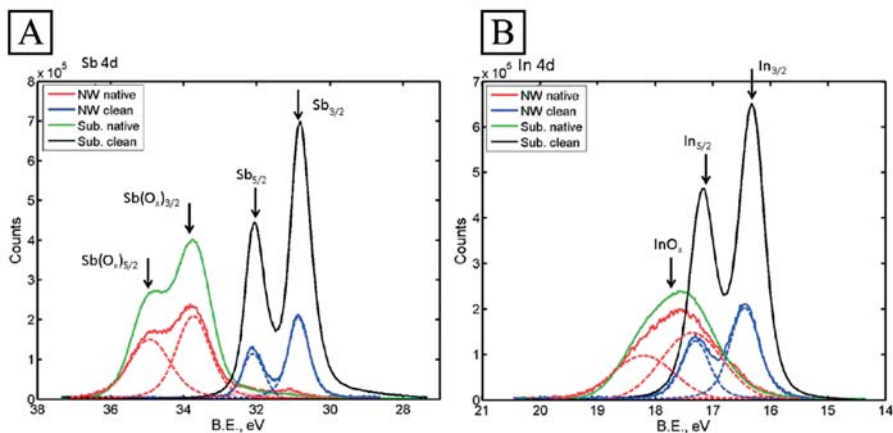


Figure 4.1. XPS spectra of InSb NWs and substrates before and after removal of native oxides, referred to as native and clean, respectively. (A) and (B) show the Sb 4d and In4d peaks, respectively. In both cases, a spin-orbit split can be seen for the pure component as well as the chemically shifted oxide-component. After oxide removal, no chemically shifted component can be seen, suggesting that the native oxides bonded to both In and Sb have been successfully removed. Image adapted from Paper VII, [89].

For large binding energies the atomic core levels are found, and consequently, the valence states are found at lower energies. The core electron levels are unique to each element (and to a large extent for each molecule and isotope) and are typically well documented. Also, the core electrons will undergo slight changes in energy due to the local changes in the surroundings, called chemical shifts. These shifts ensure a chemical sensitivity in the measurements. In fact, if the cross-section and intensity of each element-specific core level are taken into consideration, the relative (and if a reference sample is available, absolute) amounts of each atomic and molecular species can be determined.

The method is considered surface sensitive, even though the photons themselves will penetrate deep into the sample. The surface sensitivity originates from the low mean free path of the emitted photoelectrons. The mean free path, in this case, refers to the average distance the electron can travel without experiencing inelastic scattering (*i.e.*, losing energy). The energy dependence of the mean free path of the electrons can be used favorably to probe different depths of the sample. When using 50–1000 eV photons the penetration-depth is low, ranging from a few Å to a nm when going from lower to higher energies.

XPS is preferably performed at a synchrotron radiation facility where monochromatic light beams, with tunable energies, and extremely high brilliances can be achieved. Such a setup will greatly reduce noise levels and acquisition time relative to x-ray laboratory sources. I have had the privilege to perform experiments

at the MAX IV laboratory (known simply as MAXlab at the time of the experiments), where the effects of surface oxides on III–V NWs were studied. The beamline that I used, called I311, was capable of using photon energies between 43–1500 eV and had a $0.5 \times 0.1 \text{ mm}^2$ (horizontal \times vertical) spot size [90].

The work presented in paper **VII** focused on expanding the hydrogen cleaning method to be used to remove oxides from InSb surfaces. In the study, the As3d, In4d, Sb3d, and Sb4d core-levels were used to investigate the effects of atomic hydrogen cleaning on InAs/InSb NWs. The data were fitted using a combination of Lorentzian and Gaussian peak shapes, referred to as Doniach-Sunjic profiles [91]. For the subtracting of the background, necessary for fitting the data, a linear slope can be assumed in most cases.

By matching the chemical shifts found in the spectra to specific molecular compounds, their contribution to the XPS-signal could be deconvoluted and quantified. In this fashion, it was possible to assign different peaks to SbO_x and InO_x species, respectively, as shown in Figure 4.1. A more straightforward interpretation of the results was facilitated by using the same probe-depth for measurements of different elements, achieved by using the same photon energy.

5 III–V SEMICONDUCTOR NANOWIRES

All my work have revolved around the investigation of surface- and electronic properties of III–V NWs using the experimental methods that are discussed in the previous chapters. In contrast to those chapters, this section deals with the investigated NW samples and the results that were obtained while studying them. In particular, the fabrication and properties of material- and crystal phase heterostructures in III–V NWs is discussed; specifically in the context of crystal phase QDs and QWs, as well as the atomic scale properties of NW overgrowth for the formation of core–shell structures.

III–V NWs are incredibly versatile nano-scale systems with applications within high-performance electronics [1-6], photonics [7-10], and energy harvesting [10-14], as well as fundamental studies such as that of low dimensional physics [5, 92] and Majorana fermions [93-95]. They are elongated rod-shaped structures with semiconducting properties, consisting of materials from group III and V of the periodic table. Typical NWs have lengths and diameters in the μm - and nm-regime, respectively. Their geometry and growth mechanism allows for interesting band structure engineering by combining different materials and crystal structures [18, 96-98], axially or radially [99, 100], and with minimal effects from strain. III-V NWs can be grown in crystal structures which were previously unavailable in bulk, such as the hexagonal Wz structure as well as exotic crystal phases such as 4H [101-104]. They can be grown systematically—in predetermined patterns and densities [99, 105]—and seamlessly integrated into Si substrates [2, 15, 16]. The NWs investigated in this work were predominantly InAs and GaAs NWs with crystal phase heterostructures of the Wz and Zb crystal structures. Also, material heterostructure NWs consisting of an axial stacking of InAs and InSb were studied. The NWs were grown on III–V (111)B substrates and had typical diameters of 100 nm. Figure 5.1 shows SEM images of a typical NW array.

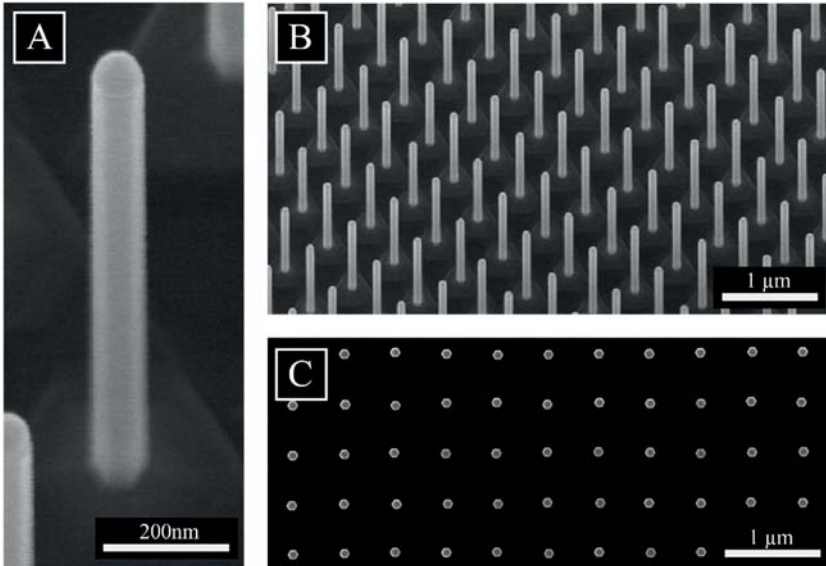


Figure 5.1. SEM images of InAs NW arrays. The NWs were grown *via* MOVPE using Au particles as catalysts. The Au particle can be seen at the top of the NW in (A). The images were obtained at 70, 70, and 90 relative to the substrate plane for (A), (B), and (C), respectively. Images courtesy of Sebastian Lehmann.

5.1 Growth

NW growth is a research field of itself, and as such I will only provide a brief review of the process in this dissertation and instead redirect the interested reader to reference [102], [106], and [107] which discuss the intricacies of traditional NW growth in depth. Notable exceptions to the traditional growth scheme are found in references [108], [109] and [16], which cover growth in the gas phase, on amorphous substrates, and III–V NW growth on Si substrates, respectively. For the NWs studied in this work, the same underlying growth mechanism was driving the growth, irrespective of the growth method, referred to as the vapor-liquid-solid (VLS) mechanism [110]. The growth process is briefly summarized in Figure 5.2.

Traditionally, III–V NWs are grown epitaxially on crystalline substrates using metallic particles as catalysts, often referred to as the seed particle. The seed particle, typically made out of gold (Au), is either deposited using size-selecting aerosol-techniques [111] or self-catalyzed using masks on the substrate [105, 112], typically made from SiO_x . The substrate is commonly a (111)B III–V wafer of the intended NW material, as NWs have been found to grow in the $\langle -1-1-1 \rangle$ -type directions pre-

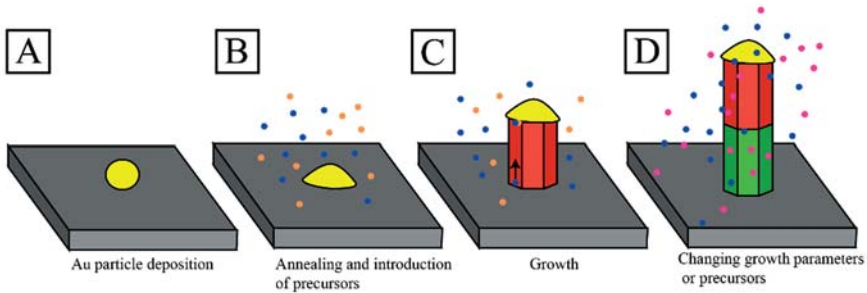


Figure 5.2. Au-particle assisted NW growth. (A) size selected Au particles are deposited onto a substrate. (B) Annealing under group V precursor flow to remove surface oxides and alloy Au-particle to the substrate. (C) Axial growth is initiated by reducing the temperature and introducing both group III and V precursors. (D) Change of precursor or introduction of dopants can be done mid-growth to create a heterostructure or homostructure, respectively.

ferentially. The substrate, prepared with either seed-particles or a mask, is introduced into a metal-organic vapor phase epitaxy (MOVPE) growth reactor (a molecular beam epitaxy process can also be used but will not be covered here as no such NWs were used in the work behind this dissertation). The constituent atomic species of the NW is introduced into the growth reactor at elevated temperatures *via* gas phase organometallics (*e.g.*, trimethylindium) and hydrides (*e.g.*, arsine), often referred to as precursors. An initial high temperature anneal under group V precursor flow is performed to remove oxide-residues and contaminants on the substrate as well as melting the Au-particle and alloying it with the substrate. Growth is initiated by reducing the temperature, typically in the range of 400–600°C, such that growth occurs predominantly under the catalytic Au-particle.

The growth preferentially nucleates at the VLS interface, *i.e.*, at the points where the vapor phase precursors, liquid catalyst particle, and solid NW stem intersect. From these nuclei, a layer by layer growth is initiated almost exclusively under the seed particle such that it is continuously pushed upwards by the most recently formed monolayer [113, 114]. The final product is a freestanding NW, with the catalyst particle located at the very top. The final diameter and length are determined by the size of the seed-particle and growth time, respectively.

The crystal structure of the NW can be controlled by varying the III–V precursor ratio [115, 116]. Although the majority of III–V materials only naturally occur in the cubic Zb crystal structure, NWs are often found to have a mixed crystal structure consisting of both Zb and the hexagonal Wz-structure [103]. Viewed along the NW growth direction ($[-1-1-1]$ and $[000-1]$ for Zb and Wz, respectively) the stacking sequence of the bilayers is different such that Zb adopts a \dots ABCABC \dots type sta-

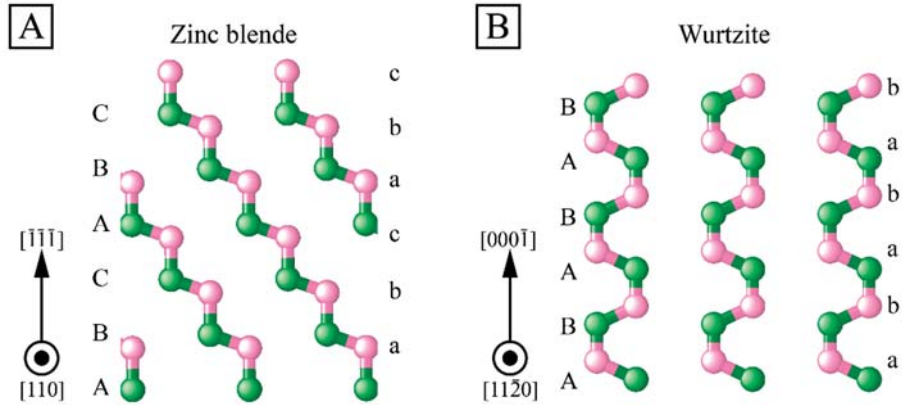


Figure 5.3. Atomic model of Zb (A) and Wz (B) crystal structures as viewed from the $\{110\}/\{11-20\}$ -type planes. Green and pink balls correspond to group V and III atoms, respectively. The stacking order is given for both group V and III atoms by capital and lower case letters, respectively.

cking and Wz aABABAB.... type, as illustrated in Figure 5.3. Although the resulting structures only differ in their third nearest neighbor, their electronic structures are different such that novel devices for electronics and photonics can be created by varying the crystal structure along a NW in a controlled fashion. Control over the crystal phase along the NW has recently progressed towards single atomic layer precision [19, 116-119].

Similarly, local variations in the NW electronic properties can also be achieved by forming material heterostructures or changing the dopant concentration or type along the growth axis. Such gradients can be achieved either by partial- or full substitution of precursors during growth or by adding entirely new ones [21, 120-122]. MOVPE-grown NWs often suffer from unintentional doping in the form of carbon-impurities which can result in different doping depending on the material; carbon induces n-doping in InAs and p-doping in GaAs [123, 124].

5.1.1 Facets and shell-growth

III-V NWs which are grown in the $[-1-1-1]/[000-1]$ direction are predominantly found to have a hexagonal cross-section, where the side-wall facets are terminated by low-index planes. The most common low-index facets on III-V NWs are, in accordance to their Miller indices [125], $\{110\}$ - and $\{112\}$ -type for Zb and $\{11-20\}$ - and $\{10-10\}$ -type for Wz, respectively [126]. In contrast to the non-polar $\{110\}$ -, $\{11-20\}$ -, and $\{10-10\}$ -type facets, the $\{112\}$ -type facets are terminated by either atoms of group III or V deepening on the orientation of the plane, referred to as A- or B-type, respectively.

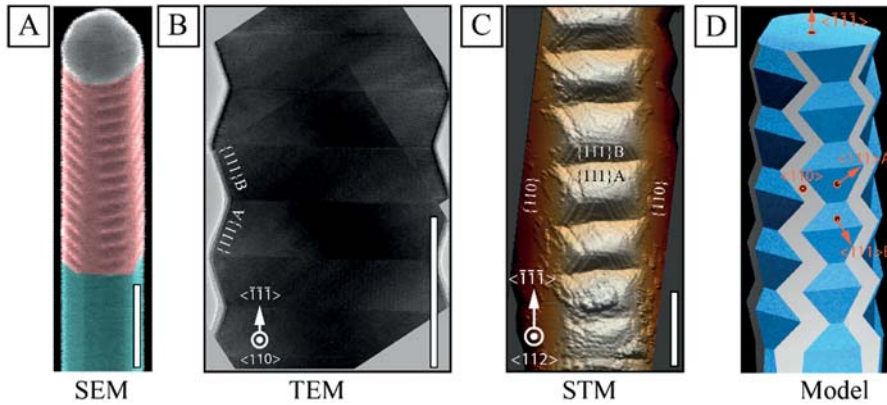


Figure 5.4. A TSL in an InAs NW imaged with SEM (A), TEM (B), and STM (C). (D) depicts a model of a TSL-structure. The TSL consists of alternating $\{111\}$ A- and $\{111\}$ B-type facets, both having a 19.5° angle relative the $\{112\}$ -type planes. As a result of epitaxial overgrowth, $\{110\}$ -type planes (grey in the model) adjacent to the $\{111\}$ -planes are often found in TSL structures. The $\{110\}$ -type planes are rotated 30° with respect to the $\{112\}$ -type planes. Images (A) and (B) courtesy of Sebastian Lehmann.

Periodic twin-defects are a type of stacking faults occurring in the Zb crystal structure where the crystal is rotated 60° around the growth axis, forming a single bilayer of Wz. In NWs with periodic twin defects the $\langle 112 \rangle$ -oriented sidewalls are terminated by polar $\{111\}$ A- and $\{111\}$ B-type nano-facets, as their surface energy is lower. These nano-facets have a 19.5° angle with respect to the $[-1-1-1]/[000-1]$ growth direction; the $\{111\}$ A- and $\{111\}$ B-type facets are inclined upwards and downwards, respectively, resulting in a saw-tooth-like shape with periodic V-groves [127, 128]. If periodic twin-defects are intentionally incorporated into a NW such a structure is often referred to as a twinning superlattice (TSL) or twin-plane superlattice (TPS). An STM, SEM, and TEM image, as well as a model of a TSL is shown in Figure 5.4.

The geometric relationships between the various low-index facets are illustrated in the STM image and model of Figure 5.5. The $\{110\}$ - and $\{11-20\}$ -type planes are in plane with each other, and so are the $\{112\}$ - and $\{10-10\}$ -type planes. There is a 30° angle between the $\{110\}/\{11-20\}$ -type and $\{112\}/\{10-10\}$ -type planes. For STM investigations of the different crystal structures in NWs, I have found that the $\{110\}$ - and $\{11-20\}$ -type facets are preferable as it is easy to sequentially access them without moving the STM tip over large steps.

As seen in Figure 5.5, several facet-types can be present within a single NW due to variations in crystal structure as well as parasitical growth on the NW sidewalls, referred to as overgrowth or shell growth. In addition to the axial layer-by-layer gr-

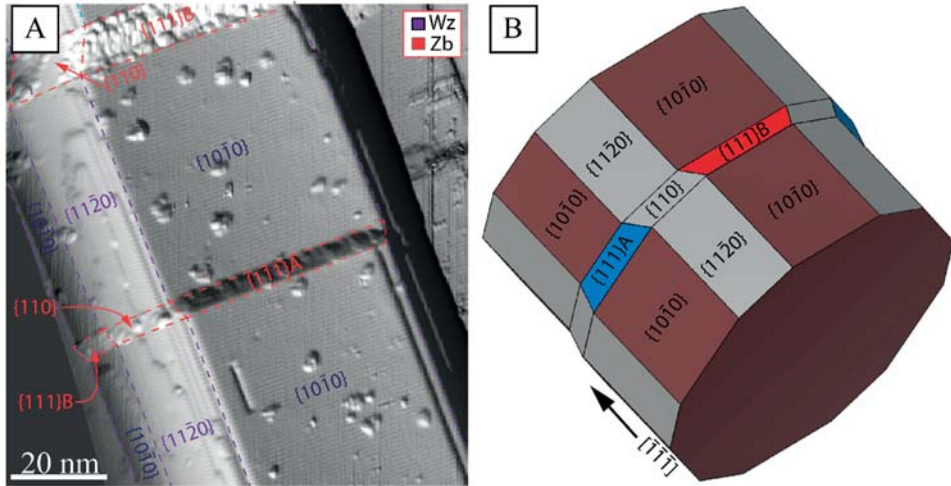


Figure 5.5. STM image (A) and model (B) illustrating the NW geometry and relative orientation of the facets. The STM image in (A) was obtained at an InAs NW, and have been differentiated for clarity. $V_T = -2.7$ V, $I_{set} = 50$ pA. Image adapted from Paper VI, [129].

rowth, occurring directly under the seed-particle, a parasitic radial (lateral) growth is also commonly observed. The radial overgrowth occurs when material from the gas phase incorporates directly into the NW sidewall facets, instead of at the VLS-interface [130]. The radial growth co-occurs on all NW side-facets as it is decoupled from the particle-induced growth, often leading to tapering along the NW growth axis. Also, the radial growth tends to promote different facet-types than the axial growth promoted by the seed-particle [131]. As a result, a deviation from the hexagonal cross-section of III-V NWs will occur towards the bottom of the NWs, where twelve facets can instead be found. The new facet-structure is a mixture of the original facets and those that result from overgrowth; for the NWs that I have studied, the $\{11\bar{2}0\}$ - and $\{110\}$ -type facets are formed as a result of radial overgrowth on Wz- and Zb-sections, respectively. The overgrowth procedure is illustrated in Figure 5.6 where STM images obtained on InAs NWs consisting of three TSL-structures, separated by Wz-sections, are shown. The STM images show the $\{110\}$ -type overgrowth-facets in different states of the radial overgrowth. As the overgrowth occurs in parallel to the axial growth, the bottom TSL segments have experienced more overgrowth relative to the upper segments.

Facet-mixing, resulting from the overgrowth, can lead to poor device performance for NWs [132]. Means of minimizing the overgrowth include simultaneous etching during growth [133, 134], or employing fast axial growth rates [135] *via* an absolute increase in III-V precursor flow rate [136]. These methods do however infer other problems, such as an increase in surface- and crystal defects.

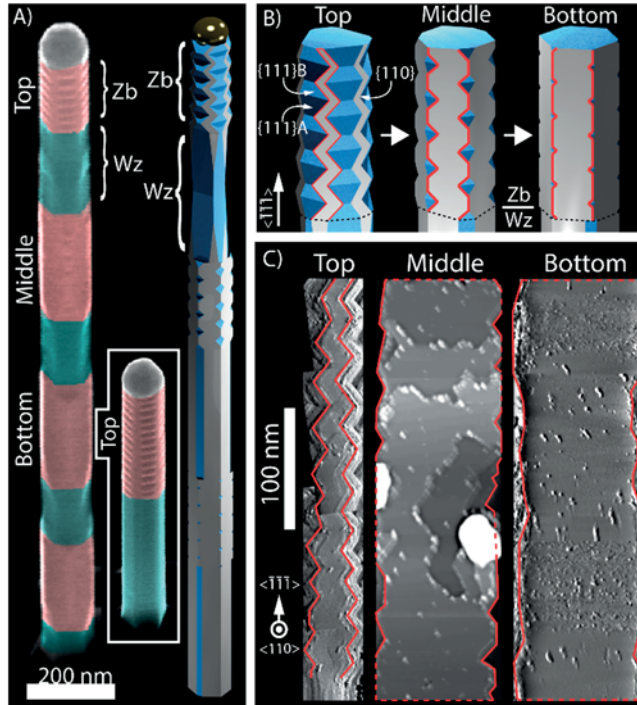


Figure 5.6. Radial growth of the NW will result in the formation of additional facets, often resulting in a 12-sided cross-sectional shape of the NW. (A) SEM image and model of InAs NW with alternating Wz and Zb segments. Radial growth was intentional to study the overgrowth-mechanism. (B) Models illustrating the evolution of the $\{110\}$ -type overgrowth-facets on the Zb segments as a function of time and position along the NW growth axis. (C) STM images of the $\{110\}$ type facets on the Zb segments formed by the radial overgrowth as a function of position along the NW growth axis, similarly to (B). Image from Paper I, [38].

When controlled, overgrowth can be used to create radial variations in material composition or doping, referred to as shell-growth [17, 18]. Using shell-growth to create so-called core-shell structures add an additional dimension for the engineering of NW devices. A benefit of the NW dimensions, relative to planar geometries, is that it allows for radial relaxation of the crystal structure. The relaxation allows for materials with a large lattice-mismatch to be combined into heterostructures without inducing dislocations due to strain. Controlled shell-growth can be used to create original NW device-designs for wrap-gated NW transistors [2, 137], light emitting diodes [138], photodetectors [139], solar cells [140], and quantum information applications [18, 141]. The growth of such multilayer structures is however complicated by a number of effects. Examples are unintentional radial doping gradients [142], uncontrolled radial growth [26], and unisotropic overgrowth [143-146]. Unisotropic growth, in the case of core-shell

NWs, refers to where the shell has grown thicker on some facet-types relative to others, often leading to poor device performance [132]. Issues related to shell-growth are originate in the fact that many properties relevant to for controlled growth of heterostructures are not known for NW surfaces. Examples are to what degree the small size of the NW facets play a role, as well as how interfaces between crystal structures and adjacent facets affect material supply and nucleation. Also, the surface energies, morphology, and growth modes of the Wz crystal structure are for the most part unknown for III–V materials.

Core–shell growth has traditionally been performed in a trial-and-error fashion, and would thus greatly benefit from detailed information about the shell-growth dynamics, and especially what role facet-types and interfaces play. Paper I of this dissertation provides information regarding nucleation sites, growth speeds, growth modes in the TSL-structures of InAs NWs. Also, the role of the different types of facets, as well as the interfaces between them, is investigated. The overgrowth-phenomena was used beneficially by imaging along an intentionally tapered NW. The axial gradient in overgrowth progression, from top to bottom, allowed for the creation of a timeline over the growth progression.

By imaging TSL-sections, with varying amounts of overgrowth, it was possible to determine that overgrowth of the TSL-structure nucleates at the concave $\{111\}$ A/B interfaces. Also, the growth on the $\{111\}$ A/B-type facets is highly anisotropic, being several times faster for the $\{111\}$ A-type facet. Similarly, it was found that for other facets, the shell growth nucleates predominantly at the Wz/Zb interfaces, but also at stacking faults/twin plains to some degree. It is common, especially in the Wz facets, to see that terraces on the NW facets start and end at stacking defects.

5.2 Crystal phase engineering

Crystal phase engineering is at the heart of III–V NW device fabrication and refers to the ability to—in a controlled fashion—change the crystal structure to shape the electronic landscape of a NW device [19, 35, 97, 102, 113, 116–118, 127, 147–154]. For instance, it has been shown that the bandgap of GaP can be changed from being indirect to a direct bandgap by the introduction of periodic coherent twin plane defects in the NW, *i.e.*, a TSL-arrangement [155]. Moreover, the V-grooves formed by such a TSL structure, consisting of $\{111\}$ A- and $\{111\}$ B-type facets, can act as a template for periodically spaced and self-assembled QDs by tuning shell growth parameters [18, 156, 157]. Additionally, surface incorporation of dopants, such as Sb, have been found to be crystal-phase selective such that highly controlled layers of delta-doping can be formed by combining crystal-structure switching and shell-growth [37]. Also, crystal phase heterostructures can be used to create periodic arrays of atomically precise QDs and QWs within a single NW by sequentially swi-

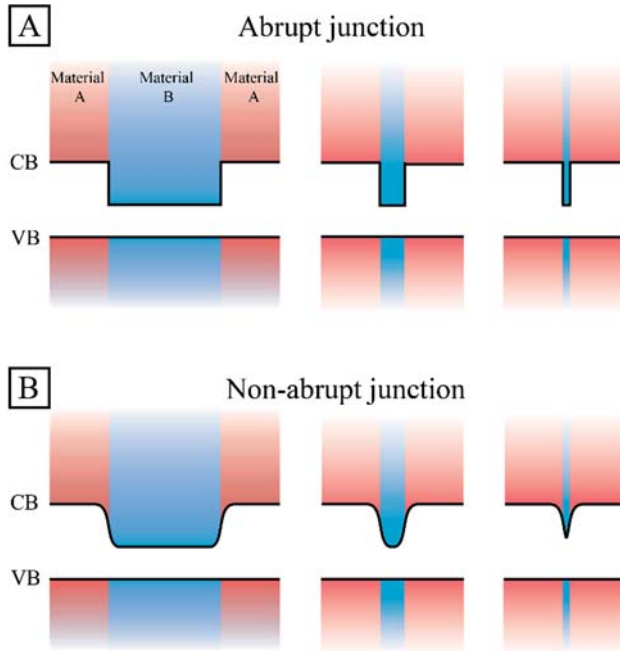


Figure 5.7. Schematics of the band response at a material heterojunction between two materials (blue and red) with different bandgaps and a flat band alignment on the VB side. (A) and (B) show QWs of different widths and with an abrupt and non-abrupt junction, respectively. For larger QWs, a non-abrupt junction will not affect the properties very much, however, as the QW is made smaller the effect of a non-abrupt junction will increase. The onset of the conduction (CB) and valence bands (VB) are marked by black lines.

tching between Wz and Zb crystal phases [97, 118]. These type of effects are all great examples of how crystal phase engineering can improve the performance of a broad spectrum of NW based applications. Examples include applications for photovoltaics [140, 158, 159], quantum computing [95, 160], and transistors [161, 162] as well as for thermoelectric- [98], and single photon devices [97, 117, 150].

Traditionally, band structure engineering is performed *via* compositional heterostructures where materials with different bandgaps are combined to shape the potential wells of, for example, QDs and QWs [21, 163-167]. However, compositional heterostructures intrinsically suffer from imperfect interfaces due to the difficulty of forming atomically sharp compositional junctions without defects or material intermixing. A non-abrupt interface will lead to an unpredicted and gradual change in electronic structure across the material boundary, resulting in a deviation from the model-like square shaped well-structure [21, 163, 165-167]. As

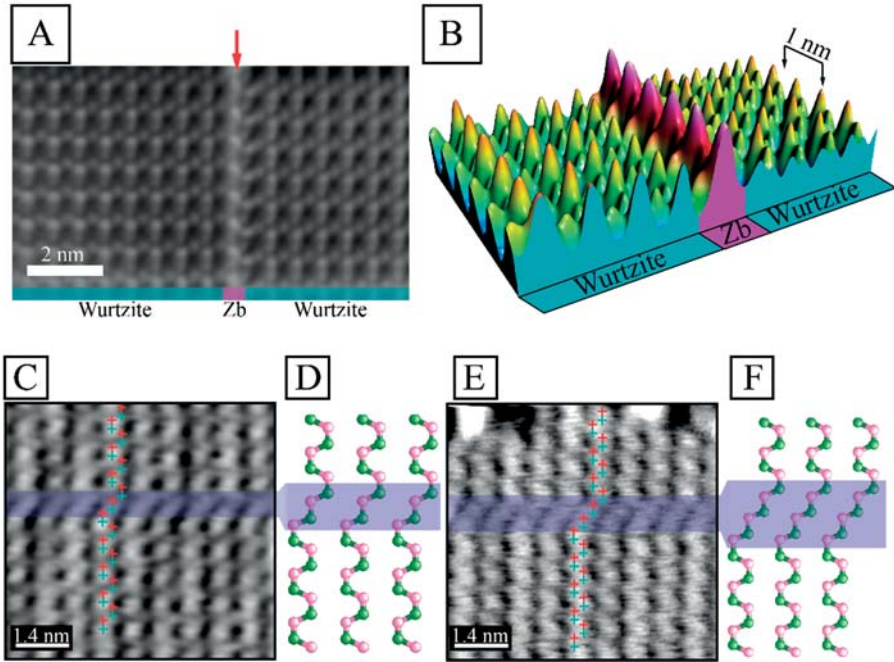


Figure 5.8. STM image of a single bilayer Zb segment in a Wz InAs NW, forming a QW as observed from an $\{110\}/\{11\bar{2}0\}$ -type surface. (A) Greyscale image, $I_{\text{set}} = 50$ pA. The tip-sample voltage of $V_T = -400$ mV corresponds to the onset of the Zb valence band, which occurs before the Wz, explaining the high contrast of the Zb segment (red arrow) in the image. (B) 3D render of a section of (A). STM images of a single- (C) and double bilayer Zb segment (E) as well as corresponding atomic models of the QWs are shown in (D) and (F), respectively. The green and red crosses in the STM images correspond to the expected positions of In- and As atoms, respectively. Image settings are $V_T = -1.7$ V and $I_{\text{set}} = 50$ pA for the single bilayer Zb segments and $V_T = -1.9$ V, $I_{\text{set}} = 150$ pA for the double bilayer segment. Figure adapted from Paper VI, [70].

illustrated in Figure 5.7, this effect is especially detrimental for smaller QWs and QDs, where the shape of the potential is heavily distorted. The shape and height of the potential well are determining factors for the physical properties of QDs and QWs [97, 118, 164, 165], and can define fundamental behavior such as metallic *versus* semiconducting [168].

These problems can, however, be solved by crystal phase engineering as the interfaces between Wz and Zb have been shown to be atomically sharp [19, 113, 115, 169]. Also, material intermixing at the interface is not a concern since both crystal phases consist of the same material composition. In Figure 5.8 I show an STM image of a crystal phase QD in an InAs NW, consisting of a small Zb segment within the Wz NW, is shown.

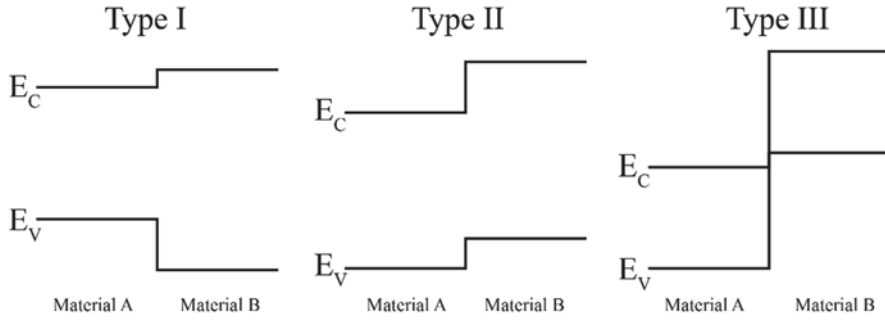


Figure 5.9. Schematics illustrating the different band alignment types that can occur at a material heterojunction. Material A and Material B could be, for instance, different crystal structures of the same material, such as Wz and Zb, or different material compounds, such as GaAs and GaSb. E_C and E_V correspond to the conduction- and valence band edges, respectively.

5.2.1 Electronic structure

Crystal phase engineering is based on the difference in bandgap between crystal structures of the same material. The electronic structure of a semiconductor is mainly determined by the atomic symmetry of the crystal, and as such, is expected to change even for small variations of the crystal ordering, such as between the Wz and Zb crystal structures, where only the third nearest neighbor is different [102]. Two relevant properties for NW devices based on crystal phase engineering are the difference in bandgap between the two crystal phases and the band alignment at the crystal interface.

Theoretical work predicts a larger bandgap for Wz relative to Zb for III–V systems [20, 155, 170–174], with the exception being GaP where the opposite behavior is expected [155]. Experimental bandgap values of the Wz phase are often extracted *via* indirect methods such as PL, or contact-electrical measurements were sample impurities, and crystal defects affect the results, leading to large discrepancies in reported bandgap values. As an example, Table 5.1 shows some theoretical and experimental values of InAs. For comparison, I have also included the values present in Paper VI, where 5 K STM/S was performed on neighboring Wz and Zb segments to directly extract their bandgaps.

The band-alignment types found for Wz and Zb are very similar to what is found in compositional heterostructures, which can be categorized as a type I, II or III depending on the alignment type, as illustrated in Figure 5.9, [20, 155, 171, 173]. The band alignment of Wz and Zb in III–V materials are predicted to be of type II

Table 5.1. Theoretical and experimental values of the bandgap in InAs in the Wz crystal phase, including values from this work obtained by 5 K-STM/S (shaded blue). The gap difference refers to the total bandgap difference between Wz and Zb in InAs. For the experimental values, a Zb bandgap of 417 meV at 5 K was assumed. The theoretical methods refer to local-density approximation calculations (LDA), modified Becke–Johnson exchange-correlation potential (mBJ), dynamically screened exchange approximation (GW), and transferable empirical pseudopotentials (EP). For some models the spin-orbit (SO) interaction is taken into account.

Theoretical:	Bandgap [meV]	Gap difference [meV]	Temperature [K]	Method
Belabbes [155]	481	70	0	LDA-1/2 QP +SO
Friedhelm[20]	481	70	0	LDA-1/2 QP +SO
De [171]	481	70	0	EP +SO
Murayama [173]	457	40	0	LDA
Zanolli [170]	611	55	0	GW
Dacal [172]	461	41	0	LDA+mBJ+SO
Experimental:				
This work	504	87	5	STM/STS
Kobl Müller [175]	500	83	20	PL
Rota [176]	477	60	11	PL
Bao [177]	520	103	7	PL
Möller [178]	458*	41*	5	PL
Trädgårdh [179]	540**	123**	5	PL
Chen [148]	345***	–20 to –70	110–240	contact-electrical
*lower bound, **extrapolation from InAsP bandgap, ***do not take valence band transport into account for bandgap extraction, likely resulting in an underestimated gap size.				

with the Zb being at more negative energies, with, again, GaP being the exception [155]. Although the majority of experimental investigations agree on this point, the reported magnitude of the shift varies.

The intrinsic band alignment can be challenging to extract experimentally due to Fermi level pinning. Instead, an extrinsic, often defect induced, band alignment is present on the surface of the NWs [35]. Fermi level pinning is an effect where surface states, generally located within the bandgap, have a very high density of states such that they can absorb large amounts of charge without changing the Fermi level position, *i.e.*, the Fermi level is pinned to the energy of the surface state. As a result, the band alignment of crystal segments can depend on the surface morphology of the NW, as atomic defects and steps will give rise to extrinsic surface states which can pin the Fermi level [180-183]. The increased surface-to-volume ratio of NWs with smaller diameters make them especially susceptible to Fermi level pinning-effects.

In Paper **IV**, **V** and **VI**, STM/S is used to directly determine the bandgap and band alignment of Wz and Zb in InAs and GaAs NWs. By performing STS onto adjacent Zb and Wz segments, it was possible to probe and compare the band structure around the Fermi levels for the two crystal phases. In STS, Fermi level pinning is found to reduce the effect of TIBB significantly, such that the amount of TIBB can indicate if a surface is pinned or not. As presented in paper **VI** and **V** a flat-band alignment was found between Wz and Zb in InAs, in contrast to the predicted type II. The flat-band alignment is explained by Fermi level pinning due to n-type defects in the NW. In contrast, for GaAs NWs of similar diameter, the surfaces were found to be unpinned such that the intrinsic band alignment could be measured, confirming the predicted type II alignment type. For both material systems, a larger bandgap was found for Wz relative to Zb.

5.2.2 Quantum dots and wells

QDs and QWs are nano-scale systems that confine charge carriers by restricting their movement in specific dimensions. In a QD, the charge carriers are confined to 0D, *i.e.*, no free movement, whereas in a QW they are confined to move in a 2D-plane. For crystal phase heterostructures the confinement, to zero- or two dimensions, is mainly determined by the NW diameter, electron/hole effective mass, and segment length. For smaller diameters, and carrier effective masses, the confinement in all dimensions increase, resulting in a QD, and vice versa for a QW [97]. Along the confined dimensions, a limited number of allowed electronic states are present such that the charge carriers only are allowed to occupy specific quantized energy levels, analogous to the energy levels within the potential well of an atom. The depth and width of the potential well will determine the number of states as well as their energy. Atomically precise and identical QDs or QWs would

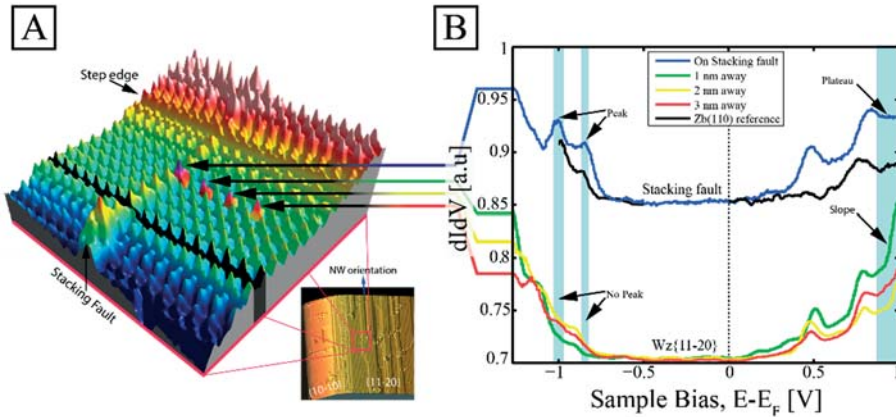


Figure 5.10. Topographic and electronic structure of single bilayer Zb segment (stacking fault) and surrounding Wz matrix. (A) A 3D render of a $12 \times 12 \text{ nm}^2$ STM image from the $\{110\}/\{11\bar{2}0\}$ -type surfaces of an InAs NW, obtained at 5K, with $V_T = -0.3 \text{ V}$, $I_{\text{set}} = 100 \text{ pA}$. The STS events shown in (B) were obtained at atoms coated in red, as shown in (A). The STS is obtained at the stacking fault (blue), as well as 1, 2, and 3 nm away (green, yellow, and red, respectively). A reference Zb spectra is shown in black, obtained at a Zb segment larger than 100 nm. Fermi level is shown as a black dotted line. Characteristic similarities can be seen in the valence and conduction band for the single bilayer Zb segment and the reference Zb segment. Also, the STS obtained on the Wz consistently show features characteristic to Wz, independent on the distance to the single bilayer Zb segment. Figure adapted from Paper VI, [70].

be beneficial for a large number of applications, were high coherence between QDs and QWs is required, such as single photon emitters or quantum computers [55, 150, 160, 184-186].

As discussed previously, QDs and QWs are commonly formed by artificially creating potential wells *via* compositional or crystal phase heterostructures. For atomic scale QD- and QW-applications crystal phase heterostructures would be preferable as the interface is atomically sharp [113]. Very little is however known about the atomic scale band-alignment at the Wz and Zb interface. Electrical measurements of polytype NWs have shown that atomic scale crystal-defects result in poor device performance due to trapped charges or reduced charge mobility [23, 151, 187]. These effects indirectly confirm that a potential well is formed, but reveal little about its depth and shape. Direct determination of the atomic scale band-alignment *via* conventional experimental methods, such as contact-electrical and PL measurements, is limited by the extreme precision required in NW growth, sample preparation as well as spatial and electronic resolution [118]. Also, only a limited number of theoretical work exists that predict how the electronic structure changes spatially over a crystal phase boundary at the atomic-scale level. When reviewing those studies, the results are found to be inconclusive, varying from a predicted ato-

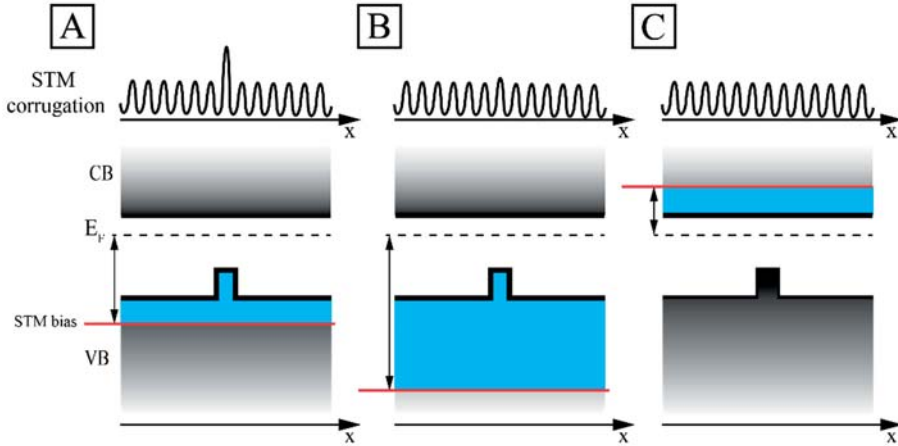


Figure 5.11. The schematic image is illustrating the relationship between atomic-scale corrugation, STM imaging bias, and the potential landscape of the surface. The image shows a band diagram of a heterostructure QW. Tunneling occurs to/from the states between the STM bias, marked by a red line, and the Fermi level, E_F , as indicated by the black arrows. The conduction band and valence band are denoted CB and VB, respectively. States that contribute to the tunneling along the spatial dimension x are marked in blue. In (A), a significantly larger amount of states are available for tunneling at the QW, leading to a large corrugation of the atom at that position. In (B), the relative amount of available states is more comparable such that almost no difference in corrugation is seen over the QW. In (C) no difference in sample DOS exist on the CB side resulting in an isotropic corrugation along x .

mically abrupt junction to non-local effects spanning over several III–V bilayers [148, 188, 189]. In conclusion, despite its technological relevance, no consensus has been reached regarding the atomic-scale electronic properties of Wz/Zb interfaces.

In Paper VI, I contribute to the field of crystal phase engineering by experimentally confirming that an atomically abrupt change in electronic structure indeed occurs at the crystal phase interface between Wz and Zb. For this purpose, 5 K-STM/S was performed on InAs NW surfaces with intentional inclusions of small Zb segments. In Figure 5.10, STS and a (3D rendered) topographic STM image are shown, obtained from a single bilayer Zb segment (a stacking fault) and the surrounding Wz matrix, obtained on the $\{110\}/\{11\bar{2}0\}$ -type facet. When comparing STS on the Zb QW with Zb segments which are larger than 100 nm (*i.e.*, no expected confinement) characteristic similarities were found, indicating that the electronic structure of a single bilayer of Zb segments mimics that of the bulk. When probing the Wz crystal just 1 nm away from the Zb bilayer, characteristics of bulk Wz is found. This indicates that the transition in electronic structure from Wz-like to Zb-like is abrupt to within at least 1 nm. STM imaging of the Zb segment and surrounding Wz matrix reveal that the transition, in fact, is atomically sharp. This

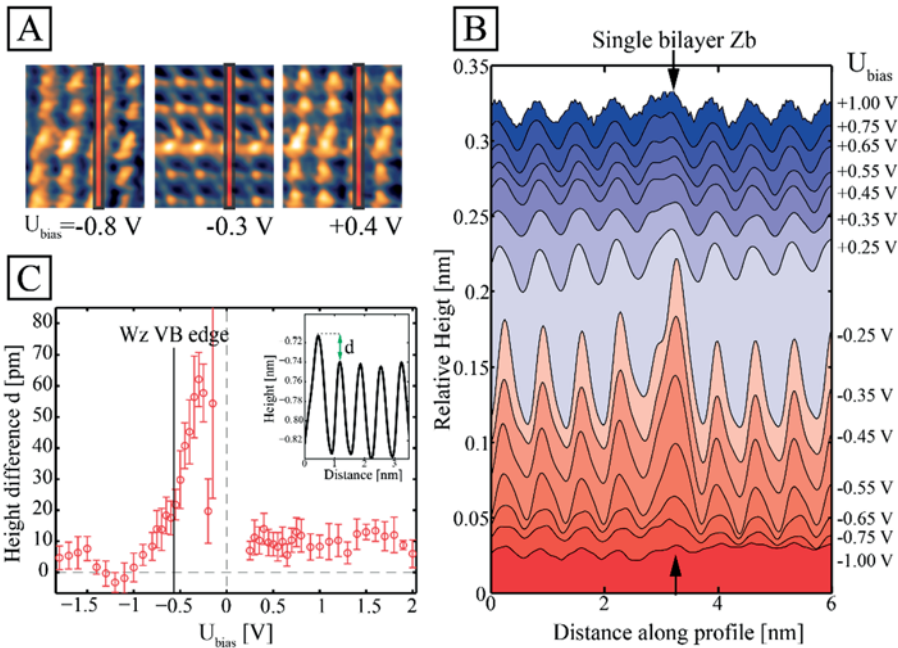


Figure 5.12. (A) STM images of single bilayer Zb segment in a Wz matrix, obtained on the $\{110\}/\{11\bar{2}0\}$ -type facets. I_{set} is 100 pA for all images. Red lines represent the position of line profiles used in (B) and (C). (B) Line profile across the stacking fault from STM images at different tip-sample voltages, V_T . (C) The difference in atomic corrugation, d , between the Zb atoms and the nearest Wz atom (as illustrated in inset) is plotted as a function of tip-sample voltage, V_T . Errorbars represent the standard deviation. Image adapted from Paper VI, [70].

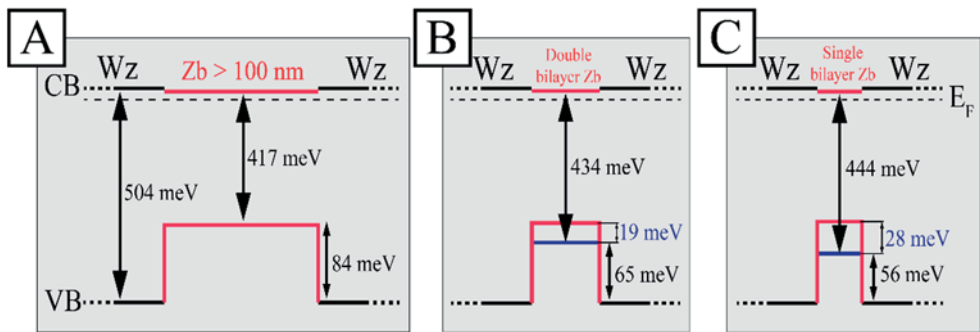


Figure 5.13. Energy diagram showing the valence- and conduction band edges of Wz (black) and Zb (red) segments in InAs as obtained with STS at 5 K. The dashed line represent the Fermi level. The increase in the observed bandgap of the double (B) and single (C) bilayer Zb segments, relative to the large Zb segment (A), is interpreted as due to confined ground state levels within the QW, marked by horizontal purple lines. Image from Paper VI, [70].

could be determined as an atomically sharp contrast between the Zb bilayer, and the surrounding Wz surface was observed when imaging at energies where few states should be present for the Wz relative to the Zb, i.e., just above the Wz band edge. The principles behind this effect are illustrated in Figure 5.11, and experimental results are shown in Figure 5.12.

A size-dependent change in the bandgap of the Zb segments with different lengths was found, suggesting the presence of confined states within the smaller segments. A bandgap of 417 meV was found for Zb segments which were larger than 100 nm (considered as bulk-like), whereas a bandgap of 444 meV and 434 meV was found for single- and double bilayer Zb segments, respectively. As illustrated in Figure 5.13, the enlarged bandgap for the smaller Zb-segments is consistent with confinement effects within the Zb segments, where the bandgap limits are defined not by the VB edge but instead by the highest ground state energy within the QW/QD-structure.

6 NANOWIRE SURFACES

As discussed in this chapter, the NW surface plays a major role in determining the overall optical and electronic properties of the NW. For this reason, I discuss the atomic and electronic structure of the various types of facets available in III–V NWs; a special emphasis is that of surface states. A brief introduction to the general morphology of the NW facets is also provided. The ability to identify specific NW facets without atomic resolution—but rather based on their larger scale morphology—have been important for navigating to an area of interest on a NW.

When a surface is formed, the symmetry of a crystal is broken, and as a result, some of the electronic bonds of the surface atoms will be unsatisfied. The spatial configuration and electronic characteristics of these bonds, commonly referred to as dangling bonds, are determining factors for the chemical properties of a surface. For example, the dangling bonds can be the origin of surface states, *i.e.*, states or bands of energies often located within the bandgap of semiconductors. In some cases, the dangling bond configuration can be chemically unstable to such a degree that morphological changes in the atomic arrangement of the surface layer(s) spontaneously occur to reduce the surface energy, referred to as a surface reconstruction. Factors that play a role in the formation of surface reconstructions are, for example, the material type, crystal plane, temperature, or atmospheric conditions. The electronic and optical properties of any given material may be vastly different depending on what type of reconstruction the surface exhibits [190-195]. Also, diffusion lengths and surface energies—parameters which are essential for modeling and growth of core–shell NW structures—are partly determined by the type of reconstruction of the surface [196, 197].

As a consequence of the nano-scale dimensions and rod-shaped geometry, NWs have an inherently large surface-to-bulk ratio. As a result, NW devices are much more sensitive to surface effects compared to larger-scale components. In fact, the electronic and optical properties of NWs are greatly influenced—and in some cases dominated by [24, 25]—the surface morphology [26-28], surface defects [29-34], and surface states of the NW side facets. This issue is further complicated since the morphology and types of defects may vary for the different crystal structures and facet types [35-38]. Characterization of surface effects, their nature, and origin, thus play a crucial role in determining, and more importantly, when trying to manipulate the NW properties.

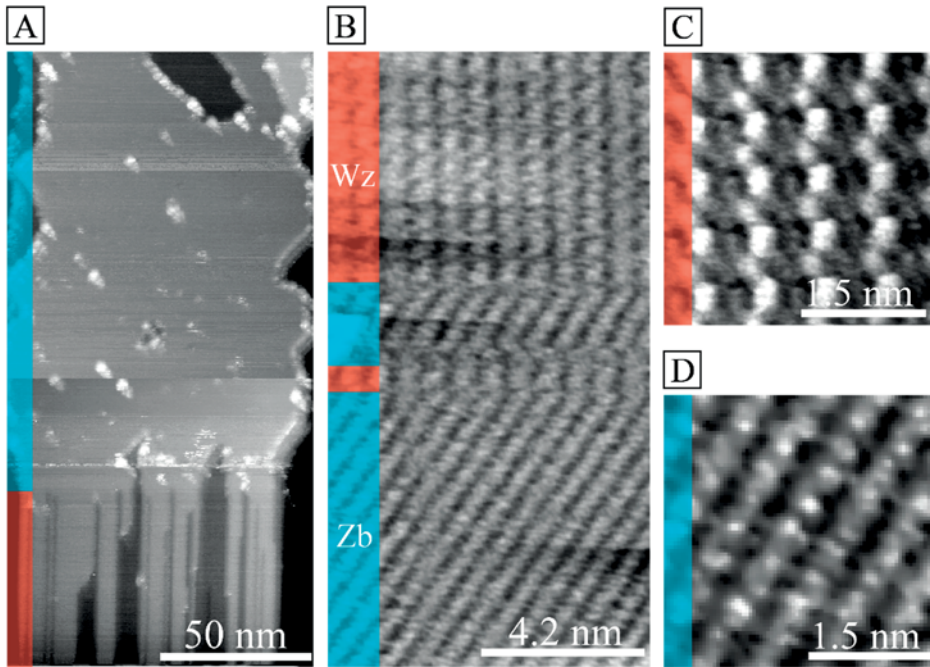


Figure 6.1. STM images of the most common low index facets of III-V NWs. (A) and (B) show a Wz/Zb interface obtained on the $\{110\}/\{11-20\}$ -type facets of InAs NWs. (C) and (D) show atomically resolved images of the $\{11-20\}$ -type and $\{110\}$ -type facets, respectively. $V_T = -1$ V, $I_{set} = 50$ pA

6.1 Surface morphology

When imaged with STM, the low index facets of the NWs were all found to be different in regards to the atomic-scale structure as well as larger-scale surface-morphology. For the $\{11-20\}$ -, $\{110\}$ -, and $\{10-10\}$ -type facets, STM images reveal atomic patterns corresponding to an unreconstructed surface [198]. In Figure 6.1 and Figure 6.2, large-scale as well as atomically resolved STM images of the most relevant low index facets, obtained on the sidewalls of InAs, are shown. On the atomic scale, the $\{110\}$ - and $\{10-10\}$ -type surfaces have atomic rows extending along the surface at a 35.4° angle or perpendicular to the $[-1-1-1]$ growth direction, respectively. A slightly more complex pattern is found for the $\{11-20\}$ -type surface, where instead zig-zag chains are found to extend along the NW growth axis. However, sometimes a square-pattern is observed instead of the zig-zag pattern. This inconsistency can be explained by a change in the electronic configuration of the atom at the tip apex, switching from an ideal s-orbital to a higher order configuration, such as a p-orbital [48].

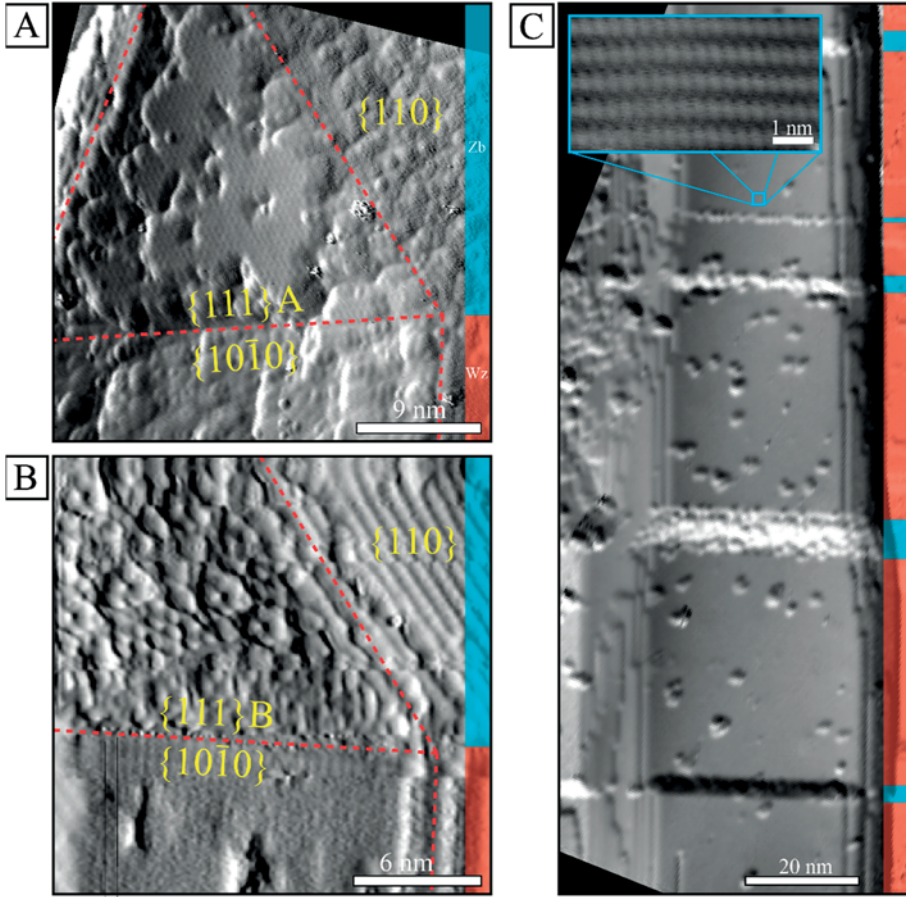


Figure 6.2. STM images of the $\{111\}$ A/B- and $\{10\bar{1}0\}$ -type surfaces obtained on GaAs NWs. The images have been differentiated for clarity. (A) and (B) shows a (2×2) and a $(\sqrt{19}\times\sqrt{19})R23.4^\circ$ reconstruction on the $\{111\}$ A- and $\{111\}$ B-type facet, respectively, $V_T = -4.5$ V, $I_{set} = 50$ pA. (C) Shows an $\{10\bar{1}0\}$ -type facet, broken up by several intentionally included Zb segments exhibiting $\{111\}$ A/B-type facets. Inset of figure (C) shows a section of the $\{10\bar{1}0\}$ surface with atomic resolution, $V_T = -2.7$ V, $I_{set} = 50$ pA. The growth direction $[-1\bar{1}\bar{1}]/[000\bar{1}]$ is upward in all images.

For InAs and GaAs NWs the $\{111\}$ A- and $\{111\}$ B-type facets were both found to be reconstructed. The $\{111\}$ A-type facet exhibits a (2×2) reconstruction, consistent with the most common reconstruction found for the surface in planar geometries within the same parameter-space [199]. The $\{111\}$ B-type facet was found to be heavily reconstructed, reminding of a semi-ordered $(\sqrt{19}\times\sqrt{19})R23.4^\circ$ reconstruction often found on GaAs $\{111\}$ B-type surfaces [200, 201]. This is quite interesting as the InAs $\{111\}$ B-type surface is expected to have a (1×1) structure within the parameter-space used for both the NW growth and post-treatment [202].

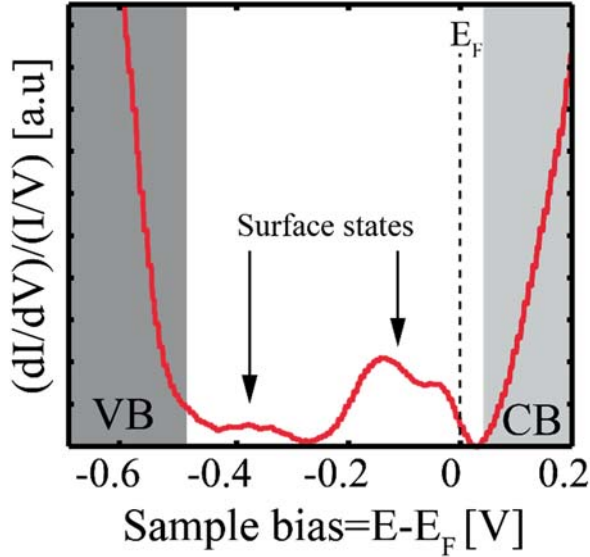


Figure 6.3. STS obtained at an $\{11\bar{2}0\}$ -type facet on an InAs NW, obtained at 5 K. States are present in the bandgap and are attributed to extrinsic surface states originating from atomic steps. VB and CB refer to the valence- and conduction bands, respectively. E_F denotes the Fermi level. Image adapted from Paper VI, [129]. $U_{\text{set}} = -1.2$ V, $I_{\text{set}} = 200$ pA.

In fact, this type of $(\sqrt{19} \times \sqrt{19})R23.4^\circ$ reconstruction has never been observed on the planar analogies of the InAs surface, implying that the surface energy may be greatly affected by a size-limited surface. This, in turn, implies that such effects must be taken into consideration when growing and designing nano-scaled objects.

In analogy to the atomic scale morphology, the large-scale topography of the NW facets is characteristic for each surface type. The $\{11\bar{2}0\}$ -type surface exhibits a high density of steps propagating along the $[-1\bar{1}\bar{1}]/[000\bar{1}]$ growth direction. The terraces formed by these steps are often very thin, sometimes being only single atoms wide, and can extend for several hundred nanometers along the NW, see Figure 6.1. This is indicative of a low and high surface mobility of adatoms along and perpendicular to the growth direction, respectively. For the $\{11\bar{2}0\}$ -type surface, terraces on top of terraces were never observed, suggesting that any epitaxial growth on this facet-type occurs in a layer-by-layer fashion. Based on a large number of STM images, we found that nucleation of new layers, *i.e.*, the extended terraces, occurs almost predominantly at three locations on the surface: at interfaces between Wz/Zb, at steps perpendicular to the growth direction, and at stacking faults. These type of nucleation sites are interesting as they demonstrate that the surface morphology is affected by crystal defects.

In contrast to the $\{11\bar{2}0\}$ -type facets, the $\{10\bar{1}0\}$ -type facets generally exhibit a very open surface morphology with a relatively low density of steps, with edges perpetuating perpendicular to the NW growth direction. This morphology suggests that the surface mobility of growth material is different for the $\{10\bar{1}0\}$ - and $\{11\bar{2}0\}$ -type facets. Interestingly, stacking faults (small Zb segments) were always found to correlate directly to an atomic step on the $\{10\bar{1}0\}$ surface, whereas no such effect was found on the $\{11\bar{2}0\}$ -type surface. This type of correlation is not surprising as the corresponding facet of the $\{10\bar{1}0\}$ -plane for Zb is the $\{11\bar{2}\}$ -type plane, which tends to form $\{111\}$ A- and $\{111\}$ B-type facets. Hence, the atomic steps induced by stacking faults are in fact atomic-scale sized $\{111\}$ A- or $\{111\}$ B-type facets, again demonstrating the relationship between crystal-structure defects and surface morphology.

6.2 Surface states

Surface states can modify the electronic structure around the Fermi level of a given material such that it deviates from the bulk structure. Surface states which are located within the fundamental bandgap can be detrimental to the performance of semiconductor devices where they can act as unwanted recombination centers for charge carriers or preventing band bending at a heterojunction *via* Fermi level pinning [24-33]. Luckily, the low index surfaces of GaAs and InAs NWs do not have any intrinsic surface states located within the bandgap [203, 204]. However, a large number of extrinsic surface states can potentially be present as a result of surface defects such as vacancies, atomic steps, adsorbates, material interfaces and even atomic steps [205-207]. Characterization of such surface states on NWs have been challenging as conventional methods such as PL and contact-electrical measurements only observe the cumulative effect of all surface states present on the NW surfaces, providing no information about the influence of each type of defect.

The ability of STM/S to map the electronic structure with atomic resolution makes it an excellent tool for probing the characteristics of surface states. For example, in Paper VI 5 K-STM/S was used to detect the presence of step induced states on the $\{110\}$ - and $\{11\bar{2}0\}$ -type surfaces of InAs NWs. The surface states were highly delocalized, extending several tens of nanometers away from the step edge, being virtually omnipresent due to the small size of the NW facets and relatively large density of steps. In Figure 6.3 an STS spectrum from the $\{11\bar{2}0\}$ -type surface is presented, obtained far away from any defects or step edges, and nonetheless, a non-zero LDOS is seen within the bandgap at energies between 0 to -0.45 V, signifying the presence of surface states at those energies.

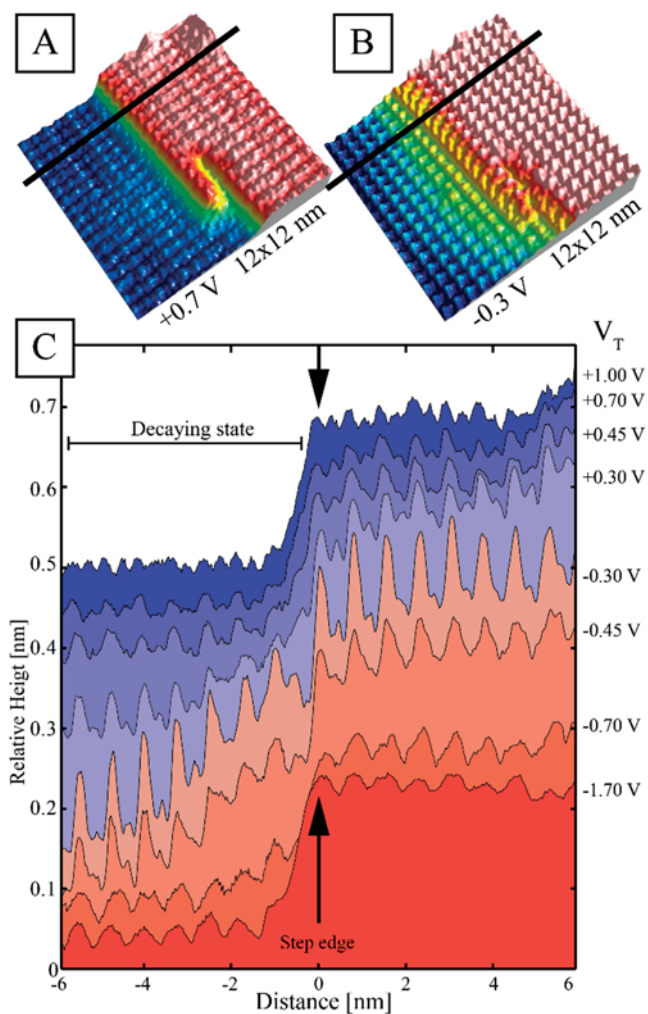


Figure 6.4. STM images obtained at the same position but at different energies at the $\{11\bar{2}0\}$ -type facets of InAs NWs reveal the presence of surface states originating from step edges. (A) and (B) shown 3D renders of STM images obtained at $V_T = +0.7$ V and $V_T = -0.3$ V, respectively. (C) Shows a number of line profiles (obtained as marked by a black line in (A) and (B)) extracted from STM images obtained at varying tip-sample voltages V_T . $I_{\text{set}} = 200$ pA for all images and line profiles. Profiles are shifted along the y-axis for clarity. An increase in LDOS can be seen below the step edge for energies between -0.45 V and -0.3 V. Image from Paper VI, [129].

Performing STM imaging with imaging-biases corresponding to the energies of the gap-states revealed that the states most likely originated from the terrace step edges of the $\{11\bar{2}0\}$ -type surfaces, which were extending along the NW growth direction. In Figure 6.4, 3D renders of STM images obtained on a $\{11\bar{2}0\}$ -type surface are shown. The surface exhibits two terraces which are separated by an atomic step. The images are obtained at the same spatial location but at different energies. The difference in step morphology is consistent with the presence of a decaying surface state below the step edge at -0.3 V. The presence of a higher LDOS below the step edge is confirmed by a number of line scans, shown in Figure 6.4, where the states are found to be confined to energies between $+0.3$ to -0.45 V with respect to the Fermi level, similarly to what is seen in the STS, see Figure 6.3.

7 SURFACE PREPARATION AND MODIFICATION

This chapter primarily deals with means for preparing the NWs for STM investigations. Specifically, the chapter elaborates on methods for NW transfer from the growth substrate to another suitable substrate—going from standing upright to laying down—allowing for easy access to their side facets by the STM tip. A discussion regarding suitable substrates and how to remove the native oxides is also provided. Finally, the chapter contains a section on surface-modification for the purpose of altering the NW properties. Specifically, incorporation of Bi on GaAs NWs is discussed in terms of the experimental procedure and implications of the results.

STM investigations of NW surfaces poses some restrictions on sample preparation. Two main challenges come to mind: firstly, the NWs are grown standing upright, and due to the geometric configuration of our STM setup it is very challenging to approach a NW side-facet with the STM tip in such a configuration. Any realistic experiment hence requires that the NWs be transferred from the growth substrate to an additional substrate, on which they are oriented in parallel to that substrate surface. Secondly, when transporting the NWs from the growth chamber to the vacuum chamber of the STM, native oxides are formed on the NW surfaces. These oxides will affect any spectroscopic measurements as well as making direct surface imaging impossible, and must, therefore, be removed before STM investigation.

The large number of facets available within one single Wz/Zb heterostructure NW also provides an excellent playground for material-deposition experiments. For such heterostructure NWs, the effects of material deposition can be studied for several facets and interfaces within the same sample. Also, it provides a unique opportunity to study the effects of material deposition on the surfaces of the Wz crystal segments which are relatively unexplored for III–V materials due to their unavailability in bulk form.

7.1 Sample preparation

When transferring NWs to a preferred substrate, two methods are commonly used, referred to as the close-proximity (CP) method and cleanroom tissue method. The latter refers to using a piece of cleanroom tissue and gently swiping it on the surface of the NW growth sample, resulting in a NW-covered tissue. Swiping the tissue over

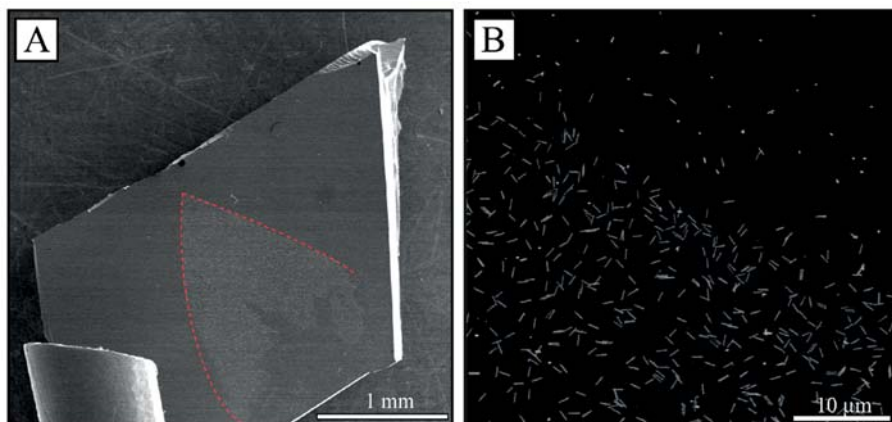


Figure 7.1. SEM images of InAs NWs deposited onto an InAs{111}B-type substrate *via* the CP method. (A) Shows large parts of the substrate. The NW-covered area (marked by red dashed lines) have a brighter contrast with respect to the substrate surface. (B) Zoomed-in at the border of the NW area of the sample. Image courtesy of Martin Hjort.

a clean substrate will result in a low concentration of NW on the surface. For STM studies, this method is unfavorable due to the low coverage of NWs on the surface, which significantly increases the time it takes to find a suitable NW to image. For this purpose, it is more favorable to use the CP method which in principle means that the NW growth-sample is brought into direct contact with another substrate surface [48]. By gently applying pressure on the backside of the substrate a high density of NWs is transferred, corresponding approximately to the density of the growth substrate. Also, by varying the applied pressure, a gradient in NW-coverage can be obtained on the substrate. A sample with NWs deposited using the CP method is shown in Figure 7.1.

In general, it is favorable to use a substrate of the same material as the investigated NWs consist of. This has several benefits; the substrate can be used as a reference for STS measurements and the deoxidation process. Also, the NWs appear to adhere better to surfaces of similar elemental composition, possibly due to “alloying” during annealing of the sample. For all studies related to this thesis {111}B-oriented substrates were used. These substrates have empirically been shown to be more favorable in comparison to other readily available surfaces such as the (100)-type when it comes to NW adhesion.

Table 7.1. The table shows temperature and time intervals for hydrogen cleaning of a number of III–V systems when using a hydrogen chamber pressure of 2×10^{-6} mbar. The procedure will produce well ordered, flat and oxide free surfaces. The temperatures provided in the table were measured with a pyrometer.

	InAs	GaAs	InP	GaSb	InSb
Temperature [°C]	360–400	450–600	400–420	450–520	380–400
Time [min]	25–35	30–90	25–35	45	25–35

7.2 Removal of native oxides

Native oxides on most III–V semiconductors could in principle be removed by annealing the sample to approximately 600°C. For some material systems, such as InAs, this is not advisable as the material start to decompose above 400–420°C. Sputtering, using for instance Ar-ions, would be another option. However, the method is destructive to some degree, and the high kinetic energy of the Ar-ions would most probably result in Ar-incorporation into sub-surface layers, and possibly also the bulk, of the NWs. For many materials such issues can be solved by annealing, but in the case of III–V materials it does not work due to evaporation of the group V element. Other possibilities would be annealing in an As-atmosphere [202], or capping (covering) the sample in another material—which can easily be removed by annealing—before exposing the sample to ambient conditions. The latter method is commonly used for MBE grown samples, but is not possible with the MOVPE setups.

Our method of choice is to reduce the desorption barrier of the oxides by annealing the sample in a stream of hydrogen radicals [208]. A chamber pressure of 2×10^{-6} mbar of hydrogen is often used for this procedure. The method allows for native oxide removal of InAs at 360–400°C, which conveniently is below the decomposition temperature for As in InAs. I can attest that the hydrogen must be radicalized for the procedure to work; a days-worth of experimental time at a synchrotron was spent by, unsuccessfully, trying to clean a sample with the hydrogen beam-shutter closed such that no hydrogen radicals could reach the sample. However, if the beam shutter was instead opened, the cleaning was successful. Cleaned samples will stay oxide-free for up to a week in an ultra-high vacuum environment ($P < 1 \times 10^{-11}$ mbar).

Interestingly, the atomic hydrogen cleaning procedure is effective for most III–V materials that I have investigated, and usually within the same temperature ranges, which allows for easy cleaning of material heterostructures. In Table 7.1 I have summarized parameters that have been used to successfully clean InAs, GaAs, InP, GaSb, and InSb.

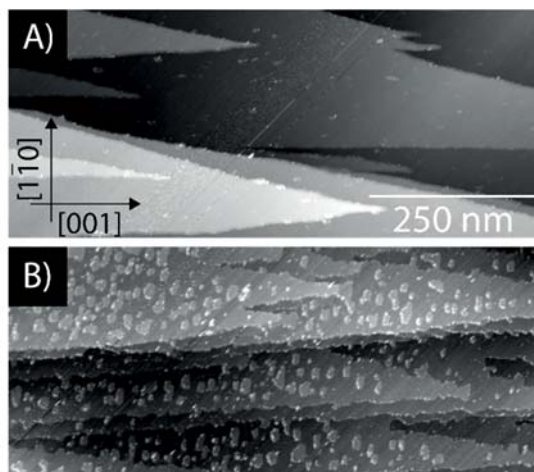


Figure 7.2. The figure demonstrate the morphological effects of hydrogen treatment and oxide removal on the surface of InAs. The image depict cleaved InAs {110} surface, before (A) and after (B) hydrogen treatment. Only the first monolayer of the surface is found to be affected (island-formation). The general surface morphology remains the same. $V_T = -2.5$ V, $I_{set} = 200$ pA.

7.2.1 Effects on surface morphology

For investigations into the atomic scale surface morphology of the NW sidewalls, it is vital to know in what way the hydrogen cleaning-procedure affect the surface morphology. To this end, a series of experiments were performed on {110}-type InAs surfaces. A {110}-type wafer was cleaved in-vacuum, using a specially designed sample holder, resulting in a {110}-type surface free of native oxides. STM imaging of this surface reveals the “true” surface morphology of a {110}-type surface. The sample was then exposed to ambient conditions to form a native oxide, which later was removed using the hydrogen cleaning-procedure. For the cleaned sample the general surface morphology remains the same with the exception of a formation of ML high islands as well as a small roughening of surface step-edges. When hydrogen-cleaning a cleaved sample that is not oxidized, no apparent change in surface morphology is observed with the exception of a slight roughening of step edges. These observations suggest that only the topmost surface layer is affected by the hydrogen-treatment and that the ML-high islands are formed by material residues that are released when the oxide is removed. The results are summarized in Figure 7.2, but also presented in more detail in Paper II.

7.3 Surface modification

During my work, I was privileged to visit Chris Palmstrøm's research group at the University of California at Santa Barbara (UCSB) and use their unique vacuum system. It consists of an impressively large network of growth chambers and characterization instruments, including a 5 K STM setup, all connected into one enormous vacuum system. Such a setup allows for the sequential growth and characterization of exciting heterostructures without breaking vacuum [209-212].

The system also provides an excellent opportunity to study the effects of material deposition on NW surfaces. Studies of material deposition on NWs can lead to the discovery of new and interesting phenomena due to the large number of possible facet types, material variations, and crystal phase heterostructures available within a single NW. For instance, when depositing submonolayer amounts of Sb on GaAs NWs, it has been shown that, after annealing, the Sb incorporate within the first surface layer of the NW by replacing As in the lattice, such that GaSb is formed [37]. The substitution effect was shown to be four times greater for the Zb{110}-type facet compared to the Wz{11-20}-type, likely due to a lower energy barrier for the Sb-for-As exchange on the Zb-facet. This type of crystal phase dependent incorporation can only be studied in NW systems for the majority of III-V semiconductors, as there is currently no other way to gain access to the Wz crystal phase. Such a non-isotropic incorporation effect could be used favorably to form atomically thin $\text{GaAs}_{(1-x)}\text{Sb}_{(x)}$ layers, selectively, on different sections of GaAs NWs, to act as QWs or delta-doping layers.

7.3.1 Bi deposition

An extremely relevant material combination to study in a similar fashion is GaAs combined with Bi as it can be used favorably for topological effects [213, 214], bandgap engineering [215], and spintronic devices due to the giant spin-orbit coupling of Bi [216, 217]. To this end, the system at UCSB was used to deposit 0.5 ML of Bi on top of heterostructure Zb/Wz GaAs NWs, which had been transferred to a GaAs{111}B-type substrate. The deposition was performed at an already cleaned sample using an MBE source and a sample temperature of 250°C. The sample was then transferred to the 5 K-STM system without breaking vacuum.

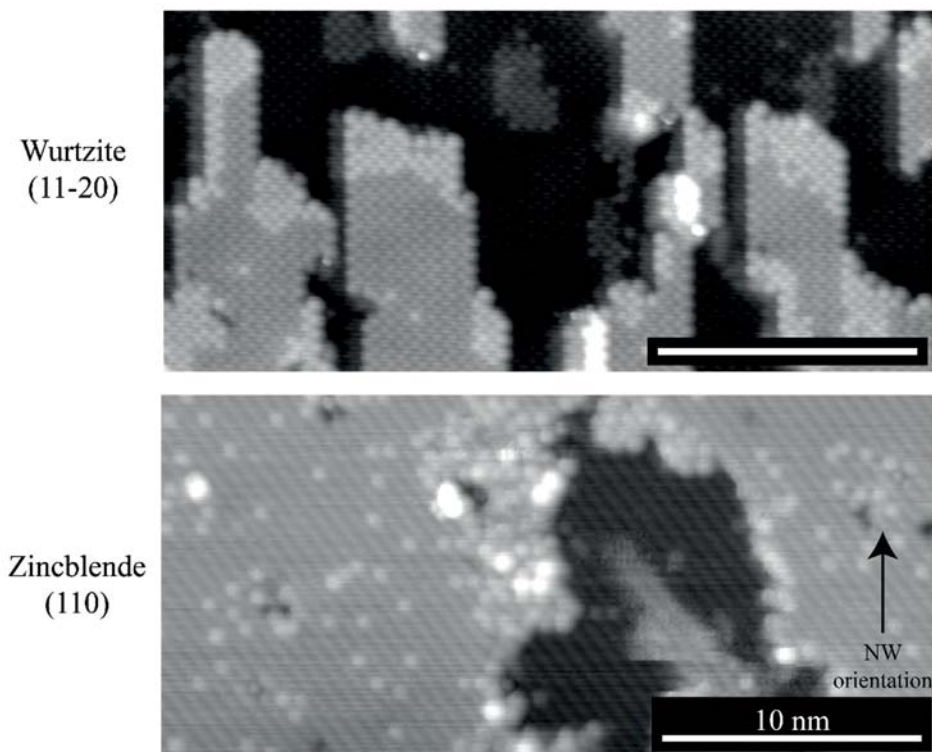


Figure 7.3. Bi incorporate differently depending on the crystal structure and facet orientation. The figure show STM images from $\{11-20\}$ -type and $\{110\}$ -type facets after Bi-deposition, respectively. Brighter areas and spots correspond to Bi inclusions. $V_T = -4.4$ V, $I_{set} = 100$ pA for both STM images.

As discussed in detail in Paper III, the effects of Bi-deposition are different from what have previously been observed with Sb [37]. Instead of a straightforward difference in a number of incorporation-events between the Zb $\{110\}$ surface and the Wz $\{11-20\}$ surface, different patterns were formed. In Figure 7.3 filled state STM images (imaging As) of the Zb $\{110\}$ surface as well as the Wz $\{11-20\}$ surface after Bi deposition are shown. The brighter protrusions in the images correspond to Bi. Based on their apparent height, see Figure 7.4, they appear to have replaced As-atoms in the top surface layer, forming local pairs of GaBi, rather than sitting intop of the surface. On the Zb $\{110\}$, the Bi appear to be distributed randomly at the surface and is predominantly found without any Bi-neighbors. On the Wz $\{11-20\}$ surface, however, the Bi seems to incorporate in clusters, forming atomic chains or “terraces.”

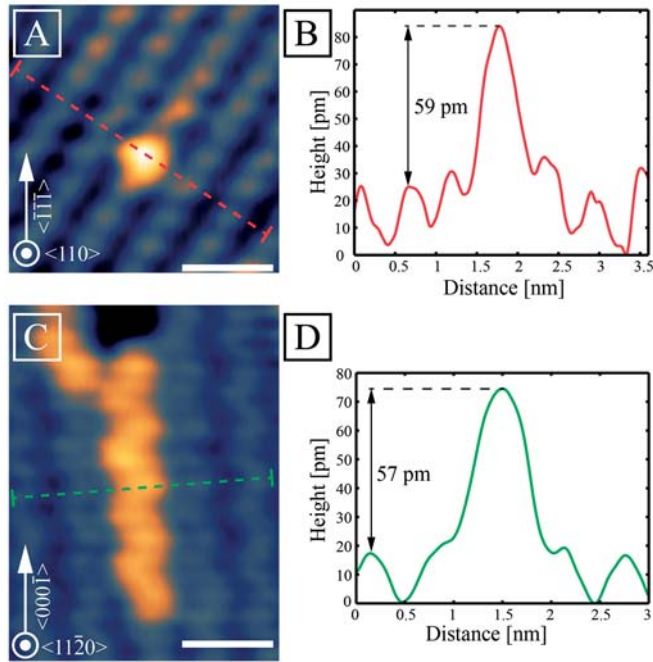


Figure 7.4. STM image obtained at room temperature of Bi in GaAs. For reference, the height of an atomic step on the GaAs is approximately 210 pm. Scale bar is 1nm. (A) Single Bi atom incorporated in the $\{110\}$ surface of Zb, $I_{\text{set}} = 210$ pA, and $V_T = -4.6$ V. (B) Line profile as marked in (A). (C) Chain of Bi atoms incorporated in the $\{11\bar{2}0\}$ surface of Wz, $V_T = -3.5$ V and $I_{\text{set}} = 210$ pA. (D) Line profile as marked in (C).

Relevant for both facets is that the number of As-for-Bi exchange events is higher in the vicinity of atomic steps or vacancy sites, as shown in Figure 7.5, signifying that such defects act as incorporation-centers for the Bi. For the Zb, Bi-incorporation appears to be preferential *via* the $\{111\}$ A/B-type step edges. For the Wz $\{11\bar{2}0\}$ -type surface, the Bi incorporates *via* the $\langle 0001 \rangle$ A/B-type step edges, which are polar in contrast to the $\langle 10\bar{1}0 \rangle$ -oriented step edges. Any preference for A-type or B-type polarity is not clear from the images as the NW alignment is not known. The atomic chains are most likely formed due to a low-energy diffusion path along the $\langle 0001 \rangle$ -type directions, similarly to what is seen for GaAs and InAs where elongated terraces are naturally formed on the Wz $\{11\bar{2}0\}$ -type facets (as shown in Paper IV and V).

After imaging a total area of 3800 nm^2 and 3000 nm^2 , for Zb $\{110\}$ and Wz $\{11\bar{2}0\}$, respectively, and counting the number of Bi incorporation events, a Bi-density of $\delta_{\text{Wz}\{11\bar{2}0\}} = 0.41 \pm 0.30 \text{ Bi/nm}^2$ and $\delta_{\text{Zb}\{110\}} = 0.33 \pm 0.10 \text{ Bi/nm}^2$ was found for the two facets. The large standard deviation in the Wz case is most likely explained by a va-

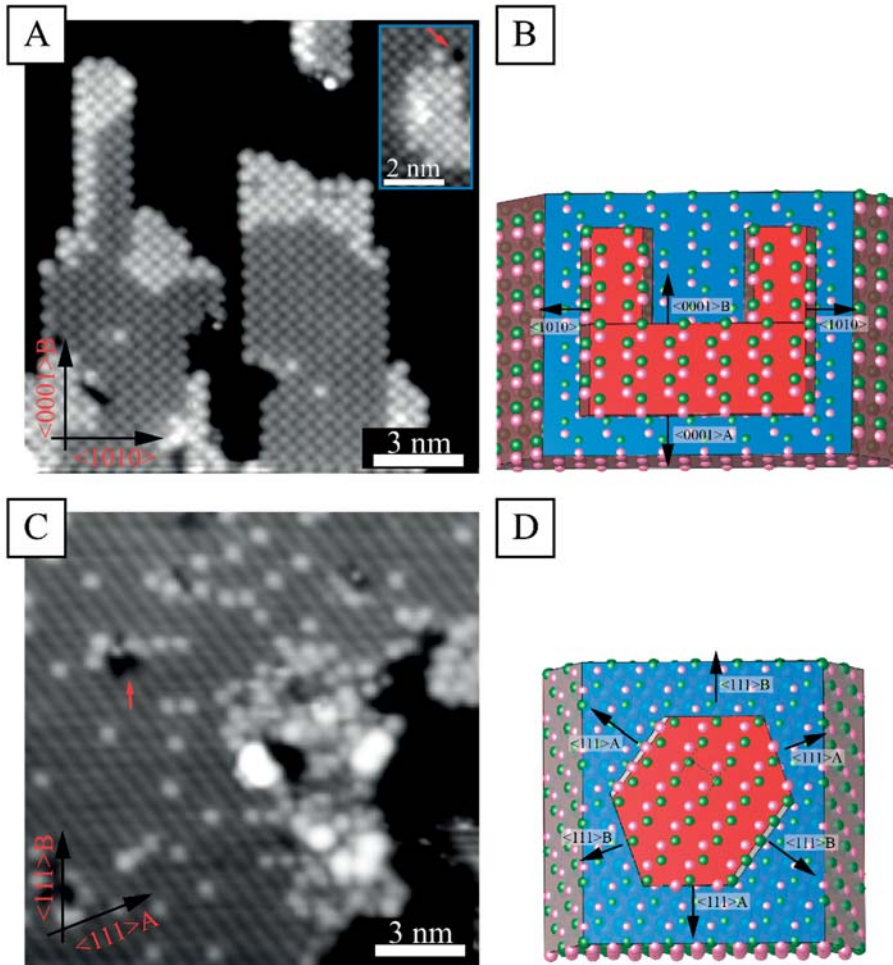


Figure 7.5. The Bi incorporates into the surface layer *via* atomic step edges and vacancies in both the $\{110\}$ - and $\{11\bar{2}0\}$ -type surfaces in GaAs NWs. (A) And (B) show atomically resolved STM images and a model, respectively, of an $\{11\bar{2}0\}$ -type surface. The bright protrusions correspond to Bi atoms. Bi enters the surface *via* the $\langle 0001 \rangle_{A/B}$ -oriented step edges and vacancies. (C) And (D) show STM image and model of the $\{110\}$ -type surface, where Bi incorporates *via* the $\langle 111 \rangle_{A/B}$ -type step edges as well as vacancies. $V_T = -4.4$ V, $I_{set} = 100$ pA for both STM images.

riation in step density in the different images used for the Bi-counting. Nonetheless, no clear preferential incorporation is found between the two facets in terms of amount.

Interestingly, STS measurements on the Bi-chains, formed on the $Wz\{11\bar{2}0\}$ facets, show signs of a size-dependent confinement effect within the chains. A distinct feature on the valence band side shows up uniquely on the Bi chains, and

the position of the state changes depending on the chain length. This is similar to what has been observed for atomic chains of In on metal surfaces [55] and would be interesting for quantum computing applications. The GaAs+Bi-system is however much more favorable for such applications compared to a metal-system due to a number of key points: it is a semiconductor system, the chains are self-assembled, and finally, the Bi layer could potentially be covered in a few ML of GaAs to protect the chains from external perturbations. From an electronics point of view, a semiconductor system is far more interesting due to its relative ease to be integrated into devices compared to a metal-based system. Self-assembly of Bi chains allows for large-scale fabrication were the chain length could potentially be controlled by regulating the crystal segment lengths.

8 NANOWIRE DEVICES

During the course of my work, means to perform STM/S investigations of NW surfaces while the NW was in operation were developed, *i.e.*, having an electrical potential applied to the NW [218-220]. The performance of NW-based devices is generally below what is theoretically expected due to perturbations from surface- or crystal structure defects (stacking faults) [23]. Also, conventional electronics generally degrade over time as a result of electro-migration, where material from the surface transports along the electric field gradient. The material transport will slowly degrade device performance, and ultimately renders the device useless [221, 222]. For NW systems, these type of performance-reducing effects is generally hard to study using conventional techniques, such as contact-electrical measurements, as those cannot distinguish between surface- and bulk conductance or the effects of individual defects [23]. STM/S is however capable of performing potential maps with atomic resolution such that the effects of individual defects such as atomic steps, vacancies, adatoms or crystal phase variations can be determined. An example is shown in Figure 8.1, where the p-n junction has been mapped in an InP NW.

8.1 Device design

Performing STM on a contacted NW poses a challenge as conventional planar NW devices, used for contact-electrical measurements, are based on non-conducting SiO substrates [3]. In such devices, gradually thinner gold contacts are connected to the ends of the NWs, *via* electron beam lithography (EBL), such that an external bias can be applied over the NW. To perform STM imaging on such a device, the STM tip has to be manually placed (*via* optical inspection) on top of the thicker end of the gold contact and then (*via* STM imaging) slowly moved along the contact towards the NW. This was extremely time consuming, and the risk of “falling off” the contact and crashing the STM tip into the insulating substrate is high.

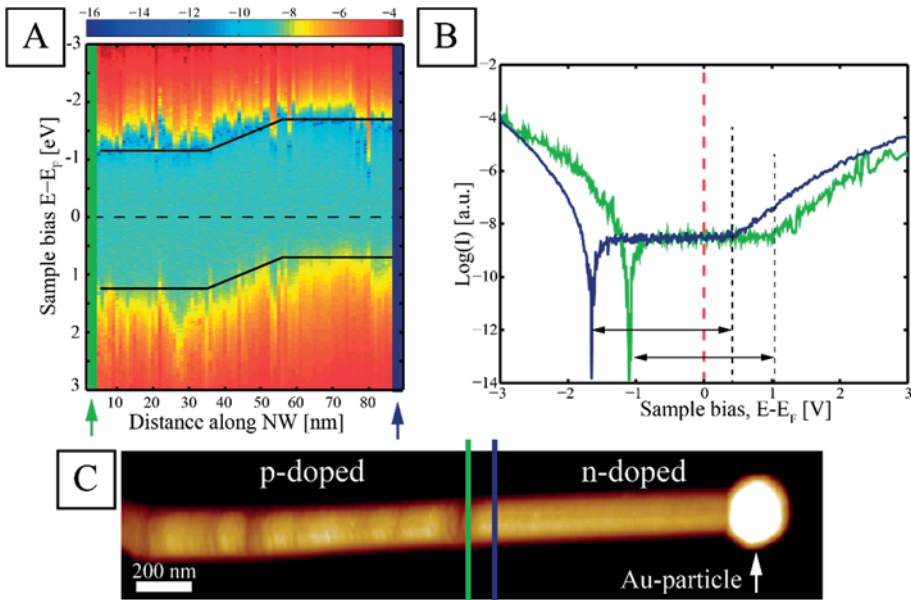


Figure 8.1. Low-resolution potential profile along a p-n junction in an InP NW. (A) STS line profile, *i.e.*, the logarithmic tunneling current as a function of voltage and position along p-n junction. Dashed line denotes Fermi level. Solid lines mark approximate position of valence and conduction band edges. The depletion region is *ca.* 15 nm long. (B) I–V spectra obtained from positions marked by a green and blue arrow in (A), illustrating the shift in potential between the two regions of the NW. (C) Large-scale STM image of InP NW. Green and blue line denote the start and end of STS line profile from (A).

In our device designs, a conductive substrate surface is instead used, allowing for STM imaging over the whole device, with little risk of tip crashes. SEM images and schematic models of our device designs are shown in Figure 8.2. A Si substrate is used as a template on which a SiO layer is grown. As described in detail in Paper VIII, EBL was used to form large sheets of 15 nm thick conductive Ti, which in turn is capped by a 2 nm thick Au layer, on top of the Si-substrate. The Ti sheets are separated by 0.5–1.5 μm wide trenches such that they can be individually biased. The SiO at the bottom of the trench is etched away, exposing the underlying semiconducting Si surface. The underlying Si surface is grounded, allowing for STM-scanning within the trench. The NWs are then suspended between two adjacent Ti sheets, which can be independently biased, allowing for a potential drop along the section of the NW that is suspended over the trench. The NWs are placed over the trench with a focused ion beam (FIB) tip, using an optical microscope for navigation. Alternatively, the NWs can be deposited stochastically *via* the paper-tissue method—resulting in a large number of NWs in the area of a trench—and relying on luck that one or a few NWs end up lying across the trench. In some ver-

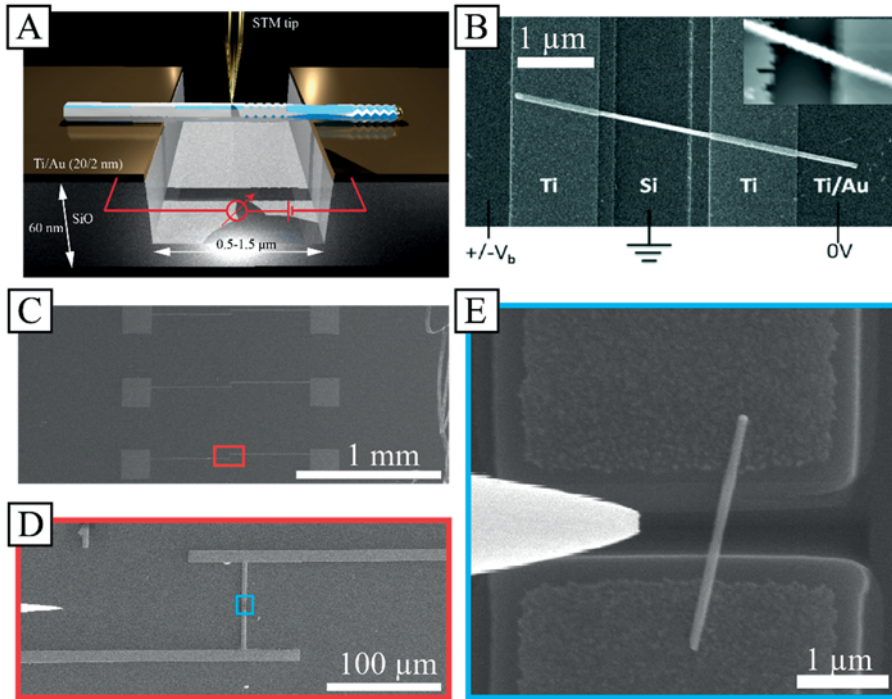


Figure 8.2. The figure shows NW device designs where all parts of the surface are conductive such that STM imaging can be performed without the risk of tip crashes. (A) Schematic model of the device. (B) SEM image of NW device with the Ti holding layer. The inset shows low-resolution STM image of the NW as well as the two contacts. (C)–(E) Shows consecutively more zoomed in versions of the latest generation device with shorter trenches and only single NWs at each contact. The bright tip that is visible in (D) and (E) is the FIB-tip that was used for placing the NWs at the trench. Figure (B) adapted from Paper VIII, [223].

sions of the device design, a holding layer of Ti was placed on top of the NW to immobilize it. This idea was later scrapped as it involved an additional processing step that was found to be unnecessary. This type of device setup can withstand temperatures at least 450°C such that the native oxides of the NW surface can be removed for most III–V materials *via* annealing in a flux of atomic hydrogen. In Paper VII, it is shown that the surface oxide reduces the conductivity of the NWs by several orders of magnitude. This effect was measured by recording the conductance of a NW device pre- and post-oxide removal.

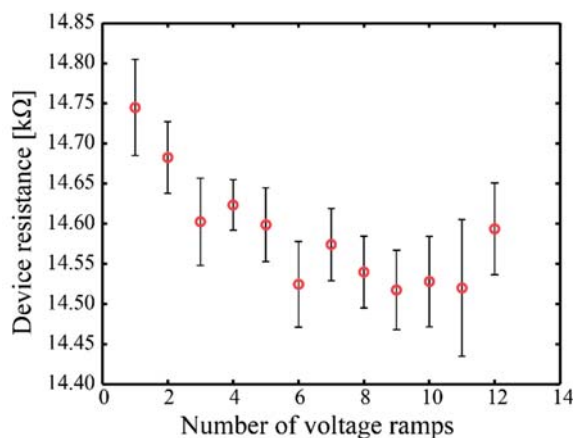


Figure 8.3. A decrease in device resistance is often found after several consecutive voltage-ramps. Here, the effect is demonstrated for an individual InAs NW that was ramped between -1 V and $+1$ V. The errorbars show the standard deviation.

8.2 Device operation

Using this type of device design, a contacted NW can be found within one hour with the help of previously obtained optical/SEM images and visual markers for reference. The design allows for voltage ramping while simultaneously performing STM/S imaging. For NWs with diameters of ca 100 nm, a 4–5 V or 1 V bias can be applied before device breakdown for the multi and single NW devices, respectively. Nonetheless, great care had to be taken to use high-quality equipment as voltage spikes would destroy the NW. For this reason, it is also recommended to use rather slow voltage ramps when applying an external bias. An additional reason for a slow ramp is the rapid increase in NW temperature when a current is running through it, resulting in thermal drift. Surprisingly, thermal drift dissipates within a minute, suggesting a rapid thermal dissipation with good heat transfer between the Ti/Au electrodes and the NW.

The electrical contact between the Ti/Au and the NWs was found to be very good, such that at least 90% of the applied bias dropped over the NW. The device resistance is instead predominantly due to the low conductance of the NW. Typical resistances are in the M Ω - and k Ω -range pre- and post-removal of the native oxides, respectively. These values do however vary greatly depending on the NW properties, such as material, doping concentration, and axial/radial composition. Interestingly, the device resistance experience a slight reduction after having experienced a few voltage ramps. As shown in Figure 8.3, the improvement is small, only on the order of a few hundred Ω , and commonly saturates after 5–10 voltage-

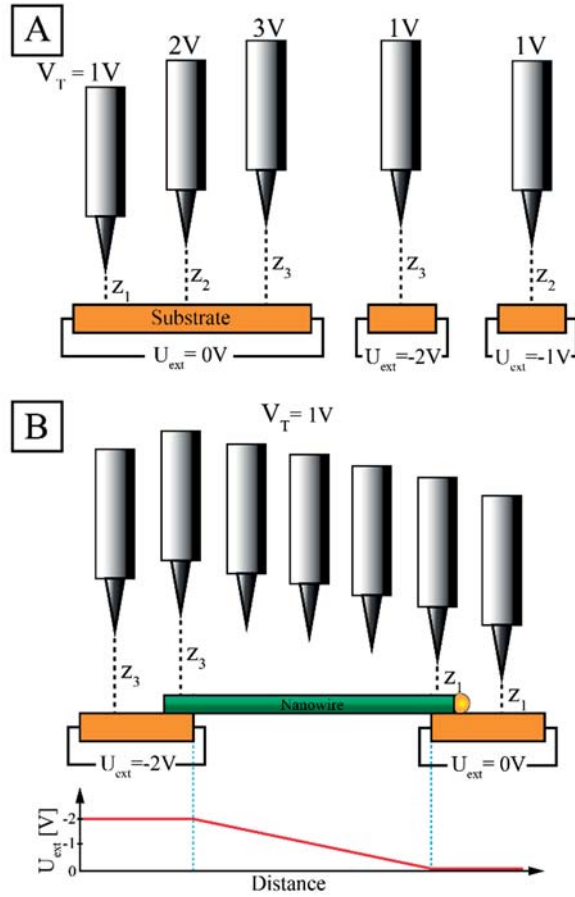


Figure 8.4. Schematic images illustrating the relationship between tip-sample separation (z), tip-sample bias (V_T), and an externally applied bias on the substrate (U_{ext}). The effective tip-sample separation for a surface with a uniform or varying surface potential is shown in (A) and (B), respectively.

ramps. The effect is only present for cleaned NWs suggesting that it may be due to sequential alloying between the NW and the Ti/Au.

When running the STM in constant-current mode, the setpoint bias between the tip and sample, V_T , will determine the tip-sample separation, z , for a uniform sample. When an external bias, U_{ext} , is applied to the sample (as in the case for the NW devices) it will change the local surface potential of the sample such that the net tip-sample bias is altered, ultimately resulting in a different tip-sample separation, as illustrated in Figure 8.4. For a non-uniform sample, such as a contacted NW, where the surface potential continuously changes along the NW growth axis due to

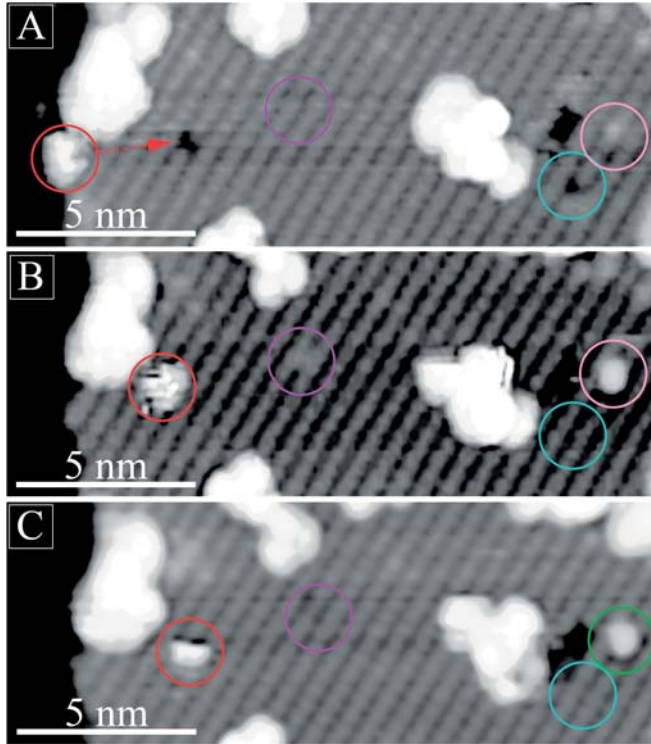


Figure 8.5. When NWs are externally biased the rate of adatom and vacancy movement appears to increase. The images (A)–(C) depict a GaAs NW $\{110\}$ -type surface with several defects, obtained 8.5 min apart from each other. For all images an external bias of $U_{\text{ext}} = 3$ V is applied to the NW. For all images $V_T = -2$ V and $I_{\text{set}} = 50$ pA. Between (A) and (C) several surface features have moved (marked by rings). As shown in Paper VIII, the migration effect is much more pronounced for InAs surfaces where a large number of defects are healed in a matter of minutes.

the potential drop between the device contacts, the effective tip–sample bias and distance will change in accordance with the varying surface potential along the NW. One has to be mindful of this effect when imaging semiconductor surfaces as an applied external bias can result in an effective tip–sample bias that only allows for tunneling into the bandgap of the semiconductor, resulting in a tip crash. Similarly, extremely high tip–sample voltages can be reached, inducing unwanted tip changes. It is thus recommended to always account for the external bias by changing the tip–sample setpoint bias accordingly.

The correlation between tip–sample separation, tip–sample bias, and an externally applied bias could be used beneficially in Paper VIII to determine the potential drop over an individual stacking fault (single bilayer of Zb) in a Wz NW. Due to interfacial effects, and differences in bandgap between Wz and Zb, stacking faults

are assumed to act as small resistances in NWs [23], but their individual effect has not been quantitatively measured. In Paper **VIII** we show STM images of the stacking fault as observed from a {10-10}-type surface, obtained using the same tip-sample setpoint bias, $V_T = -1$ V, but using external biases U_{ext} varying from -4 to +0.2 V. The tip-sample separation for images obtained at $U_{ext} = 0$ V purely depends on local variations in sample height (and electronic effects) for a given V_T . However, if an external bias is applied, the resulting tip-sample distance in each point of the STM image will depend on the local height variation (and electronic effects) as well as the varying changes in surface potential due to the potential drop along the NW growth axis. By subtracting an image obtained using a non-zero external bias from the image obtained at $U_{ext} = 0$ V, only the height information related to the local variations in surface potential due to the external bias remains in the image. A change in contrast (*i.e.*, tip-sample separation) at the stacking fault, consistent with a local potential drop induced by the intrinsic resistance of the stacking fault, could be observed.

This may seem to be a rather convoluted way to obtain the changes in local potential within an image as the STM/S is perfectly capable of obtaining such information directly *via* for instance spectroscopy maps. However, the STM setup at the time only allowed for room temperature measurements such that the long imaging times required for spectroscopy maps, in the order of hours for dI/dV -V maps, would result in a useless image due to severe thermal drift.

As discussed in Paper **VIII**, by performing atomically resolved imaging and simultaneously applying an external bias, it was possible to study the morphological effects of having an electric field gradient along the NW. We found that a material dependent self-healing effect occurred for moderate to high external biases as a result of electromigration. For a sufficiently large bias (above 2 V and 3 V for InAs and GaAs, respectively), adatoms would migrate along the electric field gradient and occupy surface vacancies, reducing the net amount of surface defects on the NW. The effect scales with the applied external bias, being more pronounced at higher values. In Figure 8.5, this effect is demonstrated by atomically resolved STM images of an {11-20} surface of a GaAs NW device. In all images, an external bias of 3 V is applied during image acquisition, and the images are obtained with an 8.5-minute separation. Several surface-features change in between the images, consistent with a migration of material along the NW surface. As shown in Paper **VIII**, this effect is more significant for InAs compared to GaAs, most likely due to the differences in surface energy between the two materials. In the case of InAs, also larger-scale morphological changes occurred were terraces would move and change shape.

This type of self-healing effect could potentially be used to improve the performance of NW devices *via* a reduction in the net amount of surface defects. However, the results presented here are preliminary, and further studies would be of interest. For example, the long-term effects of applied biases as well as quantification of how the

potential drop along the NW is affected by various types of surface defects and heterojunctions could be investigated.

9 CONCLUDING REMARKS AND OUTLOOK

The work presented in this dissertation has been devoted to atomic scale characterization of III–V NW surfaces. The III–V NW systems have shown great potential for improved and novel applications within MOSFET electronics, photonics, photovoltaics, and quantum information-technologies [7-10, 95, 97, 117, 150, 160]. My work is motivated by the shortage of atomic-scale surface studies of III–V NWs, despite the critical role the surface plays for determining the NW characteristics [24, 25]. In fact, when I started my work only two studies were published which could demonstrate atomic resolution on the sidewall facets of III–V NWs [27, 198]. Since then, a total of fifteen atomically resolved STM/S studies on III–V NW surfaces have emerged (of which I have contributed to seven) [27, 35-38, 47, 70, 89, 198, 223-228]. When reviewing the current publications on the topic, I find that they can roughly be divided into three sub-categories: (I) surface characterization and modification, (II) characterization of heterostructure interfaces, and (III) characterization of NW devices *operando*.

Surface characterization and modification with the purpose to control surface properties or create material heterostructures—such as QWs, QDs, or delta-doping layers—have significant relevance for the development of novel NW devices. Information at the atomic scale on the origins of surface states, step densities, nucleation sites, and growth modes are essential for consistent growth and control over the NWs and their electronic properties. To this end, Paper **I** deals with the atomic level overgrowth dynamics on NW surfaces and demonstrates that crystal phase interfaces and surface types play a major role in determining growth modes and nucleation sites. It also demonstrates that the small-sized facets of the NW sidewalls can be determining factors for the formation of surface reconstructions that normally do not appear within the given parameter-space. Such effects are important to consider regarding both growth modes and electronic properties. A natural progression from the present study would be to move onto core–shell heterostructures. One approach to investigating core–shell growth could be to sequentially grow single MLs (or less) of material A, on a NW of material B, while performing STM characterization in between the growth-sessions to better understand the origin of interfacial defects and material intermixing.

Paper **III** deals with the growth of submonolayer quantities of Bi on GaAs NWs, and further demonstrates the prominent role of the surface characteristics concerning the growth process. The Bi is found to form different structures on the NW surfaces depending on the facet type, with a tendency towards forming self-

assembled atomic chains of Bi on the {11–20}-type surfaces in the Wz crystal phase. Initial measurements show signs of quantum confinement within the atomic chains, making them interesting for applications in quantum computing and quantum information technologies, and warrants further study. The Bi–GaAs system is especially interesting in this regard as the chains could potentially be overgrown with an epitaxial layer of GaAs to protect them from surface-induced perturbations and ambient conditions.

Surface selectivity as a concept is also worth exploring further in terms of selective radial overgrowth to form crystal-phase dependent QW-structures or delta-doping layers. In this regard, exploring the parameter-space for controlling the surface selectivity, in terms of both the NW sample and the Bi-growth conditions, could be of value. For instance, varying parameters such as the NW diameter, crystal segment lengths, and crystal phase interface types (*i.e.*, V-grooves of a TSL) could lead to interesting differences in the overgrowth dynamics and Bi-incorporation. Concerning growth properties, systematic studies of temperature dependencies, material amounts, and post-treatment processes could also contribute towards atomic scale modification of NW structures. Finally, it is noteworthy that the material system, *i.e.*, Bi–GaAs, is interesting in itself in the context of fundamental physics such as topological effects [214], a field in which the NW geometry already has proven useful [94]. The ability of selectively modifying the properties of only the topmost surface layer of the NWs could open up new avenues for studying topological phenomena.

In Paper **II** and **VII**, a method for oxide removal of NW surfaces that apply to a large range of III–V systems is demonstrated. It is shown that only the topmost surface layer is affected by the procedure, making it an excellent alternative to material capping. Paper **II** also demonstrates that the step density can be controlled by the growth parameters. Means for controlling the atomic scale surface morphology are highly relevant as shown in Paper **VI** where atomic steps are found to give rise to surface states. Surface states can be detrimental to the performance of NW devices that rely on the confinement of charge carriers *via* bandgap engineering. Paper **VII** also demonstrates the importance of developing surface passivation techniques for improving NW device performance. In the paper, the presence of the native surface-oxides was shown to reduce the conductivity of the NWs by several orders of magnitude.

Characterization of heterostructure interfaces in III–V NWs has the potential to improve the performance of NW-based devices. For instance, in contrast to the well-established material heterostructure junctions, crystal phase engineering has the potential for modulating the potential landscape in NWs with atomic-level precision. However, direct measurement of the electronic properties of the Wz crystal phase is difficult, and no consensus regarding its bandgap has been reached for many materials. Paper **IV**, **V**, and **VI** deal with the electronic characterization of crystal phases in the GaAs and InAs systems. It is demonstrated that the bandgap

and band alignment between Wz and Zb can be extracted with STS. However, in the case of InAs, the true band alignment is masked due to Fermi level pinning induced by n-type defects, indicating that developing methods for surface passivation is essential for the predictable and consistent behavior of NW devices. Paper **VI** also demonstrates that the crystal-phase dependent bandgap is valid down to a single atomic bilayer, a result which holds significance for crystal phase engineering. In the context of crystal phase engineering, further characterization of quantum confinement within small material- and crystal phase junctions would be interesting for developing arrays of QDs within single NWs. Such arrays could function as a system of qubits within a quantum computer.

Further exploration into how surface defects affects the electronic properties of material or crystal phase interfaces is also of interest. Recent efforts towards using heterojunctions in III–V NWs as transistors with on-state voltages below the fundamental sub-threshold limit (*i.e.*, tunnel field effect transistors operating below 60 mV/decade) are currently limited by mid-gap states and trap-assisted tunneling. These effects could be related to defects at the surface in the vicinity of the heterojunction interface [229]. For further improvement of such devices, the origin of bandgap tails and trap states could be characterized by STM.

Characterization of NW devices *operando* is a natural step towards correlating electronic properties and surface defects in NWs. The performance of NW devices is often hampered by defects and imperfections. Deconvolution of the influence of each defect type, such as surface vacancies, atomic steps, and stacking faults, is conventionally difficult, and optimization of the NW performance is often done *via* a trial and error approach. The results of Paper **VII** and **VIII** demonstrate a proof of principle for atomic-scale characterization of the surfaces of NW devices *operando*, a prerequisite for taking performance-characterization of NWs beyond trial and error. Also, interesting phenomena such as electromigration and its self-healing effects on surface defects are presented in Paper **VIII**. Such effects could open up possibilities for creating highly ordered crystals for improved device performance. The current study could be expanded by investigating the extent of the self-healing effect in terms of defect types, materials, surfaces, and bias thresholds. Also, studies of electromigration in the context of long-term exposure to biases, or rapid switching of voltages, could be of interest for the NW device community.

Operando STM studies of NWs could be further expanded by increasing the complexity of the NW. By adding, for example, heterojunctions, dopant gradients, or adsorbates, valuable insights for optimizing the performance of NW devices for a large number of applications could be gained. These type of measurements could naturally be progressed into a low-temperature environment that allows for a more detailed characterization of defects and heterostructures, for instance *via* high-resolution potential-mapping. The complexity of the measurement could be further increased by combining *operando* measurements with a laser system to measure the photo-response of the NWs.

In conclusion, STM on NWs have been, and will most likely continue to be, important for the atomic level characterization of III-V NWs. However, the low temporal resolution of STM leaves many electronic properties of the NW surfaces to, currently, only be investigated at the theoretical level. I believe that if the NW system is to act as a foundational building block within future applications for electronics and photonics, the characterization methods must evolve to allow for investigation of both temporal and spatial dynamics simultaneously. Perhaps by combining pulsed light sources—with ultrafast repetition rates—and scanning probe techniques for a combined temporal and spatial characterization of nanostructures at the resolution limits of the respective methods. This being said, I am pleased for having been given the opportunity to contribute to early work of NW surface characterization, and I expect the field to grow considerably in the coming years.

10 BIBLIOGRAPHY

- [1] Wallentin, J.; Persson, J.M.; Wagner, J.B.; Samuelson, L.; Deppert, K., and Borgström, M.T., High-Performance Single Nanowire Tunnel Diodes. *Nano Lett.*, 2010. **10**, 974-979.
- [2] Doornbos, G.; Holland, M.; Vellianitis, G.; Dal, M.J.H.V.; Duriez, B.; Oxland, R.; Afzalian, A.; Chen, T.K.; Hsieh, G.; Passlack, M., and Yeo, Y.C., High-Performance InAs Gate-All-around Nanowire Mosfets on 300 Mm Si Substrates. *IEEE Journal of the Electron Devices Society*, 2016. **4**, 253-259.
- [3] Dey, A.W.; Thelander, C.; Lind, E.; Dick, K.A.; Borg, B.M.; Borgstrom, M.; Nilsson, P., and Wernersson, L.E., High-Performance InAs Nanowire Mosfets. *IEEE Electron Device Lett.*, 2012. **33**, 791-793.
- [4] Egard, M.; Johansson, S.; Johansson, A.C.; Persson, K.M.; Dey, A.W.; Borg, B.M.; Thelander, C.; Wernersson, L.E., and Lind, E., Vertical InAs Nanowire Wrap Gate Transistors with $F_t > 7$ GHz and $F_{max} > 20$ GHz. *Nano Lett.*, 2010. **10**, 809-812.
- [5] Larsen, T.W.; Petersson, K.D.; Kuemmeth, F.; Jespersen, T.S.; Krogstrup, P.; Nygård, J., and Marcus, C.M., Semiconductor-Nanowire-Based Superconducting Qubit. *Phys. Rev. Lett.*, 2015. **115**, 127001.
- [6] Thelander, C.; Agarwal, P.; Brongersma, S.; Eymery, J.; Feiner, L.F.; Forchel, A.; Scheffler, M.; Riess, W.; Ohlsson, B.J.; Gösele, U., and Samuelson, L., Nanowire-Based One-Dimensional Electronics. *Materials Today*, 2006. **9**, 28-35.
- [7] Kim, S.K.; Day, B.; Cahoon, J.F.; Kempka, T.; Song, K.D.; Park, H.G., and Lieber, C., Tuning Light Absorption in Core/Shell Silicon Nanowire Photovoltaic Devices through Morphological Design. *Nano Lett.*, 2012.
- [8] Hochbaum, A.I. and Yang, P., Semiconductor Nanowires for Energy Conversion. *Chem. Rev. (Washington, DC, U. S.)*, 2009. **110**, 527-546.
- [9] Saxena, D.; Mokkalapati, S.; Parkinson, P.; Jiang, N.; Gao, Q.; Tan, H.H., and Jagadish, C., Optically Pumped Room-Temperature GaAs Nanowire Lasers. *Nat. Photonics*, 2013. **7**, 963-968.
- [10] Yan, R.; Gargas, D., and Yang, P., Nanowire Photonics. *Nat. Photonics*, 2009. **3**, 569-576.
- [11] Wallentin, J.; Anttu, N.; Asoli, D.; Huffman, M.; Åberg, I.; Magnusson, M.H.; Siefer, G.; Fuss-Kailuweit, P.; Dimroth, F.; Witzigmann, B.; Xu, H.Q.; Samuelson, L.; Deppert, K., and Borgström, M.T., InP Nanowire Array Solar Cells Achieving 13.8% Efficiency by Exceeding the Ray Optics Limit. *Science*, 2013. **339**, 1057-1060.
- [12] Borgström, M.T.; Wallentin, J.; Heurlin, M.; Fält, S.; Wickert, P.; Leene, J.; Magnusson, M.H.; Deppert, K., and Samuelson, L., Nanowires with Promise for Photovoltaics. *IEEE J. Sel. Top. Quantum Electron.*, 2011. **17**, 1050-1061.

BIBLIOGRAPHY

- [13] Xu, S.; Hansen, B.J., and Wang, Z.L., Piezoelectric-Nanowire-Enabled Power Source for Driving Wireless Microelectronics. 2010. **1**, 93.
- [14] Boukai, A.I.; Bunimovich, Y.; Tahir-Kheli, J.; Yu, J.-K.; Goddard Iii, W.A., and Heath, J.R., Silicon Nanowires as Efficient Thermoelectric Materials. *Nature*, 2008. **451**, 168-171.
- [15] Svensson, J.; Dey, A.W.; Jacobsson, D., and Wernersson, L.-E., III–V Nanowire Complementary Metal–Oxide Semiconductor Transistors Monolithically Integrated on Si. *Nano Lett.*, 2015. **15**, 7898-7904.
- [16] Borg, M.; Schmid, H.; Moselund, K.E.; Signorello, G.; Gignac, L.; Bruley, J.; Breslin, C.; Das Kanungo, P.; Werner, P., and Riel, H., Vertical III–V Nanowire Device Integration on Si(100). *Nano Lett.*, 2014. **14**, 1914-1920.
- [17] Jiang, N.; Gao, Q.; Parkinson, P.; Wong-Leung, J.; Mokkapatil, S.; Breuer, S.; Tan, H.H.; Zheng, C.L.; Etheridge, J., and Jagadish, C., Enhanced Minority Carrier Lifetimes in GaAs/AlGaAs Core–Shell Nanowires through Shell Growth Optimization. *Nano Lett.*, 2013. **13**, 5135–5140.
- [18] Heiss, M.; Fontana, Y.; Gustafsson, A.; Wüst, G.; Magen, C.; O’Regan, D.D.; Luo, J.W.; Ketterer, B.; Conesa-Boj, S.; Kuhlmann, A.V.; Houel, J.; Russo-Averchi, E.; Morante, J.R.; Cantoni, M.; Marzari, N.; Arbiol, J.; Zunger, A.; Warburton, R.J., and Fontcuberta i Morral, A., Self-Assembled Quantum Dots in a Nanowire System for Quantum Photonics. *Nat. Mater.*, 2013. **12**, 439-444.
- [19] Dick, K.A.; Thelander, C.; Samuelson, L., and Caroff, P., Crystal Phase Engineering in Single InAs Nanowires. *Nano Lett.*, 2010. **10**, 3494-3499.
- [20] Friedhelm, B. and Abderrezak, B., Structure, Energetics, and Electronic States of III–V Compound Polytypes. *J. Phys.: Condens. Matter*, 2013. **25**, 273201.
- [21] Priante, G.; Glas, F.; Patriarche, G.; Pantzas, K.; Oehler, F., and Harmand, J.-C., Sharpening the Interfaces of Axial Heterostructures in Self-Catalyzed AlGaAs Nanowires: Experiment and Theory. *Nano Lett.*, 2016. **16**, 1917-1924.
- [22] Qian, X.; Kawai, M.; Goto, H., and Li, J., Effect of Twin Boundaries and Structural Polytypes on Electron Transport in GaAs. *Computational Materials Science*, 2015. **108, Part A**, 258-263.
- [23] Thelander, C.; Caroff, P.; Plissard, S.; Dey, A.W., and Dick, K.A., Effects of Crystal Phase Mixing on the Electrical Properties of InAs Nanowires. *Nano Lett.*, 2011. **11**, 2424-2429.
- [24] Dayeh, S.A.; Aplin, D.P.R.; Zhou, X.; Yu, P.K.L.; Yu, E.T., and Wang, D., High Electron Mobility InAs Nanowire Field-Effect Transistors. *Small*, 2007. **3**, 326-332.
- [25] Shalish, I.; Temkin, H., and Narayanamurti, V., Size-Dependent Surface Luminescence in ZnO Nanowires. *Phys. Rev. B*, 2004. **69**, 245401.
- [26] Vu, T.T.T.; Zehender, T.; Verheijen, A.M.; Plissard, R.S.; Immink, W.G.G.; Haverkort, E.M.J., and Bakkers, P.A.M.E., High Optical Quality Single Crystal Phase Wurtzite and Zincblende InP Nanowires. *Nanotechnology*, 2013. **24**, 115705.
- [27] Hjort, M.; Wallentin, J.; Timm, R.; Zakharov, A.A.; Håkanson, U.; Andersen, J.N.; Lundgren, E.; Samuelson, L.; Borgström, M.T., and Mikkelsen, A., Surface Chemistry, Structure, and Electronic Properties from Microns to the Atomic Scale of Axially Doped Semiconductor Nanowires. *ACS Nano*, 2012. **6**, 9679-9689.
- [28] Fengyun, W.; SenPo, Y.; Ning, H.; KitWa, F.; Hao, L.; Jared, J.H.; Guofa, D.; TakFu, H.; Chan, K.S., and Johnny, C.H., Surface Roughness Induced Electron Mobility Degradation in InAs Nanowires. *Nanotechnology*, 2013. **24**, 375202.

-
- [29] Cui, Y.; Wang, J.; Plissard, S.R.; Cavalli, A.; Vu, T.T.T.; van Veldhoven, R.P.J.; Gao, L.; Trainor, M.; Verheijen, M.A.; Haverkort, J.E.M., and Bakkers, E.P.A.M., Efficiency Enhancement of InP Nanowire Solar Cells by Surface Cleaning. *Nano Lett.*, 2013. **13**, 4113-4117.
- [30] Dayeh, S.A.; Soci, C.; Yu, P.K.L.; Yu, E.T., and Wang, D., Transport Properties of InAs Nanowire Field Effect Transistors: The Effects of Surface States. *Journal of Vacuum Science & Technology B: Microelectronics and Nanometer Structures Processing, Measurement, and Phenomena*, 2007. **25**, 1432-1436.
- [31] Sköld, N.; Karlsson, L.S.; Larsson, M.W.; Pistol, M.-E.; Seifert, W.; Trägårdh, J., and Samuelson, L., Growth and Optical Properties of Strained GaAs–Ga_(x)In_(1-x)P Core–Shell Nanowires. *Nano Lett.*, 2005. **5**, 1943-1947.
- [32] del Alamo, J.A., Nanometre-Scale Electronics with III-V Compound Semiconductors. *Nature*, 2011. **479**, 317-323.
- [33] Koenraad, P.M. and Flatte, M.E., Single Dopants in Semiconductors. *Nat. Mater.*, 2011. **10**, 91-100.
- [34] Parkinson, P.; Joyce, H.J.; Gao, Q.; Tan, H.H.; Zhang, X.; Zou, J.; Jagadish, C.; Herz, L.M., and Johnston, M.B., Carrier Lifetime and Mobility Enhancement in Nearly Defect-Free Core–Shell Nanowires Measured Using Time-Resolved Terahertz Spectroscopy. *Nano Lett.*, 2009. **9**, 3349-3353.
- [35] Capiod, P.; Xu, T.; Nys, J.P.; Berthe, M.; Patriarche, G.; Lymperakis, L.; Neugebauer, J.; Caroff, P.; Dunin-Borkowski, R.E.; Ebert, P., and Grandidier, B., Band Offsets at Zincblende-Wurtzite GaAs Nanowire Sidewall Surfaces. *Appl. Phys. Lett.*, 2013. **103**, 122104-4.
- [36] Xu, T.; Dick, K.A.; Plissard, S.; Nguyen, T.H.; Makoudi, Y.; Berthe, M.; Nys, J.P.; Wallart, X.; Grandidier, B., and Caroff, P., Faceting, Composition and Crystal Phase Evolution in III-V Antimonide Nanowire Heterostructures Revealed by Combining Microscopy Techniques. *Nanotechnology*, 2012. **23**, 095702.
- [37] Hjort, M.; Kratzer, P.; Lehmann, S.; Patel, S.J.; Dick, K.A.; Palmström, C.J.; Timm, R., and Mikkelsen, A., Crystal Structure Induced Preferential Surface Alloying of Sb on Wurtzite/Zinc Blende GaAs Nanowires. *Nano Lett.*, 2017. **17**, 3634-3640.
- [38] Knutsson, J.V.; Lehmann, S.; Hjort, M.; Reinke, P.; Lundgren, E.; Dick, K.A.; Timm, R., and Mikkelsen, A., Atomic Scale Surface Structure and Morphology of InAs Nanowire Crystal Superlattices: The Effect of Epitaxial Overgrowth. *ACS Appl. Mater. Interfaces*, 2015.
- [39] Binnig, G.; Rohrer, H.; Gerber, C., and Weibel, E., Tunneling through a Controllable Vacuum Gap. *Appl. Phys. Lett.*, 1982. **40**, 178-180.
- [40] Binnig, G.; Rohrer, H.; Gerber, C., and Weibel, E., Surface Studies by Scanning Tunneling Microscopy. *Phys. Rev. Lett.*, 1982. **49**, 57-61.
- [41] Binnig, G. and Rohrer, H., Scanning Tunneling Microscopy. *Surf. Sci.*, 1982. **126**, 236-244.
- [42] Bardeen, J., Tunnelling from a Many-Particle Point of View. *Phys. Rev. Lett.*, 1961. **6**, 57-59.
- [43] Alex, D.G. and Lisa, W., Bardeen's Tunnelling Theory as Applied to Scanning Tunneling Microscopy: A Technical Guide to the Traditional Interpretation. *Nanotechnology*, 2006. **17**, R57.
- [44] Tersoff, J. and Hamann, D.R., Theory and Application for the Scanning Tunneling Microscope. *Phys. Rev. Lett.*, 1983. **50**, 1998-2001.
- [45] Tersoff, J. and Hamann, D.R., Theory of the Scanning Tunneling Microscope. *Phys. Rev. B*, 1985. **31**, 805-813.

BIBLIOGRAPHY

- [46] Feenstra, R.M.; Stroscio, J.A.; Tersoff, J., and Fein, A.P., Atom-Selective Imaging of the GaAs(110) Surface. *Phys. Rev. Lett.*, 1987. **58**, 1192-1195.
- [47] Hjort, M.; Lehmann, S.; Knutsson, J.; Timm, R.; Jacobsson, D.; Lundgren, E.; Dick, K.A., and Mikkelsen, A., Direct Imaging of Atomic Scale Structure and Electronic Properties of GaAs Wurtzite and Zinc Blende Nanowire Surfaces. *Nano Lett.*, 2013. **13**, 4492-4498.
- [48] Hjort, M., *III-V Nanowire Surfaces*. Department of physics, PhD, 191. Lund University: Lund. 2014.
- [49] Feenstra, R.M., Scanning Tunneling Spectroscopy. *Surf. Sci.*, 1994. **299**, 965-979.
- [50] Chen, C.J., Theory of Scanning Tunneling Spectroscopy. *Journal of Vacuum Science & Technology A: Vacuum, Surfaces, and Films*, 1988. **6**, 319-322.
- [51] Walzer, K. and Hietschold, M., STM and STS Investigation of Ultrathin Tin Phthalocyanine Layers Adsorbed on Hpg(0001) and Au(111). *Surf. Sci.*, 2001. **471**, 1-10.
- [52] Feenstra, R.M. and Stroscio, J.A., Tunneling Spectroscopy of the GaAs(110) Surface. *J. Vac. Sci. Technol., B*, 1987. **5**, 923-929.
- [53] Feenstra, R.M., Tunneling Spectroscopy of the (110) Surface of Direct-Gap III-V Semiconductors. *Phys. Rev. B*, 1994. **50**, 4561-4570.
- [54] Kawagoe, T.; Tamura, E.; Suzuki, Y., and Koike, K., Scattering of Surface-State Electrons by the Monatomic Step in Fe(001): Differential Conductivity Imaging by Scanning Tunneling Microscopy. *Phys. Rev. B*, 2001. **65**, 024406.
- [55] Folsch, S.; Martinez-Blanco, J.; Yang, J.; Kanisawa, K., and Erwin, S.C., Quantum Dots with Single-Atom Precision. *Nat. Nanotechnol.*, 2014. **9**, 505-508.
- [56] Krenner, W.; Kühne, D.; Klappenberger, F., and Barth, J.V., Assessment of Scanning Tunneling Spectroscopy Modes Inspecting Electron Confinement in Surface-Confined Supramolecular Networks. *Scientific Reports*, 2013. **3**, 1454.
- [57] Yazdani, A.; Jones, B.A.; Lutz, C.P.; Crommie, M.F., and Eigler, D.M., Probing the Local Effects of Magnetic Impurities on Superconductivity. *Science*, 1997. **275**, 1767-1770.
- [58] Koenraad, P.M. and Flatte, M.E., Single Dopants in Semiconductors. *Nat. Mater.*, 2011. **10**, 91-100.
- [59] Crommie, M.F.; Lutz, C.P., and Eigler, D.M., Imaging Standing Waves in a Two-Dimensional Electron Gas. *Nature*, 1993. **363**, 524-527.
- [60] Timm, R.; Eisele, H.; Lenz, A.; Ivanova, L.; Vossebürger, V.; Warming, T.; Bimberg, D.; Farrer, I.; Ritchie, D.A., and Dähne, M., Confined States of Individual Type-II GaSb/GaAs Quantum Rings Studied by Cross-Sectional Scanning Tunneling Spectroscopy. *Nano Lett.*, 2010. **10**, 3972-3977.
- [61] Rahnejat, K.C.; Howard, C.A.; Shuttleworth, N.E.; Schofield, S.R.; Iwaya, K.; Hirjibehedin, C.F.; Renner, C.; Aeppli, G., and Ellerby, M., Charge Density Waves in the Graphene Sheets of the Superconductor *Cac*. *Nat Commun*, 2011. **2**, 558.
- [62] Feenstra, R.M.; Lee, J.Y.; Kang, M.H.; Meyer, G., and Rieder, K.H., Band Gap of the Ge(111)2x1 and Si(111)2x1 Surface by Scanning Tunneling Spectroscopy. *Phys. Rev. B*, 2006. **73**, 035310.
- [63] Bera, A.; Dey, S., and Pal, A.J., Band Mapping across a Pn-Junction in a Nanorod by Scanning Tunneling Microscopy. *Nano Lett.*, 2014.

-
- [64] Stroschio, J.A.; Feenstra, R.M., and Fein, A.P., Electronic Structure of the Si(111) 2x1 Surface by Scanning-Tunneling Microscopy. *Phys. Rev. Lett.*, 1986. **57**, 2579-2582.
- [65] Mårtensson, P. and Feenstra, R.M., Geometric and Electronic Structure of Antimony on the GaAs(110) Surface Studied by Scanning Tunneling Microscopy. *Phys. Rev. B*, 1989. **39**, 7744-7753.
- [66] Lang, N.D., Spectroscopy of Single Atoms in the Scanning Tunneling Microscope. *Phys. Rev. B*, 1986. **34**, 5947-5950.
- [67] Feenstra, R.M., Tunneling Spectroscopy of the Si(111) 2x1 Surface. *Phys. Rev. B*, 1999. **60**, 4478-4480.
- [68] Mårtensson, P. and Feenstra, R.M., Voltage-Dependent Imaging of Antimony on the GaAs(110) Surface. *Journal of Microscopy*, 1988. **152**, 761-769.
- [69] Feenstra, R.M.; Gaan, S.; Meyer, G., and Rieder, K.H., Low-Temperature Tunneling Spectroscopy of Ge(111) C(2x8) Surfaces. *Phys. Rev. B*, 2005. **71**, 125316.
- [70] Knutsson, J.V.; Lehmann, S.; Hjort, M.; Lundgren, E.; Dick, K.A.; Timm, R., and Mikkelsen, A., Electronic Structure Changes Due to Crystal Phase Switching at the Atomic Scale Limit. *ACS Nano*, 2017. **11**, 10519-10528.
- [71] Feenstra, R.M.; Dong, Y.; Semtsiv, M.P., and Masselink, W.T., Influence of Tip-Induced Band Bending on Tunneling Spectra of Semiconductor Surfaces. *Nanotechnology*, 2007. **18**, 044015.
- [72] Dombrowski, R.; Steinebach, C.; Wittneven, C.; Morgenstern, M., and Wiesendanger, R., Tip-Induced Band Bending by Scanning Tunneling Spectroscopy of the States of the Tip-Induced Quantum Dot on InAs(110). *Phys. Rev. B*, 1999. **59**, 8043-8048.
- [73] Morgenstern, M.; Haude, D.; Gudmundsson, V.; Wittneven, C.; Dombrowski, R.; Steinebach, C., and Wiesendanger, R., Low Temperature Scanning Tunneling Spectroscopy on InAs(110). *J. Electron Spectrosc. Relat. Phenom.*, 2000. **109**, 127-145.
- [74] Feenstra, R.M. *Semitip Software*. [http://www.andrew.cmu.edu/user/feenstra/semitip_v6/] 2011 [cited 2017 August].
- [75] Derry, G.N.; Kern, M.E., and Worth, E.H., Recommended Values of Clean Metal Surface Work Functions. *Journal of Vacuum Science & Technology A*, 2015. **33**, 060801.
- [76] Chen, C.J., Microscopic View of Scanning Tunneling Microscopy. *Journal of Vacuum Science & Technology A: Vacuum, Surfaces, and Films*, 1991. **9**, 44-50.
- [77] Chen, C.J., In-Situ Characterization of Tip Electronic Structure in Scanning Tunneling Microscopy. *Ultramicroscopy*, 1992. **42**, 147-153.
- [78] Sun, M.H.; Leong, E.S.P.; Chin, A.H.; Ning, C.Z.; Cirilin, G.E.; Yu, B.S.; Dubrovskii, V.G.; Chuang, L., and Chang-Hasnain, C., Photoluminescence Properties of InAs Nanowires Grown on GaAs and Si Substrates. *Nanotechnology*, 2010. **21**, 335705.
- [79] Ma, D.D.D.; Lee, C.S.; Au, F.C.K.; Tong, S.Y., and Lee, S.T., Small-Diameter Silicon Nanowire Surfaces. *Science*, 2003. **299**, 1874-1877.
- [80] Weitering, H.H.; Carpinelli, J.M.; Melechko, A.V.; Zhang, J.; Bartkowiak, M., and Plummer, E.W., Defect-Mediated Condensation of a Charge Density Wave. *Science (New York, N.Y.)*, 1999. **285**, 2107-2110.
- [81] Sacks, W.; Roditchev, D., and Klein, J., Voltage-Dependent STM Image of a Charge Density Wave. *Phys. Rev. B*, 1998. **57**, 13118-13131.

BIBLIOGRAPHY

- [82] Bode, M.; Heinze, S.; Kubetzka, A.; Pietzsch, O.; Nie, X.; Bihlmayer, G.; Blügel, S., and Wiesendanger, R., Magnetization-Direction-Dependent Local Electronic Structure Probed by Scanning Tunneling Spectroscopy. *Phys. Rev. Lett.*, 2002. **89**, 237205.
- [83] Pietzsch, O.; Kubetzka, A.; Bode, M., and Wiesendanger, R., Observation of Magnetic Hysteresis at the Nanometer Scale by Spin-Polarized Scanning Tunneling Spectroscopy. *Science*, 2001. **292**, 2053-2056.
- [84] Jourdan, M.; Huth, M., and Adrian, H., Superconductivity Mediated by Spin Fluctuations in the Heavy-Fermion Compound Upd_2Al_3 . *Nature*, 1999. **398**, 47-49.
- [85] Jäger, N.D.; Ebert, P.; Urban, K.; Krause-Rehberg, R., and Weber, E.R., Scanning Tunneling Microscopy and Spectroscopy of Semi-Insulating GaAs. *Phys. Rev. B*, 2002. **65**, 195318.
- [86] Khanbabaee, B.; Bussone, G.; Knutsson, J.V.; Geijselaers, I.; Pryor, C.E.; Rieger, T.; Demarina, N.; Grützmacher, D.; Lepsa, M.I.; Timm, R., and Pietsch, U., Band Bending at the Heterointerface of GaAs/InAs Core/Shell Nanowires Monitored by Synchrotron X-Ray Photoelectron Spectroscopy. *J. Appl. Phys.*, 2016. **120**, 145703.
- [87] Timm, R.; Head, A.; Yngman, S.; Knutsson, J.V.; Hjort, M.; McKibbin, S.; Troian, A.; Persson, O.; Urpelainen, S.; Knudsen, J.; Schnadt, J., and Mikkelsen, A., Self-Cleaning and Surface Chemical Reactions During HfO_2 Atomic Layer Deposition on InAs. *in manuscript*, 2017.
- [88] Schnadt, J.; Knudsen, J.; Andersen, J.N.; Siegbahn, H.; Pietzsch, A.; Hennies, F.; Johansson, N.; Mårtensson, N.; Öhrwall, G.; Bahr, S.; Mähl, S., and Schaff, O., The New Ambient-Pressure X-Ray Photoelectron Spectroscopy Instrument at Max-Lab. *Journal of Synchrotron Radiation*, 2012. **19**, 701-704.
- [89] Webb, J.L.; Knutsson, J.; Hjort, M.; Gorji Ghalamestani, S.; Dick, K.A.; Timm, R., and Mikkelsen, A., Electrical and Surface Properties of InAs/InSb Nanowires Cleaned by Atomic Hydrogen. *Nano Lett.*, 2015. **15**, 4865-4875.
- [90] Nyholm, R.; Andersen, J.N.; Johansson, U.; Jensen, B.N., and Lindau, I., Beamline I311 at Max-Lab: A Vuv/Soft X-Ray Undulator Beamline for High Resolution Electron Spectroscopy. *Nuclear Instruments and Methods in Physics Research Section A: Accelerators, Spectrometers, Detectors and Associated Equipment*, 2001. **467**, 520-524.
- [91] Doniach, S. and Sunjic, M., Many-Electron Singularity in X-Ray Photoemission and X-Ray Line Spectra from Metals. *Journal of Physics C: Solid State Physics*, 1970. **3**, 285.
- [92] Halpern, E.; Henning, A.; Shtrikman, H.; Rurali, R.; Cartoixà, X., and Rosenwaks, Y., Room Temperature Observation of Quantum Confinement in Single InAs Nanowires. *Nano Lett.*, 2015. **15**, 481-485.
- [93] Mourik, V.; Zuo, K.; Frolov, S.M.; Plissard, S.R.; Bakkers, E.P.A.M., and Kouwenhoven, L.P., Signatures of Majorana Fermions in Hybrid Superconductor-Semiconductor Nanowire Devices. *Science*, 2012. **336**, 1003-1007.
- [94] Das, A.; Ronen, Y.; Most, Y.; Oreg, Y.; Heiblum, M., and Shtrikman, H., Zero-Bias Peaks and Splitting in an Al-InAs Nanowire Topological Superconductor as a Signature of Majorana Fermions. *Nat. Phys.*, 2012. **8**, 887-895.
- [95] Deng, M.T.; Vaitiekėnas, S.; Hansen, E.B.; Danon, J.; Leijnse, M.; Flensberg, K.; Nygård, J.; Krogstrup, P., and Marcus, C.M., Majorana Bound State in a Coupled Quantum-Dot Hybrid-Nanowire System. *Science*, 2016. **354**, 1557-1562.
- [96] Qian, F.; Li, Y.; Gradedecak, S.; Park, H.-G.; Dong, Y.; Ding, Y.; Wang, Z.L., and Lieber, C.M., Multi-Quantum-Well Nanowire Heterostructures for Wavelength-Controlled Lasers. *Nat. Mater.*, 2008. **7**, 701-706.

-
- [97] Nilsson, M.; Namazi, L.; Lehmann, S.; Leijnse, M.; Dick, K.A., and Thelander, C., Single-Electron Transport in InAs Nanowire Quantum Dots Formed by Crystal Phase Engineering. *Phys. Rev. B*, 2016. **93**, 195422.
- [98] Lin, Y.-M. and Dresselhaus, M.S., Thermoelectric Properties of Superlattice Nanowires. *Phys. Rev. B*, 2003. **68**, 075304.
- [99] Premila, M.; Junichi, M., and Takashi, F., Controlled Growth of Highly Uniform, Axial/Radial Direction-Defined, Individually Addressable InP Nanowire Arrays. *Nanotechnology*, 2005. **16**, 2903.
- [100] Dey, A.W.; Svensson, J.; Ek, M.; Lind, E.; Thelander, C., and Wernersson, L.-E., Combining Axial and Radial Nanowire Heterostructures: Radial Esaki Diodes and Tunnel Field-Effect Transistors. *Nano Lett.*, 2013.
- [101] Dick, K.A.; Caroff, P.; Bolinsson, J.; Messing, M.E.; Johansson, J.; Deppert, K.; Wallenberg, L.R., and Samuelson, L., Control of III-V Nanowire Crystal Structure by Growth Parameter Tuning. *Semicond. Sci. Technol.*, 2010. **25**.
- [102] Caroff, P.; Bolinsson, J., and Johansson, J., Crystal Phases in III-V Nanowires: From Random toward Engineered Polytypism. *IEEE J. Sel. Top. Quantum Electron.*, 2011. **17**, 829-846.
- [103] Masanari, K.; Hiroshi, K.; Masamitsu, Y.; Kenji, H., and Toshio, K., Crystal Structure Change of GaAs and InAs Whiskers from Zinc-Blende to Wurtzite Type. *Japanese Journal of Applied Physics*, 1992. **31**, 2061.
- [104] Johansson, J.; Zanolli, Z., and Dick, K.A., Polytype Attainability in III-V Semiconductor Nanowires. *Cryst. Growth Des.*, 2016. **16**, 371-379.
- [105] Mårtensson, T.; Carlberg, P.; Borgström, M.; Montelius, L.; Seifert, W., and Samuelson, L., Nanowire Arrays Defined by Nanoimprint Lithography. *Nano Lett.*, 2004. **4**, 699-702.
- [106] Dick, K.A., A Review of Nanowire Growth Promoted by Alloys and Non-Alloying Elements with Emphasis on Au-Assisted III-V Nanowires. *Prog. Cryst. Growth Charact. Mater.*, 2008. **54**, 138-173.
- [107] Mandl, B.; Stangl, J.; Hilner, E.; Zakharov, A.A.; Hillerich, K.; Dey, A.W.; Samuelson, L.; Bauer, G.; Deppert, K., and Mikkelsen, A., Growth Mechanism of Self-Catalyzed Group III-V Nanowires. *Nano Lett.*, 2010. **10**, 4443-4449.
- [108] Heurlin, M.; Magnusson, M.H.; Lindgren, D.; Ek, M.; Wallenberg, L.R.; Deppert, K., and Samuelson, L., Continuous Gas-Phase Synthesis of Nanowires with Tunable Properties. *Nature*, 2012. **492**, 90-94.
- [109] Hofmann, S.; Sharma, R.; Wirth, C.T.; Cervantes-Sodi, F.; Ducati, C.; Kasama, T.; Dunin-Borkowski, R.E.; Drucker, J.; Bennett, P., and Robertson, J., Ledge-Flow-Controlled Catalyst Interface Dynamics During Si Nanowire Growth. *Nat. Mater.*, 2008. **7**, 372-375.
- [110] Wagner, R.S. and Ellis, W.C., Vapor - Liquid - Solid Mechanism of Single Crystal Growth. *Appl. Phys. Lett.*, 1964. **4**, 89-90.
- [111] Magnusson, M.H.; Deppert, K.; Malm, J.-O.; Bovin, J.-O., and Samuelson, L., Size-Selected Gold Nanoparticles by Aerosol Technology. *Nanostructured Materials*, 1999. **12**, 45-48.
- [112] Mandl, B.; Stangl, J.; Martensson, T.; Mikkelsen, A.; Eriksson, J.; Karlsson, L.S.; Bauer, G.; Samuelson, L., and Seifert, W., Au-Free Epitaxial Growth of InAs Nanowires. *Nano Lett.*, 2006. **6**, 1817-1821.
- [113] Jacobsson, D.; Panciera, F.; Tersoff, J.; Reuter, M.C.; Lehmann, S.; Hofmann, S.; Dick, K.A., and Ross, F.M., Interface Dynamics and Crystal Phase Switching in GaAs Nanowires. *Nature*, 2016. **531**, 317-322.

BIBLIOGRAPHY

- [114] Wen, C.Y.; Tersoff, J.; Reuter, M.C.; Stach, E.A., and Ross, F.M., Step-Flow Kinetics in Nanowire Growth. *Phys. Rev. Lett.*, 2010. **105**, 195502.
- [115] Lehmann, S.; Wallentin, J.; Jacobsson, D.; Deppert, K., and Dick, K.A., A General Approach for Sharp Crystal Phase Switching in InAs, GaAs, InP, and GaP Nanowires Using Only Group V Flow. *Nano Lett.*, 2013. **13**, 4099-4105.
- [116] Bolinsson, J.; Caroff, P.; Mandl, B., and Dick, K.A., Wurtzite-Zincblende Superlattices in InAs Nanowires Using a Supply Interruption Method. *Nanotechnology*, 2011. **22**.
- [117] Akopian, N.; Patriarche, G.; Liu, L.; Harmand, J.C., and Zwiller, V., Crystal Phase Quantum Dots. *Nano Lett.*, 2010. **10**, 1198-1201.
- [118] Vainorius, N.; Lehmann, S.; Jacobsson, D.; Samuelson, L.; Dick, K.A., and Pistol, M.-E., Confinement in Thickness-Controlled GaAs Polytype Nanodots. *Nano Lett.*, 2015. **15**, 2652-2656.
- [119] Bao, J.; Bell, D.C.; Capasso, F.; Wagner, J.B.; Mårtensson, T.; Trägårdh, J., and Samuelson, L., Optical Properties of Rotationally Twinned InP Nanowire Heterostructures. *Nano Lett.*, 2008. **8**, 836-841.
- [120] Svensson, S.F.; Jeppesen, S.; Thelander, C.; Samuelson, L.; Linke, H., and Dick, K.A., Control and Understanding of Kink Formation in InAs-InP Heterostructure Nanowires. *Nanotechnology*, 2013. **24**, 345601.
- [121] Caroff, P.; Messing, M.E.; Borg, B.M.; Dick, K.A.; Deppert, K., and Wernersson, L.E., InSb Heterostructure Nanowires: MOVPE Growth under Extreme Lattice Mismatch. *Nanotechnology*, 2009. **20**.
- [122] Paquette, B.; DeVita, M.; Turala, A.; Kolhatkar, G.; Boucherif, A.; Jaouad, A.; Aimez, V., and Arès, R., Optimization of p-doping in AlGaAs Grown by CBE Using Tma for AlGaAs/GaAs Tunnel Junctions. *J. Cryst. Growth*, 2013. **374**, 1-4.
- [123] Salehzadeh, O.; Zhang, X.; Gates, B.D.; Kavanagh, K.L., and Watkins, S.P., P-Type Doping of GaAs Nanowires Using Carbon. *J. Appl. Phys.*, 2012. **112**, 094323.
- [124] Thelander, C.; Dick, K.A.; Borgström, M.T.; Fröberg, L.E.; Caroff, P.; Nilsson, H.A., and Samuelson, L., The Electrical and Structural Properties of n-type InAs Nanowires Grown from Metal-Organic Precursors. *Nanotechnology*, 2010. **21**, 205703.
- [125] Miller, W.H., *A Treatise on Crystallography*. 1839, Trinity Street, London: J. & J. J. Deighton.
- [126] Jonas, J.; Brent, A.W.; Kimberly, A.D., and Werner, S., Growth Related Aspects of Epitaxial Nanowires. *Nanotechnology*, 2006. **17**, S355.
- [127] Algra, R.E.; Verheijen, M.A.; Borgstrom, M.T.; Feiner, L.-F.; Immink, G.; van Enckevort, W.J.P.; Vlieg, E., and Bakkers, E.P.A.M., Twinning Superlattices in Indium Phosphide Nanowires. *Nature*, 2008. **456**, 369-372.
- [128] Xiong, Q.; Wang, J., and Eklund, P.C., Coherent Twinning Phenomena: Towards Twinning Superlattices in III-V Semiconducting Nanowires. *Nano Lett.*, 2006. **6**, 2736-2742.
- [129] Knutsson, J.V.; Lehmann, S.; Hjort, M.; Lundgren, E.; Dick, K.A.; Timm, R., and Mikkelsen, A., Electronic Structure Changes Due to Crystal Phase Switching at the Atomic Scale Limit. *ACS Nano*, 2017.
- [130] Jacobsson, D.; Yang, F.; Hillerich, K.; Lenrick, F.; Lehmann, S.; Kriegner, D.; Stangl, J.; Wallenberg, L.R.; Dick, K.A., and Johansson, J., Phase Transformation in Radially Merged Wurtzite GaAs Nanowires. *Cryst. Growth Des.*, 2015.

-
- [131] Plante, M.C. and LaPierre, R.R., Control of GaAs Nanowire Morphology and Crystal Structure. *Nanotechnology*, 2008. **19**, 495603.
- [132] Regolin, I.; Sudfeld, D.; Lüttjohann, S.; Khorenko, V.; Prost, W.; Kästner, J.; Dumpich, G.; Meier, C.; Lorke, A., and Tegude, F.J., Growth and Characterisation of GaAs/InGaAs/GaAs Nanowhiskers on (111) GaAs. *J. Cryst. Growth*, 2007. **298**, 607-611.
- [133] Alexander, B.; Kilian, M.; Martin, E.; Mats-Erik, P.; Wallenberg, L.R., and Magnus, T.B., In Situ Etching for Control over Axial and Radial III-V Nanowire Growth Rates Using Hbr. *Nanotechnology*, 2014. **25**, 505601.
- [134] Borgström, M.T.; Wallentin, J.; Trägårdh, J.; Ramvall, P.; Ek, M.; Wallenberg, L.R.; Samuelson, L., and Deppert, K., In Situ Etching for Total Control over Axial and Radial Nanowire Growth. *Nano Research*, 2010. **3**, 264-270.
- [135] Joyce, H.J.; Gao, Q.; Tan, H.H.; Jagadish, C.; Kim, Y.; Fickenscher, M.A.; Perera, S.; Hoang, T.B.; Smith, L.M.; Jackson, H.E.; Yarrison-Rice, J.M.; Zhang, X., and Zou, J., Unexpected Benefits of Rapid Growth Rate for III-V Nanowires. *Nano Lett.*, 2009. **9**, 695-701.
- [136] Dick, K.A.; Deppert, K.; Samuelson, L., and Seifert, W., Optimization of Au-Assisted InAs Nanowires Grown by MOVPE. *J. Cryst. Growth*, 2006. **297**, 326-333.
- [137] Tomioka, K.; Yoshimura, M., and Fukui, T., A III-V Nanowire Channel on Silicon for High-Performance Vertical Transistors. *Nature*, 2012. **488**, 189-192.
- [138] Dimakis, E.; Jahn, U.; Ramsteiner, M.; Tahraoui, A.; Grandal, J.; Kong, X.; Marquardt, O.; Trampert, A.; Riechert, H., and Geelhaar, L., Coaxial Multishell (in,Ga)as/GaAs Nanowires for near-Infrared Emission on Si Substrates. *Nano Lett.*, 2014. **14**, 2604-2609.
- [139] Dai, X.; Zhang, S.; Wang, Z.; Adamo, G.; Liu, H.; Huang, Y.; Couteau, C., and Soci, C., GaAs/AlGaAs Nanowire Photodetector. *Nano Lett.*, 2014. **14**, 2688-2693.
- [140] Tian, B.; Zheng, X.; Kempa, T.J.; Fang, Y.; Yu, N.; Yu, G.; Huang, J., and Lieber, C.M., Coaxial Silicon Nanowires as Solar Cells and Nanoelectronic Power Sources. *Nature*, 2007. **449**, 885-889.
- [141] Hu, Y.; Kuemmeth, F.; Lieber, C.M., and Marcus, C.M., Hole Spin Relaxation in Ge-Si Core-Shell Nanowire Qubits. *Nat Nano*, 2012. **7**, 47-50.
- [142] Dufouleur, J.; Colombo, C.; Garma, T.; Ketterer, B.; Uccelli, E.; Nicotra, M., and Fontcuberta i Morral, A., P-Doping Mechanisms in Catalyst-Free Gallium Arsenide Nanowires. *Nano Lett.*, 2010. **10**, 1734-1740.
- [143] Zheng, C.; Wong-Leung, J.; Gao, Q.; Tan, H.H.; Jagadish, C., and Etheridge, J., Polarity-Driven 3-Fold Symmetry of GaAs/AlGaAs Core Multishell Nanowires. *Nano Lett.*, 2013. **13**, 3742-3748.
- [144] Guo, Y.-N.; Burgess, T.; Gao, Q.; Tan, H.H.; Jagadish, C., and Zou, J., Polarity-Driven Nonuniform Composition in InGaAs Nanowires. *Nano Lett.*, 2013. **13**, 5085-5089.
- [145] Rieger, T.; Schäpers, T.; Grützmacher, D., and Lepsa, M.I., Crystal Phase Selective Growth in GaAs/InAs Core-Shell Nanowires. *Cryst. Growth Des.*, 2014. **14**, 1167-1174.
- [146] Poole, P.J.; Dalacu, D.; Wu, X.; Lapointe, J., and Mnaymneh, K., Interplay between Crystal Phase Purity and Radial Growth in InP Nanowires. *Nanotechnology*, 2012. **23**, 385205.
- [147] Nilsson, M.; Namazi, L.; Lehmann, S.; Leijnse, M.; Dick, K.A., and Thelander, C., Electron-Hole Interactions in Coupled InAs-GaSb Quantum Dots Based on Nanowire Crystal Phase Templates. *Phys. Rev. B*, 2016. **94**, 115313.

BIBLIOGRAPHY

- [148] Chen, I.J.; Lehmann, S.; Nilsson, M.; Kivisaari, P.; Linke, H.; Dick, K.A., and Thelander, C., Conduction Band Offset and Polarization Effects in InAs Nanowire Polytype Junctions. *Nano Lett.*, 2017. **17**, 902-908.
- [149] Kusch, P.; Grelich, E.; Somaschini, C.; Luna, E.; Ramsteiner, M.; Geelhaar, L.; Riechert, H., and Reich, S., Type-II Band Alignment of Zinc-Blende and Wurtzite Segments in GaAs Nanowires: A Combined Photoluminescence and Resonant Raman Scattering Study. *Phys. Rev. B*, 2014. **89**, 045310.
- [150] Bouwes Bavinck, M.; Jöns, K.D.; Zieliński, M.; Patriarche, G.; Harmand, J.-C.; Akopian, N., and Zwiller, V., Photon Cascade from a Single Crystal Phase Nanowire Quantum Dot. *Nano Lett.*, 2016. **16**, 1081-1085.
- [151] Wallentin, J.; Ek, M.; Wallenberg, L.R.; Samuelson, L., and Borgström, M.T., Electron Trapping in InP Nanowire Fets with Stacking Faults. *Nano Lett.*, 2012. **12**, 151-155.
- [152] Pemasiri, K.; Montazeri, M.; Gass, R.; Smith, L.M.; Jackson, H.E.; Yarrison-Rice, J.; Paiman, S.; Gao, Q.; Tan, H.H.; Jagadish, C.; Zhang, X., and Zou, J., Carrier Dynamics and Quantum Confinement in Type II Zb-Wz InP Nanowire Homostructures. *Nano Lett.*, 2009. **9**, 648-654.
- [153] Caroff, P.; Dick, K.A.; Johansson, J.; Messing, M.E.; Deppert, K., and Samuelson, L., Controlled Polytypic and Twin-Plane Superlattices in III-V Nanowires. *Nat. Nanotechnol.*, 2009. **4**, 50-55.
- [154] Loitsch, B.; Winnerl, J.; Grimaldi, G.; Wierzbowski, J.; Rudolph, D.; Morkötter, S.; Döblinger, M.; Abstreiter, G.; Koblmüller, G., and Finley, J.J., Crystal Phase Quantum Dots in the Ultrathin Core of GaAs–AlGaAs Core–Shell Nanowires. *Nano Lett.*, 2015.
- [155] Belabbes, A.; Panse, C.; Furthmüller, J., and Bechstedt, F., Electronic Bands of III-V Semiconductor Polytypes and Their Alignment. *Phys. Rev. B*, 2012. **86**, 075208.
- [156] Gustafsson, A.; Reinhardt, F.; Biasiol, G., and Kapon, E., Low-Pressure Organometallic Chemical Vapor Deposition of Quantum Wires on V-Grooved Substrates. *Appl. Phys. Lett.*, 1995. **67**, 3673-3675.
- [157] Ishida, S.; Arakawa, Y., and Wada, K., Seeded Self-Assembled GaAs Quantum Dots Grown in Two-Dimensional V Grooves by Selective Metal–Organic Chemical-Vapor Deposition. *Appl. Phys. Lett.*, 1998. **72**, 800-802.
- [158] Ellis, S.G.; Herman, F.; Loebner, E.E.; Merz, W.J.; Struck, C.W., and White, J.G., Photovoltages Larger Than the Band Gap in Zinc Sulfide Crystals. *Phys. Rev.*, 1958. **109**, 1860-1860.
- [159] Lempicki, A., Anomalous Photovoltaic Effect in ZnS Single Crystals. *Phys. Rev.*, 1959. **113**, 1204-1209.
- [160] Kroutvar, M.; Ducommun, Y.; Heiss, D.; Bichler, M.; Schuh, D.; Abstreiter, G., and Finley, J.J., Optically Programmable Electron Spin Memory Using Semiconductor Quantum Dots. *Nature*, 2004. **432**, 81-84.
- [161] Lind, E.; Persson, A.I.; Samuelson, L., and Wernersson, L.-E., Improved Subthreshold Slope in an InAs Nanowire Heterostructure Field-Effect Transistor. *Nano Lett.*, 2006. **6**, 1842-1846.
- [162] Memisevic, E.; Hellenbrand, M.; Lind, E.; Persson, A.R.; Sant, S.; Schenk, A.; Svensson, J.; Wallenberg, R., and Wernersson, L.-E., Individual Defects in InAs/InGaAsSb/GaSb Nanowire Tunnel Field-Effect Transistors Operating Below 60 mV/Decade. *Nano Lett.*, 2017. **17**, 4373-4380.
- [163] Miao, M.S.; Yan, Q.M., and Walle, C.G.V.d., Electronic Structure of a Single-Layer InN Quantum Well in a GaN Matrix. *Appl. Phys. Lett.*, 2013. **102**, 102103.
- [164] Baretin, D.; Maur, M.A.d.; Pecchia, A., and Carlo, A.d. Realistic Models of Quantum-Dot Heterostructures. in *Numer. Simul. Optoelectron. Devices*. 2014. Palma de Mallorca, Spain IEEE.

-
- [165] Magri, R. and Zunger, A., Theory of Optical Properties of 6.1 Å III–V Superlattices: The Role of the Interfaces. *Journal of Vacuum Science & Technology B: Microelectronics and Nanometer Structures Processing, Measurement, and Phenomena*, 2003. **21**, 1896-1902.
- [166] Bauer, R.S. and Sang, H.W., On the Adjustability of the “Abrupt” Heterojunction Band-Gap Discontinuity. *Surf. Sci.*, 1983. **132**, 479-504.
- [167] Luna, E.; Guzmán, Á.; Trampert, A., and Álvarez, G., Critical Role of Two-Dimensional Island-Mediated Growth on the Formation of Semiconductor Heterointerfaces. *Phys. Rev. Lett.*, 2012. **109**, 126101.
- [168] Kawasaki, J.K.; Timm, R.; Delaney, K.T.; Lundgren, E.; Mikkelsen, A., and Palmström, C.J., Local Density of States and Interface Effects in Semimetallic ErAs Nanoparticles Embedded in GaAs. *Phys. Rev. Lett.*, 2011. **107**, 036806.
- [169] Joyce, H.J.; Wong-Leung, J.; Gao, Q.; Tan, H.H., and Jagadish, C., Phase Perfection in Zinc Blende and Wurtzite III–V Nanowires Using Basic Growth Parameters. *Nano Lett.*, 2010. **10**, 908-915.
- [170] Zanolli, Z.; Fuchs, F.; Furthmüller, J.; von Barth, U., and Bechstedt, F., Model GW Band Structure of InAs and GaAs in the Wurtzite Phase. *Phys. Rev. B*, 2007. **75**, 245121.
- [171] De, A. and Pryor, C.E., Predicted Band Structures of III-V Semiconductors in the Wurtzite Phase. *Phys. Rev. B*, 2010. **81**, 155210.
- [172] Luis, C.O.D. and Cantarero, A., Ab Initio Calculations of Indium Arsenide in the Wurtzite Phase: Structural, Electronic and Optical Properties. *Mater. Res. Express*, 2014. **1**, 015702.
- [173] Murayama, M. and Nakayama, T., Chemical Trend of Band Offsets at Wurtzite/Zinc-Blende Heterocrystalline Semiconductor Interfaces. *Phys. Rev. B*, 1994. **49**, 4710-4724.
- [174] Yeh, C.-Y.; Wei, S.-H., and Zunger, A., Relationships between the Band Gaps of the Zinc-Blende and Wurtzite Modifications of Semiconductors. *Phys. Rev. B*, 1994. **50**, 2715-2718.
- [175] Koblmüller, G.; Hertenberger, S.; Vizbaras, K.; Bichler, M.; Bao, F.; Zhang, J.P., and Abstreiter, G., Self-Induced Growth of Vertical Free-Standing InAs Nanowires on Si(111) by Molecular Beam Epitaxy. *Nanotechnology*, 2010. **21**, 365602.
- [176] Rota, M.B.; Ameruddin, A.S.; Fonseka, H.A.; Gao, Q.; Mura, F.; Polimeni, A.; Miriametro, A.; Tan, H.H.; Jagadish, C., and Capizzi, M., Bandgap Energy of Wurtzite InAs Nanowires. *Nano Lett.*, 2016. **16**, 5197-5203.
- [177] Bao, J.; Bell, D.C.; Capasso, F.; Erdman, N.; Wei, D.; Fröberg, L.; Mårtensson, T., and Samuelson, L., Nanowire-Induced Wurtzite InAs Thin Film on Zinc-Blende InAs Substrate. *Adv. Mater. (Weinheim, Ger.)*, 2009. **21**, 3654-3658.
- [178] Möller, M.; M. M. de Lima, J.; Cantarero, A.; Chiamonte, T.; Cotta, M.A., and Iikawa, F., Optical Emission of InAs Nanowires. *Nanotechnology*, 2012. **23**, 375704.
- [179] Trägårdh, J.; Persson, A.I.; Wagner, J.B.; Hessman, D., and Samuelson, L., Measurements of the Band Gap of Wurtzite InAs_(1-x)P_(x) Nanowires Using Photocurrent Spectroscopy. *J. Appl. Phys.*, 2007. **101**, 123701.
- [180] Feenstra, R.M. and Mårtensson, P., Fermi-Level Pinning at the Sb/GaAs(110) Surface Studied by Scanning Tunneling Spectroscopy. *Phys. Rev. Lett.*, 1988. **61**, 447-450.
- [181] Aristov, V.Y.; Bolotin, I.L., and Gelakhova, S.G., Anomalous Pinning of the Fermi Level at the InAs(110)-Cu Interface Obtained at 10 K. *Surf. Sci.*, 1991. **251**, 453-456.

BIBLIOGRAPHY

- [182] Pashley, M.D.; Haberern, K.W.; Feenstra, R.M., and Kirchner, P.D., Different Fermi-Level Pinning Behavior on N- and P-Type GaAs(001). *Phys. Rev. B*, 1993. **48**, 4612-4615.
- [183] Dow, J.D. and Allen, R.E., Surface Defects and Fermi - Level Pinning in InP. *Journal of Vacuum Science and Technology*, 1982. **20**, 659-661.
- [184] Heinze, D.; Breddermann, D.; Zrenner, A., and Schumacher, S., A Quantum Dot Single-Photon Source with on-the-Fly All-Optical Polarization Control and Timed Emission. *Nat. Commun.*, 2015. **6**, 8473.
- [185] Juska, G.; Dimastrodonato, V.; Mereni, L.O.; Gocalinska, A., and Pelucchi, E., Towards Quantum-Dot Arrays of Entangled Photon Emitters. *Nat. Photonics*, 2013. **7**, 527-531.
- [186] Bayer, M.; Hawrylak, P.; Hinzer, K.; Fafard, S.; Korkusinski, M.; Wasilewski, Z.R.; Stern, O., and Forchel, A., Coupling and Entangling of Quantum States in Quantum Dot Molecules. *Science*, 2001. **291**, 451-453.
- [187] Toru, A.; Kohji, N., and Tomonori, I., Effects of Stacking Sequence on the Electrical Conductivity of InAs: A Combination of Density Functional Theory and Boltzmann Transport Equation Calculations. *Japanese Journal of Applied Physics*, 2015. **54**, 075001.
- [188] Northrup, J.E. and Cohen, M.L., Electronic Structure of the Rotation Twin Stacking Fault in β -ZnS. *Phys. Rev. B*, 1981. **23**, 2563-2566.
- [189] Birman, J.L., Simplified LCAO Method for Zincblende, Wurtzite, and Mixed Crystal Structures. *Phys. Rev.*, 1959. **115**, 1493-1505.
- [190] Xue, Q.-K.; Hashizume, T., and Sakurai, T., Scanning Tunneling Microscopy of III-V Compound Semiconductor (001) Surfaces. *Prog. Surf. Sci.*, 1997. **56**, 1-131.
- [191] Akbulut, S.; Akbulut, A.; Özdemir, M., and Yildiz, F., Effect of GaAs (100) Substrate Surface Reconstruction on Magnetic Properties of Ni Thin Films. *J. Magn. Magn. Mater.*, 2015. **373**, 155-159.
- [192] Pal, S.; Jasper-Tönnies, T.; Hack, M., and Pehlke, E., Effect of Surface Reconstruction on the Electronic Structure of ZnO(0001). *Phys. Rev. B*, 2013. **87**, 085445.
- [193] Griffiths, C.L.; Anyele, H.T.; Matthai, C.C.; Cafolla, A.A., and Williams, R.H., Effect of Surface Reconstruction on Fermi - Level Pinning in the Sn on Si(111) System. *Journal of Vacuum Science & Technology B*, 1993. **11**, 1559-1563.
- [194] Zhang, S. and Zunger, A., Surface-Reconstruction-Enhanced Solubility of N, P, as, and Sb in III-V Semiconductors. *Appl. Phys. Lett.*, 1997. **71**.
- [195] Patrizia, B.; Jorge, L.-C.; Elizabeth, G.; Aitor, M.; Frederik, S.; Ortega, J.E., and Eugene, E.K., Effect of Surface Reconstruction on the Photoemission Cross-Section of the Au(111) Surface State. *J. Phys.: Condens. Matter*, 2012. **24**, 395006.
- [196] Michely, T.; Hohage, M.; Esch, S., and Comsa, G., The Effect of Surface Reconstruction on the Growth Mode in Homoepitaxy. *Surf. Sci.*, 1996. **349**, L89-L94.
- [197] Rosini, M.; Kratzer, P., and Magri, R., In Adatom Diffusion on $\text{in}_{(x)}\text{Ga}_{(1-x)}\text{as}/\text{GaAs}(001)$: Effects of Strain, Reconstruction and Composition. *J. Phys.: Condens. Matter*, 2009. **21**, 355007.
- [198] Hilner, E.; Hakanson, U.; Froberg, L.E.; Karlsson, M.; Kratzer, P.; Lundgren, E.; Samuelson, L., and Mikkelsen, A., Direct Atomic Scale Imaging of III-V Nanowire Surfaces. *Nano Lett.*, 2008. **8**, 3978-3982.

-
- [199] Taguchi, A. and Kanisawa, K., Stable Reconstruction and Adsorbates of InAs(111)a Surface. *Appl. Surf. Sci.*, 2006. **252**, 5263-5266.
- [200] Thornton, J.M.C.; Woolf, D.A., and Weightman, P., Reconstructions of the GaAs(111)B Surface. *Appl. Surf. Sci.*, 1998. **123**, 115-119.
- [201] Farrell, H.H.; Lu, J.; Schultz, B.D.; Denison, A.B., and Palmstrøm, C.J., GaAs(111)B($\sqrt{19} \times \sqrt{19}$)R23.4 Degrees Surface Reconstruction. *J. Vac. Sci. Technol., B*, 2001. **19**, 1597-1605.
- [202] Hilner, E.; Lundgren, E., and Mikkelsen, A., Surface Structure and Morphology of InAs(111)B with/without Gold Nanoparticles Annealed under Arsenic or Atomic Hydrogen Flux. *Surf. Sci.*, 2010. **604**, 354-360.
- [203] Engels, B.; Richard, P.; Schroeder, K.; Blügel, S.; Ebert, P., and Urban, K., Comparison between Ab Initio Theory and Scanning Tunneling Microscopy for (110) Surfaces of III-V Semiconductors. *Phys. Rev. B*, 1998. **58**, 7799-7815.
- [204] Chelikowsky, J.R. and Cohen, M.L., Self-Consistent Pseudopotential Calculation for the Relaxed (110) Surface of GaAs. *Phys. Rev. B*, 1979. **20**, 4150-4159.
- [205] van der Wielen, M.C.M.M.; van Roij, A.J.A., and van Kempen, H., Direct Observation of Friedel Oscillations around Incorporated Si_{Ga} Dopants in GaAs by Low-Temperature Scanning Tunneling Microscopy. *Phys. Rev. Lett.*, 1996. **76**, 1075-1078.
- [206] Sagisaka, K. and Fujita, D., Standing Waves on Si(100) and Ge(100) Surfaces Observed by Scanning Tunneling Microscopy. *Phys. Rev. B*, 2005. **72**, 235327.
- [207] Degtyarev, V.E.; Khazanova, S.V., and Demarina, N.V., Features of Electron Gas in InAs Nanowires Imposed by Interplay between Nanowire Geometry, Doping and Surface States. *Scientific Reports*, 2017. **7**, 3411.
- [208] Bell, G.R.; Kaijaks, N.S.; Dixon, R.J., and McConville, C.F., Atomic Hydrogen Cleaning of Polar III-V Semiconductor Surfaces. *Surf. Sci.*, 1998. **401**, 125-137.
- [209] Rice, A.D.; Kawasaki, J.K.; Verma, N.; Pennachio, D.J.; Schultz, B.D., and Palmstrøm, C.J., Structural and Electronic Properties of Molecular Beam Epitaxially Grown Ni_(1+x)TiSn Films. *J. Cryst. Growth*, 2017. **467**, 71-76.
- [210] Kjaergaard, M.; Suominen, H.J.; Nowak, M.P.; Akhmerov, A.R.; Shabani, J.; Palmstrøm, C.J.; Nichele, F., and Marcus, C.M., Transparent Semiconductor-Superconductor Interface and Induced Gap in an Epitaxial Heterostructure Josephson Junction. *Physical Review Applied*, 2017. **7**, 034029.
- [211] Drachmann, A.C.C.; Suominen, H.J.; Kjaergaard, M.; Shojaei, B.; Palmstrøm, C.J.; Marcus, C.M., and Nichele, F., Proximity Effect Transfer from NbTi into a Semiconductor Heterostructure Via Epitaxial Aluminum. *Nano Lett.*, 2017. **17**, 1200-1203.
- [212] Harrington, S.D.; Sharan, A.; Rice, A.D.; Logan, J.A.; McFadden, A.P.; Pendharkar, M.; Pennachio, D.J.; Wilson, N.S.; Gui, Z.; Janotti, A., and Palmstrøm, C.J., Valence-Band Offsets of CoTiSb/In_{0.53}Ga_{0.47}As and CoTiSb/In_{0.52}Al_{0.48}As Heterojunctions. *Appl. Phys. Lett.*, 2017. **111**, 061605.
- [213] Drozdov, I.K.; Alexandradinata, A.; Jeon, S.; Nadj-Perge, S.; Ji, H.; Cava, R.J.; Andrei Bernevig, B., and Yazdani, A., One-Dimensional Topological Edge States of Bismuth Bilayers. *Nat. Phys.*, 2014. **10**, 664-669.
- [214] Huang, H.; Liu, J., and Duan, W., Nontrivial Z₂ Topology in Bismuth-Based III-V Compounds. *Phys. Rev. B*, 2014. **90**, 195105.

BIBLIOGRAPHY

- [215] Gladysiewicz, M.; Kudrawiec, R., and Wartak, M.S., Electronic Band Structure and Material Gain of III-V-Bi Quantum Wells Grown on GaSb Substrate and Dedicated for Mid-Infrared Spectral Range. *J. Appl. Phys.*, 2016. **119**, 075701.
- [216] Fluegel, B.; Francoeur, S.; Mascarenhas, A.; Tixier, S.; Young, E.C., and Tiedje, T., Giant Spin-Orbit Bowing in GaAs_{1-x}Bi_x. *Phys. Rev. Lett.*, 2006. **97**.
- [217] Fluegel, B.; Mascarenhas, A.; Ptak, A.J.; Tixier, S.; Young, E.C., and Tiedje, T., E₊ Transition in GaAs_{1-x}N_x and GaAs_{1-x}Bi_x Due to Isoelectronic-Impurity-Induced Perturbation of the Conduction Band. *Phys. Rev. B*, 2007. **76**, 155209.
- [218] Timm, R.; Persson, O.; Engberg, D.L.J.; Fian, A.; Webb, J.L.; Wallentin, J.; Jönsson, A.; Borgström, M.T.; Samuelson, L., and Mikkelsen, A., Current–Voltage Characterization of Individual as-Grown Nanowires Using a Scanning Tunneling Microscope. *Nano Lett.*, 2013. **13**, 5182-5189.
- [219] Webb, J.; Persson, O.; Dick, K.; Thelander, C.; Timm, R., and Mikkelsen, A., High Resolution Scanning Gate Microscopy Measurements on InAs/GaSb Nanowire Esaki Diode Devices. *Nano Research*, 2014. **7**, 877-887.
- [220] Persson, O.; Webb, J.L.; Dick, K.A.; Thelander, C.; Mikkelsen, A., and Timm, R., Scanning Tunneling Spectroscopy on InAs–GaSb Esaki Diode Nanowire Devices During Operation. *Nano Lett.*, 2015. **15**, 3684-3691.
- [221] Tao, C.; Cullen, W.G., and Williams, E.D., Visualizing the Electron Scattering Force in Nanostructures. *Science*, 2010. **328**, 736-740.
- [222] Bondarchuk, O.; Cullen, W.G.; Degawa, M.; Williams, E.D.; Bole, T., and Rous, P.J., Biased Surface Fluctuations Due to Current Stress. *Phys. Rev. Lett.*, 2007. **99**, 206801.
- [223] Webb, J.L.; Knutsson, J.; Hjort, M.; McKibbin, S.R.; Lehmann, S.; Thelander, C.; Dick, K.A.; Timm, R., and Mikkelsen, A., Imaging Atomic Scale Dynamics on III–V Nanowire Surfaces During Electrical Operation. *Scientific Reports*, 2017. **7**, 12790.
- [224] Hjort, M.; Lehmann, S.; Knutsson, J.; Zakharov, A.A.; Du, Y.A.; Sakong, S.; Timm, R.; Nylund, G.; Lundgren, E.; Kratzer, P.; Dick, K.A., and Mikkelsen, A., Electronic and Structural Differences between Wurtzite and Zinc Blende InAs Nanowire Surfaces: Experiment and Theory. *ACS Nano*, 2014. **8**, 12346-12355.
- [225] Hjort, M.; Knutsson, J.V.; Mandl, B.; Deppert, K.; Lundgren, E.; Timm, R., and Mikkelsen, A., Surface Morphology of Au-Free Grown Nanowires after Native Oxide Removal. *Nanoscale*, 2015. **7**, 9998-10004.
- [226] Xu, T.; Wei, M.J.; Capiod, P.; Díaz Álvarez, A.; Han, X.L.; Troadec, D.; Nys, J.P.; Berthe, M.; Lefebvre, I.; Patriarche, G.; Plissard, S.R.; Caroff, P.; Ebert, P., and Grandidier, B., Type I Band Alignment in GaAs₈₁Sb₁₉/GaAs Core-Shell Nanowires. *Appl. Phys. Lett.*, 2015. **107**, 112102.
- [227] Díaz Álvarez, A.; Xu, T.; Tütüncüoğlu, G.; Demonchaux, T.; Nys, J.-P.; Berthe, M.; Matteini, F.; Potts, H.A.; Troadec, D.; Patriarche, G.; Lampin, J.-F.; Coinon, C.; Fontcuberta i Morral, A.; Dunin-Borkowski, R.E.; Ebert, P., and Grandidier, B., Nonstoichiometric Low-Temperature Grown GaAs Nanowires. *Nano Lett.*, 2015.
- [228] Schnedler, M.; Lefebvre, I.; Xu, T.; Portz, V.; Patriarche, G.; Nys, J.P.; Plissard, S.R.; Caroff, P.; Berthe, M.; Eisele, H.; Dunin-Borkowski, R.E.; Ebert, P., and Grandidier, B., Lazarevicite-Type Short-Range Ordering in Ternary III-V Nanowires. *Phys. Rev. B*, 2016. **94**, 195306.
- [229] Memisevic, E., *Vertical III-V Nanowire Tunnel Field-Effect Transistor*. Department of Electrical and Information Technology, PhD, 162. Lund University: Lund. 2017.